WIND SPEED ESTIMATES AND PRECIPITATION
DETECTION USING AMBIENT SOUND
IN THE OCEAN

DOUGLAS J. SCHILLINGER

INFORMATION TO USERS

This manuscript has been reproduced from the microfilm master. UMI films the text directly from the original or copy submitted. Thus, some thesis and dissertation copies are in typewriter face, while others may be from any type of computer printer.

The quality of this reproduction is dependent upon the quality of the copy submitted. Broken or indistinct print, colored or poor quality illustrations and photographs, print bleedthrough, substandard margins, and improper alignment can adversely affect reproduction.

In the unlikely event that the author did not send UMI a complete manuscript and there are missing pages, these will be noted. Also, if unauthorized copyright material had to be removed, a note will indicate the deletion.

Oversize materials (e.g., maps, drawings, charts) are reproduced by sectioning the original, beginning at the upper left-hand corner and continuing from left to right in equal sections with small overlaps.

Photographs included in the original manuscript have been reproduced xerographically in this copy. Higher quality 6" x 9" black and white photographic prints are available for any photographs or illustrations appearing in this copy for an additional charge. Contact UMI directly to order.

Wind Speed Estimates and Precipitation Detection Using Ambient Sound in the Ocean

by

© Douglas J. Schillinger

B.Sc.(Hon) (University of Guelph, Guelph, Canada) 1998

A thesis submitted to the

School of Graduate Studies

in partial fulfillment of the

requirements for the degree of

Master of Science

Department of Physics and Physical Oceanography

Memorial University of Newfoundland

June 2000

St. John's   Newfoundland

Abstract

This thesis explores the relationship between ocean ambient sound levels, wind speed and rain. It has long been known that these surface processes generate sound in the ocean, but the development of accurate algorithms has been complicated by the difficulty in obtaining location independent sound levels. Here, absolute source level estimates are achieved by modelling the sources as an infinite field of dipoles at the surface, and accounting for acoustic absorption and reflection from the ocean floor. It is shown that bottom reflections are an important component in elevating sound levels at frequencies below 35 kHz. Knowing absolute source levels, these sound levels can be used to estimate both wind speed and detect the occurrence of precipitation. It is shown that the wind-only generated ambient sound spectrum has a mean slope of -18 dB/decade and ranges from -16 to -20 dB/decade corresponding to wind speeds from 0 to 20 $m\,s^{-1}$ for frequencies from 1 to 10 kHz. The spectral slope at frequencies greater than 10 kHz depends upon wind speed. Existing estimation algorithms are shown to overestimate the speed for wind speeds below 10 $m\,s^{-1}$ but underestimate wind speeds above 10 $m\,s^{-1}$ and that there is a maximum sound level which limits wind speed estimation for frequencies above 10 kHz. A wind speed dependent correction for the existing algorithms is proposed which gives accuracies $\pm 1.3 - 2\,m\,s^{-1}$ depending on deployment characteristics and sampling parameters. The accuracy of precipitation identification is limited by the wind speed and the precipitation type. Precipitation classified as Rain by the World Meteorological Organization (WMO) is detectable via acoustic means. Sub-division of the classification of the WMO categories shows that $50\% \pm 10\%$ of 'Continuous Rain' and $25\% \pm 12.5\%$ of 'Intermittent Rain' are detectable using the ambient sound spectra.

Acknowledgements

iii

Contents

List of Figures

vii

viii

x

List of Tables

xv

Chapter 1

Introduction

In the ocean, sound travels great distances relatively unimpeded while electro-magnetic waves suffer great attenuation. As a result, the generation and propagation of sound in the ocean is of great importance as sound is the principle mechanism for navigation and communication. With the advent of submersible vessels, the study of sound in the ocean has become relevant to military applications. Recent technologies and new understanding of ocean acoustics have expanded this field to meteorological and oceanographic applications. Two of these new applications are estimating wind speed and detecting precipitation from subsurface hydrophones using the very sources of sound which were historically a nuisance to hydro-acoustic operations – Ambient Sound.

Meteorological data is important in understanding the world around us. Weather prediction is arguably the most important aspect of meteorology to marine operations but recent environmental concerns, specifically global warming, have increased the importance of collecting meteorological data. However, collecting accurate wind speed data and rainfall data on land can be problematic. Ensuring that measurements are not affected by local topography or man made structures, including the

1

data collecting devices themselves, is difficult. This problem is magnified at sea where waves, spray and ice can affect surface buoys. Compounding this problem, the oceans represent 70% of the Earth's surface, and collecting meteorological data from the open ocean is of the utmost importance. Many existing oceanographic equipment record sound over the frequency range of wind-generated and precipitation-generated ambient sound. In sense, while studying other phenomenon, you can get the wind speed at the surface for free. A more down-to-earth appraisal is that using ambient sound to measure wind speed and precipitation represents an alternative means of meteorological data collection.

While previous studies of ambient sound as generated by wind (Knudsen et al. 1948; Wenz 1962; Shaw et al. 1978; Evans and Watts 1982; Vagle et al. 1990) and precipitation (Franz 1959; Lokken and Bom 1972; Nystuen 1986, 1987; Medwin et al. 1992) have been limited in duration, recorded sound bandwidth, and wind speeds, the present data include the ambient sound spectra for wind speeds from 1 to 21 $m\,s^{-1}$ and coincide with a variety of meteorological events, for example, 'rain,' 'drizzle' and 'fog.' Using this unique data set, the accuracy of two existing wind speed equations, from Vagle et al. (1990) and Evans and Watts (1982), are compared to the accuracy of a wind speed algorithm developed using the present data. The performance of these three equations are quantified for frequencies from 1 to 72 kHz by contrasting the mean and standard deviation of the absolute error in the wind speed estimate from the Sound Source Levels (SSL). Coincidental to the wind speed estimates over the entire spectrum is the behaviour of the spectral slope with wind speed. To characterize this behaviour, comparisons of the spectral slope between two data sets are made over three spectral regions. One result of the non-linear spectral slope of

2

ambient sound from 1 to 72 kHz is that there exists a maximum resolvable wind speed for frequencies greater than 10 kHz.

In addition to placing limits on the accuracy of wind speed estimates and characterizing the spectral behaviour with wind speed, the effects of both wind speed and rainfall rates on the acoustic signature over frequencies from 1 to 72 kHz are explored. The effects of precipitation and wind are studied by comparing the identifications of precipitation made using two characteristic features of precipitation dominated ambient sound spectra to two reference records of precipitation. These identifications are classified as either correct or incorrect and are further divided into correct identifications categorized by wind speed and precipitation type.

The ambient sound data presented here were recorded by the Ocean Ambient Sound Instrumentation System (OASIS) at Ocean Weather Station Mike (OWS Mike). The OASIS device consists of an RD Instruments (RDI) Broadband upward-looking ADCP and an International Transducer Corporation (ITC) Hydrophone, model number 6050-C. OWS Mike is a weather station located 210 km west of Bergen, Norway (at 66°N, 2°E), as shown in Figure 1.1. The weather station is described in Gammelsroed et al. (1992).

The present data spans 37 days in 1996, from Julian day 137 to 174 (mid-May until mid-June), and spans 74 days in 1997, from Julian day 111.8 to 185.8 (mid March to the beginning of July). During the deployment, several storms are observed over the instrument. From OWS Mike, a complete meteorological record is available, as well as wind speed records from a ship-mounted anemometer. Quantitative measurements of rainfall rates from an Optical Rain Gauge (ORG) are available for the 1997 deployment.

3
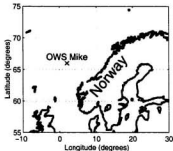
Figure 1.1: The location of Ocean Weather Station Mike (OWS Mike), 210 km west of Bergen, Norway (at 66°N, 2°E).

1.1 Thesis Outline

Chapter 2 outlines general theory for sound propagation in water, the generation of sound by air bubbles and the scattering potential of air bubbles. This theory is completed by a literature review of the study of wind-only ambient sound and the ambient sound generated by falling raindrops. The historical research on bubble entrainment and precipitation are also reviewed.

Chapter 3 is devoted to the signal processing and data acquisition of the OASIS instrument. This instrument provides both the intensity of ambient sound, and the backscatter intensity from an upward-looking ADCP for the purpose of determining wind direction. Wind direction estimation is not discussed in this thesis. For a detailed explanation of wind direction estimation from the ADCP data at OWS Mike using the data from 1996 and 1997 see Zedel et al. (1998). For an overview of the technique for determination of the wind direction see Zedel et al. (1996).

4

Chapter 4 explores the determination of a universal wind speed from ambient sound equation. The coefficients of this equation are determined, and their behaviour with frequency are examined. This frequency dependent wind speed estimation equation is compared to two existing frequency independent methods of estimating wind speed by examining the standard deviation and mean of the time series of the error in wind speed estimation. Further to wind speed estimation, three methods of improved wind speed estimation are contrasted: time averaging, spectral averaging, and a wind speed dependent correction factor. In addition to wind speed estimates, the spectral behaviour with wind speed for three separate regions of the ambient sound spectrum is examined. Finally, the maximum wind speeds which can be estimated from SSL are determined for all frequencies, and these results are compared to those presented by Vagle et al. (1990).

Analysis of Precipitation Identification from ambient sound Algorithms (PIAs) is given for two different algorithms in Chapter 5. The acoustic observations are compared to visual records from crew members of OWS Mike, as recorded following the World Meteorological Organization (WMO) observing standards. The 100 WMO weather observation conditions are re-categorized into eight new sub-categories so that the acoustic observations can be compared more easily. These sub-categories are then compared to the ORG data in 1997. The success of precipitation identification from ambient sound is analyzed by wind speed and precipitation category.

Chapter 2

Literature Review

2.1 Introduction

There are many applications involving sound in the ocean. Most of these applications are active: that is, a pulse of sound is emitted from a source and changes in the signal are noted at a receiver. The most familiar of these applications is Sound Navigation and Ranging (SONAR), which entails locating objects in the water through the detection of reflected sound. This simple technology has many oceanographic applications: for example, it can be used to study ocean currents using Acoustic Doppler Current Profilers (ADCPs), to measure ocean depths via depth sounders and to find fish. In addition, variations in the travel time of sound through the ocean can be measured via an array of hydrophones to measure the ocean's temperature (as in acoustic tomography).

Limitations are placed on these applications by the background sound in the ocean, specifically referred to as ambient sound. Ambient sound in the ocean is the sound a hydrophone (or an underwater microphone) in the absence of artificial sound sources. Knowledge of the magnitude and location of the source of ambient sound in the ocean is important in hydro-acoustic applications because in active

applications sound at the receiver other than the active signal (the 'ping') must be minimized. As a result, ambient sound has historically been classified as 'noise' along with electrical and mechanical noise from the apparatus. While some authors refer to this background sound in the ocean as ambient noise, others are more deliberate in their description and make the distinction that this signal is not 'noise' but rather sound generated by an identifiable source.

There is additional value in knowing the magnitude and location of ambient sound (e.g., the infinite plane of dipole sources at the surface generated by wind), in that the directionality of the ambient sound can be used to create passive sub-surface images (Potter 1993). This application is called Ambient Daylight ^{TM} (Potter 1993). and works in a similar fashion as ensuring a bright light source is behind the photographer and in front of the subject in photography.

While knowing the wind speed and the rainfall rate *a-priori* is important for active hydro-acoustic applications and passive imaging one question remains: can the ambient sound signal be interpreted confidently enough to determine surface meteorological conditions accurately?

The measurement of the wind speed at the ocean surface is important because the wind stress at the surface transfers momentum from the atmosphere to the ocean. Since the wind stress at the surface of the ocean varies approximately in proportion to the wind speed squared, accurate measurements of wind speed are needed. Ocean storms provide momentum transfer from the atmosphere to the ocean which leads to significant mixing of water properties throughout the water column. Precipitation is another important ocean surface process; it provides a fresh water input to the seas and oceans. This input is an important component influencing convection. sea-

7

ice formation and the large-scale thermohaline circulation. However, 80% of the precipitation is over the oceans, where only 10% of the weather stations are located (Nystuen 1986). Many of these weather stations are located on islands which affect the weather systems which pass over them. Subsequently, there is an immediate need to study precipitation and storms as they occur in the open ocean with no land masses present to affect them.

It is difficult to collect this meteorological data at sea. Some problems associated with using surface buoys to collect wind speed and rain-fall data are: waves, ice, spray and submersion. Specifically, measuring wind speed at the ocean's surface is difficult because of the troughs created by waves. Ship-mounted anemometers must be deployed with care to ensure there is no interference by the superstructure with the wind measurements. The threat of ice forming on surface buoys and pack ice damaging equipment are potential problems in colder climates. In addition, rain-gauges and disdrometers are subject to spray and possible submersion, making accurate measurements difficult.

Both wind stress and precipitation cause characteristic ocean sounds which can be used as an alternative means of studying these ocean surface processes. Subsurface listening systems have an additional advantage over surface deployed instruments, in that they spatially average over an area of radius equal to the depth of the instrument.

2.2 Sound In Water

To begin with we must define the physical phenomenon known as sound. Sound in a fluid (or solid) is the longitudinal motion of particles in that medium. Any mech-

8

anism which causes a change in pressure creates sound in a compressible medium. Often in oceanography, the ocean is assumed to be incompressible. However, if the medium were incompressible, the speed of sound would be infinite in that medium, so in ocean acoustics this assumption in not reasonable. The rate of change in pressure defines the frequency of the sound and the frequency determines how the sound wave interacts with its surroundings. The sound wave is a progression of areas of compression and rarefraction. An area of compression is where particles are pushed closer together compared to when the sound wave is absent, while rarefraction is an area where the particles are further apart than in the absence of the sound wave. An example of a longitudinal wave similar to sound waves can be demonstrated in a stretched spring: bunch a number of coils together at one end, and upon release this area of compression travels the length of the spring.

There are numerous sources of sound in the ocean, ranging from sounds made by living organisms to sounds created by breaking waves. Table 2.1 presents some sources of underwater ambient sound and the frequencies over which they are generated.

Frequency	Source
10-100 Hz	Microseism
50-500 Hz	Shipping
1-20+ kHz	Wind
10-20+ kHz	Precipitation
1-10 kHz	Fish and Crustaceans
50+ kHz	Thermal Noise

Table 2.1: Examples of sources and frequency ranges of underwater sound.

To study the characteristics of ocean ambient sound, the generation and prop-

9

agation of sound in salt water must be explained. To begin, consider the generation and propagation of sound in fresh water.

2.2.1 Generation and Propagation of Sound

A time-dependent pressure can propagate as either a plane or spherical wave. Following the approach of Burdic (1984), consider an infinite plane at x_0 in yz, and apply a force in the x-direction. For a plane wave, assume that the applied pressure is equal over the whole plane. As a result, there will be a slight change in volume to the right of the plane, with the plane moving some distance $\Delta\xi$ along the x-axis. The change in volume is $y\,\Delta\xi$ and the strain is then

$$\frac{\Delta V}{A} = \Delta\xi. \tag{2.1}$$

The stress is given by the change in pressure and the ratio of stress to strain is given by the bulk modulus B. The change in pressure, Δp, resulting from the displacement $\Delta\xi$ can be written as

$$\Delta p = -B\,\Delta\xi. \tag{2.2}$$

If the change in plane position is dependent on x and if $\Delta\xi \ll 1$, then the pressure is given by

$$p = -B\frac{\partial\xi}{\partial x}. \tag{2.3}$$

Using Newton's second law

$$F(x,t) = -m\,a(x,t), \tag{2.4}$$

$$\frac{\partial\,p(x,t)}{\partial x} = -\rho\,\frac{\partial\,u(x,t)}{\partial t} \tag{2.5}$$

where u is the velocity of the plane. Strain will also be time varying. The time derivative of Equation 2.3 becomes

$$\frac{\partial p}{\partial t} = -B \frac{\partial}{\partial t} \frac{\partial \xi}{\partial x} \qquad (2.6)$$

where

$$u(x,t) \equiv \frac{\partial \xi(x,t)}{\partial t} \qquad (2.7)$$

Changing the order of differentiation in Equation 2.6, and substituting Equation 2.7 in as the time rate of change of ξ gives

$$\frac{\partial u}{\partial x} = -\frac{1}{B} \frac{\partial p}{\partial t} . \qquad (2.8)$$

Using the time derivative of Equation 2.8 and Equation 2.5, then we can find the one dimensional wave equation:

$$\frac{\partial^2 p}{\partial x^2} = \frac{\rho}{B} \frac{\partial^2 p}{\partial t^2} . \qquad (2.9)$$

Using standard differential equation solutions there exists a forward and backward traveling wave with the form

$$p(x,t) = p_1 \left(t - (x + k_1) \sqrt{\frac{\rho}{B}} \right) + p_2 \left(t + (x + k_2) \sqrt{\frac{\rho}{B}} \right) \qquad (2.10)$$

where p_1 and p_2 are arbitrary functions, k_1 and k_2 are the wave numbers for the functions, and the wave speed is $c = (\frac{B}{\rho})^{\frac{1}{2}}$. Note that c is not the speed of the particles since in a longitudinal wave there is no net translation of the particles, but rather the speed of the energy propagation.

The pressure can be generalized in three dimensions as

$$\nabla^2 p = \frac{1}{c^2} \frac{\partial^2 p}{\partial t^2} . \qquad (2.11)$$

The plane wave solution is a special case of Equation 2.11 where the partial derivatives with respect to z and y are both equal to zero. In general, for spherical waves it is convenient to represent the solution in spherical coordinates. Doing so gives

$$\bigtriangledown^2 p = \frac{\partial^2 p}{\partial r^2} + \frac{2}{r}\frac{\partial p}{\partial r} = \frac{1}{c^2}\frac{\partial^2 p}{\partial t^2} \tag{2.12}$$

which is equivalent to

$$\frac{\partial^2 r p}{\partial r^2} = \frac{1}{c}\frac{\partial^2 r p}{\partial t^2} . \tag{2.13}$$

Solutions to Equation 2.13 are of the form

$$p(r,t) = \frac{1}{r}f_1\left(t - \frac{r+k_1}{c}\right) + \frac{1}{r}f_2\left(t + \frac{r+k_2}{c}\right) \tag{2.14}$$

where f_1 and f_2 are arbitrary functions, k_1 and k_2 are the wave numbers for the functions, and the wave speed is $c = (\frac{B}{\rho})^{\frac{1}{2}}$.

It must be noted that both the diverging and converging spherical waves dissipate as $\frac{1}{r}$, whereas the plane wave does not. Also, the converging wave has a singularity at $r = 0$ that is generally ignored in acoustic modeling, with the arbitrarily large pressure at $r = 0$ for the outgoing wave handled by the acoustic displacement at r being small with respect to r (Burdic 1984).

2.2.2 Relaxation Processes

A more realistic model of sound passing through water includes a time-dependent relaxation parameter in addition to Hooke's law in Equation 2.3. This time-dependent addition models the delay in the pressure change caused by the passing pressure front as a result of three physical processes. These processes are thermal relaxation, structural relaxation and chemical relaxation. Physically, they represent changes in

12

vibrational or rotational energy, changes in phase or structure, and ionic dissociation corresponding to periods of rarefaction and compression.

Adding the relaxation effect to Equation 2.3 makes the pressure change take the form

$$\Delta p = c^2 \, \Delta \, \rho + b \, \frac{d\Delta \rho}{dt} \tag{2.15}$$

where b is constant. Using Equation 2.15, Equation 2.13 becomes

$$\frac{\partial^2 \, \Delta \rho}{\partial x^2} + \tau_r \, \frac{\partial^2 \, \Delta \rho}{\partial x \, \partial t} = \frac{1}{c^2} \, \frac{\partial^2 \, \Delta \rho}{\partial t^2} \,. \tag{2.16}$$

This equation can be solved if a solution of the form

$$\Delta \rho = \rho_s \, e^{i \omega t} \tag{2.17}$$

is assumed. Substituting this assumed solution into Equation 2.16 gives

$$\frac{\partial^2 \rho_s}{\partial x^2} (1 + i \, \omega \, \tau_r) = -\frac{\omega}{c^2} \, \rho_s \,. \tag{2.18}$$

The spatial behaviour of density ρ_s, can be assumed to vary as $\rho_s \propto e^{-(ik + \alpha_e) x}$, with k being the wave number. Using the spatial dependence in Equation 2.18, and by considering real and complex components separately, the exponential attenuation rate is

$$\alpha_e = \frac{\omega^2 \, \tau_r \, c_p}{2 \, c^2 \, (1 + \omega^2 \, \tau^2)} \,. \tag{2.19}$$

Assuming $c = c_p$, where c_p is the phase speed, and defining a relaxation frequency $f_r = \frac{1}{2 \pi \tau_r}$, the exponential relaxation parameter can be written as

$$\alpha_e = \frac{(\pi f_r / c) \, f^2}{f_r^2 + f^2} \tag{2.20}$$

13

with units of nepers per meter. For frequencies less than f_r the attenuation is proportional to f^2 and approaches a constant for frequencies above f_r.

The relaxation time is found by considering the case where a pressure of Δp is applied until $t = 0$, at which point the pressure is released and from then on $\Delta p = 0$. In this case, Equation 2.15 becomes

$$\frac{d(\Delta \rho)}{\Delta \rho} = -\frac{c^2}{b} dt \qquad (2.21)$$

and is integrated to give

$$\Delta \rho = \Delta \rho_0 e^{-t/\tau_r} \qquad (2.22)$$

$$\tau_r \equiv \frac{b}{c^2}. \qquad (2.23)$$

where τ_r is the relaxation time parameter.

2.2.3 Effect of Salinity and Temperature on the Speed of Sound

In addition to the effects that salinity and temperature have on the relaxation parameters and therefore the frequency dependent absorption of sound, both salinity and temperature directly affect the speed of sound in water. The temperature of the ocean ranges from -4 to 30°C, while the salinity varies from 32 to 35 practical salinity units (psu). The variability in temperature and salinity occurs in both horizontal and vertical directions and must be considered in ocean acoustics.

While some oceanographic applications assume that the ocean is an incompressible medium, this assumption is not applicable to ocean acoustics. If ocean water was incompressible, the speed of sound in the ocean would be infinite. The compressibility of water is affected by the temperature and, to higher orders, by salt

14

content. In addition to temperature and salt content, the speed of sound increases with increasing pressure (i.e., the depth in the ocean). Pickard and Emery (1996) give an empirical equation for the speed of sound as

$$c = 1449 + 4.6\,T - 0.55\,T^2 + 1.4\,(S - 35) + 0.017\,D \tag{2.24}$$

where T is the temperature in degrees Celsius, S is the salinity in psu, and D is depth in metres (m). The speed of sound in water increases with T, S, and D, and this combination leads to a variety of speed of sound distributions with depth, where $c = c(z)$.

One common result of the stratification of density in the ocean is the formation of sound channels. Sound refracts as it encounters a change in density and, as a result, it changes direction as it passes through the ocean. Consider a two-layer system: sound traveling downward from the upper layer would refract as it entered the second medium. If the lower medium had a larger speed of sound than the upper layer, the sound would bend towards the vertical, as dictated by Snell's law. On the other hand, if the medium below had a lower speed of sound, the downward traveling ray would bend towards the horizontal. To illustrate this, sound can be modeled using ray theory, in which a sound wave is represented by a line perpendicular to the wave fronts (the ray), pointing in the direction propagation of the wave front. Using ray theory and an infinite distribution of layers with the density in each layer decreasing with depth, the sound would refract towards the horizontal for each plane it passed through, so that a downward traveling ray would bend and eventually travel upward. If the density increases with depth then a downward traveling ray would progress towards traveling straight downwards.

A typical sound-speed profile and sound channel are shown in Figure 2.1, taken

from Clay and Medwin (1977). All sound originating at the depth of the density
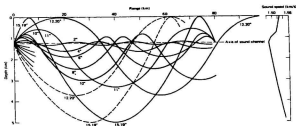
Figure 2.1: Sound refraction due to vertical distribution of the speed of sound, as shown in Clay and Medwin (1977).

minimum would be trapped in the channel. The temperature and salinity distribution therefore has a tremendous impact on ocean acoustics and the interpretation of ambient sound. The concentration of air bubbles in the water also affects the speed of sound in water (see Brekhovskikh and Lysanov (1991, pp 238), §2.3).

2.3 Scattering and Absorption of Sound by Air Bubbles in Water

The presence of air bubbles near the water surface is relevant to the study of ambient sound. Their importance at the surface is threefold. First, individual bubbles generate sound when they are created or deformed. The intensity of sound from acoustically active bubbles at the surface is magnified by the surface which is a perfect reflector and, as a result, the bubbles emit sound as a dipole source (see §2.3.2). Second, bubbles are efficient scatterers of sound at their resonant frequency. A large

16

number of bubbles at the surface, common in near shore surf zones but also in the open sea during high winds, can result in large attenuation at certain frequencies. Third, the presence of bubbles increases the void fraction (the ratio of air to water in a given volume) which changes the speed of sound. As a result, there exists the possibility of a wave guide present at the surface.

2.3.1 Breathing Mode Frequency

As noted, bubbles are efficient sound scatterers, particularly at resonance, and emit sound when they are created or when they are given energy through mechanical deformation. To examine resonant frequency, a spherical bubble of radius a, which is much smaller than the wavelength of the sound wave in water, is considered. Following the approach of Brekhovskikh and Lysanov (1991), the incoming pressure intensity p_i and the outgoing pressure p_s are assumed to have the form

$$p_i = A\, e^{-i\omega t} \tag{2.25}$$

$$p_s = \frac{B}{R}\, e^{i(kR - \omega t)} \tag{2.26}$$

where A and B are amplitudes to be determined from boundary conditions, R is a radius from the centre of the bubble to some arbitrary point, ω is the angular frequency, and $i = \sqrt{-1}$. Assuming the incoming pressure is incident from far enough away that it can be considered planar, it acts equally over the whole bubble removing any spatial dependence in Equation 2.25. Consider the adiabatic case, where

$$p\, V^\gamma = constant\,. \tag{2.27}$$

17

The time-dependent volume change from the initial volume V_0 caused by the incoming pressure change p_i, is given by

$$\frac{dV}{dt} = 4\pi a^2 \frac{dr}{dt} = 4\pi a^2 v_r \tag{2.28}$$

where v_r is the radial component of the velocity at the surface of the bubble and a is the radius of the bubble. The time derivative of the adiabatic Equation 2.27 is

$$\frac{1}{p_0}\frac{dp}{dt} = -\frac{\gamma}{V}\frac{dV}{dt}. \tag{2.29}$$

From the time-derivative of Equation 2.25 and Equations 2.28 and 2.29

$$p = \frac{3\gamma p_0}{i\, a\, \omega} v_r \tag{2.30}$$

since $V = \frac{4}{3}\pi a^3$.

If shear viscous stresses and surface capillary tension can be neglected, then the boundary conditions are

$$p = p_i + p_s \tag{2.31}$$

$$v_r = v_i + v_s \tag{2.32}$$

where v_i and v_s are the velocity components due to the incoming and outgoing pressure fields respectively. Recall that the radius is smaller than the wavelength of the incoming sound. As a result the acoustic pressure is constant over the surface of the bubble. This means

$$\rho v_i \propto \frac{\partial p_i}{\partial R} \ll 1. \tag{2.33}$$

As a result. $v_r = v_s$, where v_s is given by the rate of change of p_s with respect to R.

18

Equating 2.30 to 2.31, and substituting

$$v_r = v_s = \frac{\partial p_s}{\partial R} \tag{2.34}$$

the amplitude of B with respect to A is given by

$$A + \frac{B}{a} e^{ika} = -\frac{3\gamma p_0}{\rho \omega a^3} B \left(ika - 1\right) e^{ika}. \tag{2.35}$$

Note that $ka \ll 1$, and $e^{ika} \approx 1 + ka$ so

$$B = \frac{aA}{\frac{f_0^2}{f^2} - 1 - ika}, \tag{2.36}$$

where

$$f_0 = \frac{1}{2\pi a} (3\gamma \frac{p_0}{\rho})^{\frac{1}{2}}. \tag{2.37}$$

In the ocean, pressure can be approximated by

$$p_0 = 10^5 (1 + 0.1 z), \tag{2.38}$$

where z is the depth in metres, and p_0 is the pressure in Pascals (Pa). For an ideal gas

$$\gamma = 1.4. \tag{2.39}$$

The density of the ocean can be approximated by

$$\rho = 1025 \frac{kg}{m^3}, \tag{2.40}$$

and as a result Equation 2.37 for the ocean becomes

$$f_0 = \frac{327}{a} (1 + 0.1 z)^{\frac{1}{2}} \tag{2.41}$$

19

where a is the radius of the bubble expressed in centimetres, and z is the depth of the bubble in metres.

Any bubble which is not created symmetrically will oscillate and emit sound at the frequency f_0, as it is driven by pressure forces to become spherical. f_0 is the breathing mode frequency of a bubble (also called the Minnaert frequency, the resonant frequency). The energy centred at the resonant frequency is governed by the damping parameters which are discussed in §2.3.3. The damping parameter is equal to the width of the resonant peak divided by the peak frequency (Clay and Medwin 1977, pp 198). The damping parameter is discussed in §2.3.3. Figure 2.2 shows the resonant bubble radii for frequencies from 1 to 72 kHz.
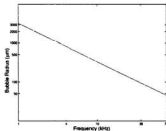
Figure 2.2: Bubble radius in μm and corresponding Minnaert frequency in kHz.

2.3.2 Dipole Source: Bubbles Near a Perfect Reflecting Surface

Acoustically active bubbles entrained by breaking waves at the surface will remain close (within an acoustic wave length) to the surface due to buoyancy forces. As a result, the effects of the ocean's surface on acoustic sources near the surface must be investigated.

The surface of the ocean is a near perfect acoustic reflector because of the large density difference between air and water. Consequently, oscillating bubbles near the surface of the ocean radiate sound in a dipole pattern in the far field. The bubble and its reflection in the ocean's surface are two closely spaced sources as viewed by a receiver at a depth much larger than the separation of the bubble and it's image. Figure 2.3 from Clay and Medwin (1977, pp 452) shows this geometry.
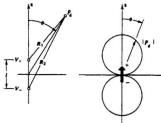
Figure 2.3: Geometry of a dipole source: two monopole source separated by $l \ll k$, where k is the wave number, taken from Clay and Medwin (1977).

The mathematical summation of the two sources gives

$$p_d = p_+ + p_- .$$ \hfill (2.42)

As a result of the density difference between air and water, the surface acts as a pressure release surface. The image will be exactly out of phase with the bubble, so that

$$p_d = \frac{i \, \rho_A \, \omega \, V}{4 \, \pi} \left(\frac{e^{i \, (\omega \, t - k \, R_1)}}{R_1} - \frac{e^{i \, (\omega \, t - k \, R_2)}}{R_2} \right) .$$ \hfill (2.43)

When $R \gg l$, where l is the separation between the source and its reflection (or, in general, the two sources), $R_1 = R_2 = R$. Assuming that the receiver is sufficiently far from the sources, then

$$p_d = \frac{i \, \rho_A \, \omega \, V}{4 \, \pi \, R} \, e^{i(\omega \, t - k \, R)} \, 2 \, i \, \sin \left(\frac{k \, l}{2} \cos \phi \right) .$$ \hfill (2.44)

The coefficient in front of the *sine* term is the pressure of the monopole source for $ka \ll 1$ at $R \gg a$. When the wave number is much less than the separation between the source and its image (or more generally the separation between two sources), then,

$$|p_d| = |p_m| \, k \, l \, cos \phi .$$ \hfill (2.45)

For the dipole sources listed in this thesis, the monopole intensity (or pressure) and the $k \, l \ll 1$ term will be incorporated into an I_0 term, so that only the cosine squared directionality is modeled. This model is reasonable since all bubbles will be close enough to the surface to ensure $k \, l \ll 1$.

2.3.3 Scattering Cross-Section

Not only do bubbles generate sound when they are created or deformed but they also scatter sound, particularly at their resonant frequencies. To describe the acoustical power scattered by the bubble or, more aptly the acoustical power scattered through a surface normal to the direction of the incident wave, it is useful to define the scattering cross-section of the bubble. By definition, the scattering cross-section is the ratio of incident acoustic power to outgoing acoustic intensity. Mathematically, this is defined by

$$\sigma_s = \frac{W_s}{I_i} = 4\pi R^2 \frac{I_s}{I_i}. \tag{2.46}$$

Substituting

$$I = \frac{p^2}{2\rho v} \tag{2.47}$$

into Equation 2.46, σ_s can be expressed by

$$\sigma_s = \frac{4\pi a^2}{(\frac{f_0}{f})^2 - 1 + (ka)^2}. \tag{2.48}$$

If heat exchange and viscous shear are neglected and the radius of the bubble is much less than the wavelength of incoming sound, then the effective scattering size is more than 20 000 times its geometric size. It should also be noted that if f is much less than the resonant frequency f_0, then σ_s approaches zero since the scattered energy drops rapidly with $f - f_0$. If the frequency is much greater than the resonant frequency then the cross-section is at most four times the geometric area, since $ka \ll 1$ for bubbles at resonance ($ka = \frac{f \cdot 207}{f_0 1300}$).

Realistically, the thermal conductivity of water cannot be neglected and the scattering and absorption of energy by bubbles is neither purely adiabatic nor isothermal. In fact, as volume decreases the temperature must increase. The exchange of

23

temperature happens before the volume can increase again. As a result, there is a phase difference between the pressure and temperature fluctuations and the fluctuations in volume. In other words, when volume is at its minimum, pressure and temperature will be less than their maximum. To model this behaviour, let gamma in Equation 2.29 be a combination of real and imaginary components given by

$$\gamma = \gamma_1 - i\,\gamma_2\,. \tag{2.49}$$

As a result, the pressure given in Equation 2.30 becomes

$$p = \frac{3\,(\gamma_1 - i\,\gamma_2)\,p_0}{i\,a\,\omega}\,v_r\,. \tag{2.50}$$

The initial pressure p_0 is the sum of the hydrostatic pressure, and the capillary pressure. The new initial pressure is given by

$$p_0' = p_0 + 2\,\frac{\alpha}{a} \tag{2.51}$$

where α is the surface tension, which can not be neglected for tiny bubbles where the volume fluctuations are not adiabatic.

For a real bubble the shear viscous stresses which act at the surface of the bubble in the radial direction must be considered. Viscous stresses result in

$$-2\,\eta\,\frac{\partial(v_i + v_s)}{\partial R}\bigg|_{R=a} = -2\,\eta\,\frac{\partial v_s}{\partial R}\bigg|_{R=a} \tag{2.52}$$

since the incident velocity is the same over the whole radius of the bubble. Equation 2.52 gives a new boundary condition at $R = a$ for pressure,

$$p = p_i + p_s - 2\,\eta\,\frac{\partial v_s}{\partial R}\,. \tag{2.53}$$

24

Solving for B now gives

$$B = a A \left(\frac{\overline{f_0}^2}{f} - 1 - i \delta \right) \tag{2.54}$$

where

$$\overline{f_0} = \frac{\gamma_1}{\gamma} \chi f_0 \tag{2.55}$$

$$\chi = 1 + \frac{2\alpha}{p_0 a} \tag{2.56}$$

$$\delta = \delta_r + \delta_\eta + \delta_t = k a + \frac{4\eta}{\rho_w \omega a^2} + \frac{f_0^2}{f} \frac{\gamma_2}{\gamma_1} . \tag{2.57}$$

The individual deltas are the damping parameters due to re-radiation (δ_r), viscosity of seawater (δ_η), and the damping due to thermal conductivity (δ_t). Below 100 kHz, δ is dominated by the damping parameter due to thermal conductivity (Brekhovskikh and Lysanov 1991). Figure 2.4 shows the relative magnitudes of the damping parameters, from Brekhovskikh and Lysanov (1991).
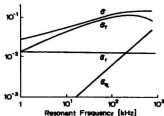
Figure 2.4: Magnitudes of the damping parameters, from Brekhovskikh and Lysanov (1991).

25

The real scattering cross-section can be written as

$$\sigma_s = \frac{4\pi a^2}{D^2 + \delta^2} \tag{2.58}$$

where

$$D = \frac{f_0^2}{f} - 1 \tag{2.59}$$

When considering total energy absorbed or scattered by a real bubble we must consider energy lost to thermal conductivity and shear viscosity. These losses are incorporated in an absorption cross-section defined in a similar way to the scattering cross-section. Both the scattering cross-section and the absorption cross-section can be combined to define the energy loss to an incident wave due to scattering from the bubble and absorption by the bubble. Incident wavelengths comparable to the scattering cross-section, and the absorption cross-section will be affected by the bubbles.

When considering the consequence of bubbles in the water column due to breaking waves, the ramifications of many bubbles with different radii must be considered. The distribution of bubbles of different sizes creates the need to refer to a volume scattering coefficient and the need to examine dispersion effects on the sound velocity.

Interactions between bubbles can be ignored when the average spacing between the bubbles is less than the larger of the wavelength of sound or the square root of the scattering cross-section. To examine the volume effects, consider n bubbles of radius a in a unit volume. The total power is

$$W_s = n\,\sigma_s\,I_i. \tag{2.60}$$

26

If there is a distribution of bubble sizes in the volume, then the integral of the volume scattering coefficient over the range of sizes must be calculated. As a result, the intensity of sound decreases by the following relation

$$dI = -\beta I \, dr \tag{2.61}$$

where β is the integral over the range of bubbles of $n(a) \sigma_s$. One solution to Equation 2.61 is

$$I(r) = I(0) \, e^{-\beta r}. \tag{2.62}$$

$I(r)$ is the acoustic intensity of the sound wave after traveling some distance r from the source $I(0)$ through the layer of bubbles, which absorbs and scatters energy in an exponential decay with β.

2.4 Sources of Ambient Sound

As Table 2.1 showed, there are many potential sources of ambient sound at various frequencies. Wind-generated ambient sound has a large bandwidth, extending from a few hundred Hz (300 Hz) to at least 72 kHz. Ambient sound dominated by precipitation extends from 10 to 25 kHz. Despite fifty years of research, both the source and exact behaviour of the spectra of ambient sound are poorly understood. However, enough is known that the wind speed at the surface can be estimated empirically from the ambient sound. Additionally, it is well known that periods of rain can be identified from the ambient sound spectra; in fact, the rainfall rate can also be determined (Medwin et al. 1992). What still needs to be addressed is the time scale over which accurate observations of wind speed and rainfall rate can be measured via ambient sound, and the effects of hydrophone depth on these measurements. In

27

addition, the effects of time or spectral averaging still need to be quantified. Finally, the exact spectral behaviour over the entire range of frequencies for wind-generated and precipitation-generated ambient sound has not been identified.

2.4.1 Ambient Sound Produced By Breaking Wind Waves

Ambient sound in the ocean extends over a large spectral range. It is generally accepted that thermal noise dominates the spectra at frequencies higher than 50 kHz (Burdic 1984; Urick 1967). Mellen (1952) derived the formula for thermal noise by considering the number of compressional modes of vibration in a cubical box of volume V. The frequency density of normal modes can be used to get the energy per unit volume from the equipartition theorem. For an omnidirectional hydrophone, the expression derived in Mellen (1952) can then be transformed to

$$NL = -15 + 20 \log f \qquad (2.63)$$

where NL is the thermal noise level in dB and f is the frequency in kHz. Sound intensity levels are often reported in dB to allow addition and subtraction operations to replace multiplication and division (see Clay and Medwin (1977)).

For frequencies below 50 kHz the first description of ambient wind-only sound was given by Knudsen et al. (1948), who noted a 5 dB/octave (equivalent to 19 dB/decade) decrease in the ambient sound level with frequency. The sound intensity peaked at 300 Hz and extended to 30 kHz. In addition, the intensity of ambient sound levels were observed to be directly related to the wind speed. Figure 2.5 shows a spectral plot of thermal noise and the ambient sound for different sea states, as given by Urick (1967).

Wenz (1962) confirmed this wind-speed-ambient-sound relation and proposed

28
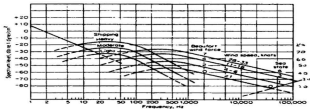
Figure 2.5: Ambient sound spectra for various sea states (Urick 1967). The numbers on the right vertical axis are the SSL in dB re: $1\ \mu Pa^2\ Hz$.

that the cause of wind-generated ambient sound might be oscillating bubbles entrained by breaking wind waves. Other hypotheses for the cause of wind-generated ambient sound included ocean spray (Wilson 1980) and shattering bubbles in breaking waves (Kerman 1984).

A common theme for all hypothesis relating to the source of wind-generated ambient sound is bubbles. Banner and Cato (1988) showed video evidence demonstrating the mechanism for the generation of ambient sound is bubbles entrained by breaking waves. The first attempts to capture the acoustic emissions from breaking waves in flumes were conducted by Banner and Cato (1988), Mellville and Rapp (1989) and Papanicolaou and Raichlen (1988). The flumes suffered from reverberation, so absolute noise levels were unobtainable, however Banner and Cato (1988) showed convincing high speed photographs of bubble production and the corresponding acoustic signal. Continuing this work, Medwin and Beaky (1989) presented absolute spectra from breaking waves in a flume with waves generated by an oscillating plunger, so that bubbles associated with the breaking waves had no association with wind. The bubbles produced a spectrum with a 5dB/octave decay from 1 to 20 kHz.

29

Medwin and Beaky's (1989) conclusions are still important to the study of wind-only ambient sound. They noted that while the far field intensity varies with the depth of the hydrophone squared (h^{-2}), the area of observable sources at the surface as seen by the receiver also varies with h^2. The increased number of observable sources at the surface for increasing depth of receiver cancels the energy loss due to spherical spreading from an infinite plane of dipole sources at the surface. In their paper, they summarized years of ambient sound research by saying

"There is a long history of ocean noise being 'instantly' sensitive to the onset of winds. Since wave height depends on the fetch and duration of the wind, it is not the wave height that is crucial to ocean noise; it is the presence of breaking waves. This was clearly evident in the laboratory experiments [. . . whose] implications [are] that the ocean noise in the frequency range 1 to 20 kHz, and perhaps at higher and lower frequencies as well, is due to wind-only through the mediation of the spilling breakers which are the sources of the sound-radiating bubble." (Medwin and Beaky 1989, p 1129)

To fully understand wind-only ambient sound, three types of wave breaking processes must be considered. The first is the 'plunging breaker', which is the type of wave breaking seen crashing in the surf zone. It occurs when the amplitude of the wave grows to the point where gravitational forces overwhelm the wave and results in catastrophic breaking of the wave. The second type of wave breaking is the 'spilling breaker.' This type of wave breaking is similar to the plunging breaker except that it occurs on a longer time scale. Also, only the crest of the wave breaks and, in essence slides down the front of the wave. The third type of wave breaking

involves 'microbreaking', as outlined by Updegraff and Anderson (1991). This type allows for parasitic capillary wave action on swell waves to entrain bubbles at the onset of low magnitude wind speeds. It is microbreaking which is responsible for ambient sound at low wind speeds. This threshold is no doubt related to the onset of ambient sound which occurs at wind speeds less than the wind speed threshold of white capping.

Aside from variations in the SSL produced by precipitation (see §2.4.2), Farmer and Lemon (1984) noted deviation from Knudsen wind-only behaviour: a decrease in signal at 14.5 and 25 kHz for wind speeds greater than 10 $m\ s^{-1}$ when compared to the SSL at 8 kHz. From the apparent decrease in the ambient sound levels at high frequencies, the extinction radii of bubbles was calculated, and provided evidence of a resident bubble layer. Relevant to the creation of a resident bubble layer is the hypothesis that the bubble size distribution near the surface can be modeled by a power law. To this end, the exponent on the power law for bubble size distribution was calculated from the ratio of the attenuation of the signal at two frequencies, and was compared to the relation determined by Johnson and Cooke (1979) and Kolovayev (1976). The experimental exponent from Farmer and Lemon's (1984) study was between the values recorded by these two studies.

Near-surface bubble size distributions are of the utmost importance as they scatter sound, affect the speed of sound, and generate wind-only sound. Initial measurement techniques concentrated on photographic methods, until a linear acoustic technique for sizing bubbles was presented by Medwin (1977). Several bubble sizing studies were compared by Wu (1981). These early studies (Kolovayev 1976; Johnson and Cooke 1979; Medwin 1977) showed many differences. Medwin (1977) admits

31

that his results may have been skewed by biological activity, while other factors such as temperature differences and the influence of the bubble trap apparatus on the bubbles may also have been the reason for the observed differences.

Although there has been further study of bubble size distributions, there is still not a clear understanding of the distributions which exist in the open ocean. Several other methods exist to measure bubble sizes *in situ*; for example, methods based on non-linear acoustics (Leighton 1994) and acoustic resonators (Farmer et al. 1998). Further discussion of bubble sizing techniques can be found in Melville et al. (1995).

The presence of a bubble layer in winds above $4\ m\,s^{-1}$ has been confirmed (Dahl and Jessup 1995; Crawford and Farmer 1987). Dahl and Jessup (1995) observed a significant increase in the backscatter intensity from the surface for wind speeds above $4\ m\,s^{-1}$ using ADCPs. The backscatter intensity increases with wind speed as the resident bubble population grows. As waves break and inject bubbles into the water column, the plume of bubbles remains as wave breaking increases the bubble population at the surface changes from pockets to a wide layer at the surface.

Capillary gravity waves also produce acoustically active bubbles. In an anechoic wave tank, production of these bubbles was observed at wind speeds greater than $14.6\ m\,s^{-1}$, and the spectra covers a broad frequency range (from a few kHz to 100 kHz, and peaks at 4 kHz) (Kolaini et al. 1994). The exact spectral shape of the observed spectra does not reflect the shape of *in situ* spectra because no bubble layer is allowed to build. From the histograms of bubble size distributions the most frequently occurring bubble radius is 0.1 mm. which corresponds to a resonant frequency of 32 kHz, while the distribution is centred around bubble radius 0.2 mm.

which corresponds to a resonant frequency of 16 kHz. Increasing the salinity increases the number of smaller radii bubbles compared to the distribution of bubbles observed in freshwater (Kolaini 1998).

Before there was conclusive evidence indicating the source of ambient sound or exhaustive research on the correlation of wind speed and ambient sound Shaw et al. (1978) suggested, although only qualitatively, that wind speed could be derived from ambient sound through empirical calculations. Since then, there have been many studies confirming this relation. Vagle et al. (1990) and Evans et al. (1984) have derived empirical equations relating the ambient sound to wind speed. Existing wind speed estimation data are limited by the range in wind speeds, and the frequencies over which the ambient sound is recorded.

Of the existing studies, the Frontal Air-Sea Interaction Experiment (FASINEX) (Vagle et al. 1990) is the most comprehensive. Many other data sets were employed in calibrating the algorithms used to exclude shipping noise and precipitation sound. The wind speed estimating equations are also tested on the various other data sets. One of the conclusions from this experiment was that there exists a critical frequency beyond which the ambient-sound-wind-speed-relation no longer exists, and that this frequency is dependent on wind speed. The relation for the critical frequency f_c with wind speed is given by

$$\log f_c = 1.9 - 0.07 \, U \tag{2.64}$$

where U is the wind speed.

The data collected in FASINEX were limited to frequencies below 25 kHz, and wind speeds of 16 $m \, s^{-1}$. In addition, the ambient sound data were not corrected for reflections off the ocean floor, and the meteorological data is measured either away

33

from the hydrophone or is measured at the surface where interactions with wave crests can be problematic.

Nystuen and Selsor (1997) present ambient sound and wind speed data collected using Acoustic Noise Sensors (ANS) drifters set to drift in the Pacific ocean. Comparison using Vagle's wind speed estimate from ambient sound equation are made to satellite observations. The ambient sound wind speed estimates show correlation ($r = 0.91$) with the satellite estimated wind speeds.

Despite the general agreement of the wind speed from ambient sound equations, a comprehensive study with wind speeds ranging from 0 to 20+ $m\,s^{-1}$ and recorded sound frequencies from 1 to 72 kHz is required to confirm the accuracy of the wind estimates at all wind speeds. Additionally, the time or spectral averaging necessary for accurate wind estimates must also be investigated. Coincidental to the study of the wind from ambient sound equation for various frequencies, the behaviour of ambient sound spectra over the entire range of wind induced ambient sound must be determined.

2.4.2 Ambient Sound Produced by Precipitation

Pumphrey et al. (1989) provided a brief look at the previous research on the sound produced by a falling drop of water onto a surface of water. This research dated back to Worthington's flash photography (1890) of falling drops on water. Several theories were postulated by Bragg (1920) and Mallock (1919), but the accepted theory was finally given by Minnaert (1933) who provided the breathing mode frequency derivation of gas bubbles in liquid that are the source of the sound generated by falling drops. Minnaert proposed that the sound of running water comes from bub-

34

bles. To come to this conclusion, he adapted the theories provided by Bragg and Mallock, who described the airborne sound of drops hitting water (see the discussion in (Franz 1959) for the references).

Franz's (1959) high-speed movie photography provided excellent pictures of the process of falling drops on water as well as the sound produced by the bubble entrainment and impact of the drop. In this study, the sound generated by the falling drops was described as a sharp pulse attributed to the initial impact accompanied by a slower sinusoidal decaying sound wave generated by entrained air bubbles. The entrainment of these bubbles was described as erratic. In addition, these oscillating bubbles were observed to be dipole sources of sound. Franz noted that the sound levels were proportional to drop size and impact velocity. He also provided results from some experiments in the sound generated by spray. In this part of the study, Franz noted that for bubbles with a radius of 0.24 cm, a canopy of water formed which prevented bubble formation. The overall sound spectra has a broad frequency range that extended from 1 to 10 kHz.

In their study of heavy rainfall, Heindsman et al. (1955) found that the absolute sound levels are 77 dB re 1μ Pa for frequencies from 1 to 10 kHz. Further, Bom (1969) plotted the log of rainfall rates from 1 to 25 $mm\,hr^{-1}$ against the sound level and found a linear relation. He also speculated that the sound level depends on the drop size and impact velocity. Lokken and Bom (1972) reported that drop size varies with the rainfall rate, so that the ambient sound spectra reflects the distribution of drop sizes in the precipitation. Changes in ambient sound with drop size are not simple: the spectral character as well as the intensity of the generated sound changes with changing drop size.

Given that raindrop size changes the acoustic signature and that the rainfall rate changes the drop size, in principle it should be possible to determine the rainfall rate from the acoustic signature. An algorithm to determine rainfall rates from the acoustic signal was developed by Nystuen (1996). This algorithm involved using a matrix of known spectrum generated by raindrops of certain sizes. It also gave an inverse method to determine the spectral density of drop sizes and subsequently a formula for calculating the rainfall rate (Medwin et al. 1992).

The general shape of the spectra for light rainfall was described by Scrimger et al. (1987) as a narrow peak centered about 15 kHz, with a steep slope of approximately 60 dB/octave on the low frequency ascent and a slower 9 dB/octave decline on the higher frequency side of the peak. Observed to 50 kHz, this slope is quite different from Knudsen's wind-only slope of 5 dB/octave. This description of the sound from rainfall also highlights the fact that the acoustic signature of snow and hail are distinct from each other as well as from liquid precipitation.

The frequency of the spectral peak is shifted by wind and by surface waves (Nystuen 1990). Wind affects the impact velocity as well as the angle at which the drop strikes the surface. This angle changes the energy released on impact. The upward velocity and phase of the wave also affect the impact velocity. If there is an equal probability that rain drops will strike the wave at any point, the sum of the drops hitting the wave at all phases causes a broadening of the spectral peak. In fact, the peak is dependent on drop impact velocity, and the spectral peak location is given by

$$F_p = 13.4 \frac{v_t}{v_p} \tag{2.65}$$

where F_p is the frequency in kHz, v_t is the terminal velocity of the drop (dependent on

drop size), and $v_i = \sqrt{v_t^2 + v_w^2}$, with v_w the upward component of the oceans surface due to wave action (Nystuen 1987). The spectra Scrimger et al. (1987) described, and the shift with wind speed as Nystuen (1987) noted, are shown in Figure 2.6, taken from Nystuen and Selsor (1997).

Figure 2.6: Ambient sound spectra for various meteorological conditions, taken from Nystuen and Selsor (1997).

Oğuz and Prosperetti (1992) showed that certain velocities and drop sizes will produce a conical crater in the surface of the water and that this crater will always entrain a bubble. Bubble entrainment is dependent on the shape of the impact crater; bubbles which do not have the correct drop size will not create a crater suitable for bubble entrainment. By plotting the terminal velocity of the drops corresponding to the drop radius, the intersection yields a region of rain drop sizes which will entrain bubbles provided there is no wind; i.e., they impact at zero angle to the surface of the ocean (Medwin et al. 1992; Pumphrey et al. 1989). In addition, for large enough drops (e.g. diameter greater than 2.2 mm), a jet of water forms which can subsequently entrain a bubble after drop impact. The entrainment by these jets is dependent on the angle at which the jets hit the surface, with increased probability of

entrainment corresponding to the increase in angle of the jet with the water (Medwin et al. 1992).

Precipitation can be identified from the spectra by plotting the SSL at high frequencies (e.g., 20 kHz) against the SSL at 8 kHz. The resulting scatter plots show a linear low-wind speed region, where the wind-only Knudsen spectral slope is obeyed and a high wind speed region where the magnitude of this critical wind speed varies with frequency (Vagle et al. 1990). Above the critical wind speed a resident bubble layer begins to attenuate the sound. Periods of precipitation can be identified by increased sound levels at 20 to 25 kHz with respect to sound levels at 8 kHz (Nystuen 1986) as shown Figure 2.7.
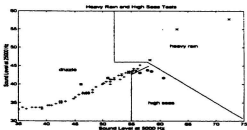
Figure 2.7: A precipitation identification scheme using the elevated sound levels at 25 kHz relative to 8 kHz, taken from Nystuen and Selsor (1997). 'High seas' marks the wind speeds when bubble attenuation affects the ambient signal.

Medwin et al. (1992) provide the most detailed description of the sound signal produced by drops of different sizes. Their results and definitions of bubble types are given in Table 2.2. Medwin et al. (1992) classify the bubbles created on impact

38

Medwin	Diameter (mm)	Notes
Miniscule	≤ 0.8	No sound
Small	$0.8 \leq D \leq 1.1$	Type I
		range 12-21 kHz
		dipole
		bubble production to 10% for incident angle 20
		major component of $0.6~mm~hr^{-1}$ drizzle
Mid Sized	$1.1 \leq D \leq 2.2$	No bubble cavitation
		Impulse signature only
		short lived broad band sound
Large	$D \geq 2.2$	Type II
		primary bubble peak frequency $\propto \frac{1}{r_b}$
		$f = \frac{580}{D} + 0.6$
		f is frequency in kHz, D is drop diameter in mm
		1.8 to 8.5 kHz, for D 4.8 to 2.2 mm

Table 2.2: Rain drop size classification and acoustic profile.

as Type I and Type II. A Type I bubble is "formed at the apex of a conical crater, which is produced by the hydrodynamic force generated by the vertical impact of a small drop onto a smooth, horizontal surface"(Medwin et al. 1992, p. 1614). This bubble is the dominant source of sound in the sea for precipitation with drop size distribution which includes small drops (e.g., those with diameters ranging from 0.8 to 1.1 mm). Larger rain drops (e.g., with diameter greater than 2.2 mm) generate sound through the Type II process. This includes sound produced by the impact, as well as from the oscillation of a large Type II bubble and possible smaller bubbles.

In summary, drops of water less than 0.8 mm in diameter make no sound because the energy of impact is not enough to form a bubble on impact. As the drop size increases the probability of bubble entrainment increases with size, and decreases with increasing wind speed. There is another drop diameter threshold at 1.1 mm. Drops between this size and less than 2.2 mm in diameter, create only

a short-lived broadband sound from the impact and have no cavitation following impact. This is because the crater formed does not have the proper shape to entrain bubbles, therefore they are acoustically undetectable (Oğuz and Prosperetti 1992). Large drops (e.g., those greater than 2.2 mm in diameter) do have a probability of entraining bubbles. For these bubbles, the probability of bubble entrainment increases with increasing wind speed. These bubbles are responsible for sound from 1.8 to 8.5 kHz. The frequency of the sound generated by these drops can be estimated by an empirical relation

$$f = \frac{160}{D^2} + 0.6 \qquad (2.66)$$

as determined by (Medwin et al. 1992). Precipitation has a spectrum of drop sizes and therefore a corresponding spectrum for the sound generated by the drops. To put the drop sizes into perspective, meteorologists classify miniscule drops as less than 0.4 mm in diameter and refer to this distribution as 'Fog'. Drops greater than 0.4 mm but less than 1.0 mm in diameter are referred to as 'Drizzle'. Combining the meteorological definitions with the drop size study, 'Drizzle' should be acoustically detectable, while 'Fog' should not. Rainfall rates dominated by drop sizes from 1.1 to 2.2 mm in diameter should not be acoustically detectable, as no bubbles are entrained following impact.

The acoustic data available for study of precipitation data are limited by the frequency range recorded as well as the wind speeds and the rainfall rates present during the studies. Scrimger's et al. (1987) study is limited to rainfall rates of 10 $mm\,hr^{-1}$ and to wind speeds less than 5 $m\,s^{-1}$, which allows for the isolation of precipitation ambient sound, but does not fully reveal the complexities of the signal at higher wind speeds. Farmer and Lemon's (1984) study measured the ambient sound

40

in shallow water, subsequently an absolute comparison cannot be made. However it must be noted that in their study ambient sound measurements were limited to 25 kHz and recorded only in 5 frequency bins. The wind speeds were less than 15 $m\,s^{-1}$. While Pumphrey et al. (1989) provide well isolated rainfall rates, their experimental results are not from the field. Rainfall rates are produced artificially, and swell and wind waves are not present.

Nystuen (1998) demonstrates the effect of rainfall on freshwater input using data collected for the Acoustic Surface Reverberation Experiment (ASREX) which spanned 87 days in the winter in the mid-Atlantic ocean. In his review, there is evidence of bubble interference during heavy rainfall in high wind, indicated by the lower-than-expected SSL at 20 to 25 kHz for wind-only spectra of similar wind speeds. There is also anecdotal evidence of a reduction in wave height growth during periods of precipitation (Nystuen 1998).

While it is known that wind speed affects the acoustic signature of precipitation, and that precipitation can be identified by the acoustic signature, a complete *in situ* study of the probability of detection from ambient sound is still required. In addition to this categorical gap in the research, the high frequency spectra signature attributed to precipitation has not been thoroughly described.

Chapter 3

Data Processing

3.1 Introduction

Absolute measurements of the intensity levels of ambient sound are modified by several factors. This chapter will examine the following factors: hydrophone response; ocean bottom depth; and hydrophone mooring depth. In the present study, data was collected with the hydrophone moored at two different depths. Increasing the depth of the hydrophone increases the spatial average over which the meteorological estimates are determined using the ambient sound, as well as increasing the path length for the direct sound signal from the surface to the hydrophone. To make absolute comparisons of the estimated Sound Source Levels (SSL) in dB, measured intensities must be adjusted to a 1 m measurement reference depth. In addition, the processed data must account for any additional signal due to reflections and attenuation as the sound travels through the ocean. These potential alterations to the signal are dependent on the temperature of the water, the nature of the reflections at the ocean bottom and the surface, as well as the depth of the water.

The accuracy of the intensity levels recorded by a hydrophone are affected by two factors: the amount of spectral averaging and the amount of temporal averaging

per ensemble. In the present data set, the data was collected at a sampling rate of one ensemble recorded every 3.5 minutes in 1996, and at a sampling rate of one ensemble recorded every 72 minutes in 1997. As such, the 1996 data set can be examined in two ways, as outlined in Chapter 4. One way is to average the data into 10 minute ensembles, and the other is to average into hourly ensembles. These two methods are treated as separate data sets, and are referred to as 1996-10 and 1996-60. The sampling rate directly affects the temporal scale from which comparisons between the estimates from ambient sound can be made to the meteorological measurements recorded by the anemometer, the crew member (via the WMO chart entry), and the Optical Rain Gauge (ORG). The accuracy of the SSL estimates improves with more temporal averaging.

Knowing the uncertainty in SSL measurements is important when describing any of the following: the absolute sound levels which occur at specific wind speeds; the absolute SSL for specific precipitation events; and SSL thresholds. The uncertainty is important so that comparison of the SSL of these properties observed in the present data set can be made to other data sets. In addition, ambient sound in the ocean has been characterized by a spectral slope of between -17 and -20 dB/decade (Knudsen et al. 1948; Wenz 1962; Shaw et al. 1978). The accuracy of the SSL estimates can be used to estimate an uncertainty in spectral slope so that the spectral slope of the present data can be compared to this historical range.

3.2 Sampling Rates and SSL Estimates

In order to measure both the direction of the wind and the wind speed using a sub-surface listening instrument, the OASIS device consists of an Acoustic Doppler

43

Current Profiler (ADCP), and an omnidirectional hydrophone (ITC model number 6050-C). For the purposes of wind speed determination and precipitation detection, only the hydrophone data will be considered.

The instrumentation is designed so that the ADCP and hydrophone are set to 'ping' and record at an appropriate delay in order to avoid any ambient sound signal contamination from the active SONAR transmission of the ADCP. The signal at the hydrophone is digitized at 450 kHz and converted to frequency spectra using a 8192-point FFT algorithm. Data storage constraints preclude recording the entire 4096-point FFT output, so data were averaged into bins using a constant ratio of bandwidth to frequency. For the two data sets considered in this thesis, that ratio was

$$\frac{\Delta f}{f} = \frac{1}{25} \tag{3.1}$$

where Δf is the width of the bin and f is the centre frequency. Data were recorded in 128 bins at frequencies from 1 to 72 kHz.

The confidence interval(ci) of the FFT is given

$$ci = \frac{\nu}{\chi^2_{\nu,\alpha}} SSL \tag{3.2}$$

where $\chi^2_{\nu,\alpha}$ is the χ^2 value for ν degrees of freedom at $1 - \alpha\%$ confidence and the SSL is in $W\,m^{-2}$. The degrees of freedom for a real time-series in a Bartlett window FFT is $\nu = 2 \cdot 3 \cdot N/M$, and here $N/M = 8192/4096$. The uncertainty in intensity levels can be estimated using

$$\sigma_I = (1 - ci)\,SSL \tag{3.3}$$

and is reduced by the averaging necessary to maintain Equation 3.1 which is associated with the data storage constraint. The amount of averaging for each processed

frequency, n_p, is given by

$$n_p = \frac{f}{25} \frac{8192}{450} , \qquad (3.4)$$

The resulting uncertainty in intensity for each recorded ensemble is reduced by the square root of n_p, so that the uncertainty in the intensity levels recorded in one ensemble is

$$\sigma_I = \frac{(1 - ci)}{\sqrt{3}\, n_p} \cdot SSL , \qquad (3.5)$$

since one ensemble is the average of three samples. If further averaging is performed, in principle the uncertainty drops by $\sqrt{n_2}$, where n_2 is the number of ensembles, or frequency bins per average. However, from the averaging used to make the frequency bins, the frequency bins are not independent, so that averaging of bins will not make the uncertainty drop by the square root of n_2. The uncertainty σ_I is converted to dB by

$$10 \cdot \log\left(1 \pm \sigma_I\right) \qquad (3.6)$$

Figure 3.1 shows the uncertainty in SSL for averaging of 3, 17, and 1 ensembles together, corresponding to the 1996-10, 1996-60, and 1997 data sets.
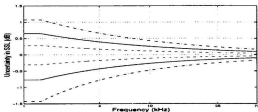
Figure 3.1: The percent uncertainty in ambient sound intensities, with 95% confidence, for 9, 17, and 1 ensembles in each averaged spectra, corresponding to the 1996-10, 1996-60 and 1997 data sets..

A sample wind-only spectrum, recorded during a wind speed of 7.7 $m\,s^{-1}$ where the constant wind-only slope of -19 dB/decade has been removed to decrease the range of the y-axis, is shown in Figure 3.2.
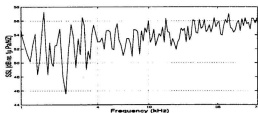
Figure 3.2: Sample spectrum with the -19 dB/decade slope removed, centred about 8 kHz, from the 1997 ambient sound data, recorded during a wind speed of 7.7 $m\,s^{-1}$.

The improvement in SSL estimate with frequency is demonstrated in the spectra shown in Figure 3.2 by the decrease in the random noise peaks from frequency

46

to frequency. For example, compare the ± 3 dB noise in the spectra for frequencies ≤ 4 kHz to the ± 1 dB peaks for frequencies ≥ 35 kHz.

3.3 Spectral Processing

In order to make the SSL deployment independent, so comparisons can be made to other data sets recorded by hydrophones at different depths at different locations, the effects of ocean depth and hydrophone placement must be calculated. The first step in processing, however, must account for the frequency dependent characteristic of the hydrophone (which in the present case differed between deployments).

3.3.1 Calibration of Hydrophone

Regardless of different deployment parameters, the signal from any hydrophone must be corrected for the hydrophone's unique performance characteristic. The ITC-6050-C hydrophones come with a factory calibration, but with the extended ambient sound data from each deployment further calibration was obtained for the hydrophone. The mean from either data set is a wind-generated signal with some constant spectral slope. By examining the mean of the spectra and comparing it to the factory calibration, a new calibration response characteristic for the hydrophone during each deployment was calculated. Figure 3.3a shows the two calibration curves and Figure 3.3b shows the differences between the 1996 and the 1997 deployments. Zedel et al. (1998) explain how the calibration curves are calculated from the data set and compare the 1996 values to the factory and lab calibrations. Figure 3.3b quantifies the difference in the performance of the hydrophone between deployments.

The largest differences between the performance of the hydrophone in the two
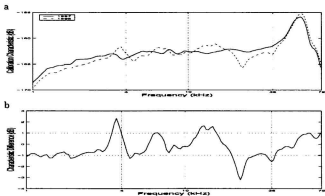
Figure 3.3: a) Hydrophone calibration characteristics for 1997 (solid blue line) and 1996 (dashed red line) deployments. b) Difference between deployments.

deployments occur at 4, 7, 20 and 30 kHz. As Zedel et al. (1998) point out, the difference between field and factory calibration (not shown) comes from the narrow spectral resolution of the OASIS system compared to the factory calibrations. The cause of the difference in performance between deployments is unknown (the same hydrophone was used in 1996 and 1997).

3.3.2 Water Temperature, Hydrophone Depth, and Bottom Depth

In order to make qualitative comparisons between ambient sound data recorded at different depths, the effects of attenuation and additional signal due to bottom reflections must be removed from the SSL (see Chapter 2). To do so, the effects of temperature, hydrophone depth, and bottom depth are investigated.

48

The source of ambient sound in the ocean as generated by breaking waves and precipitation can be modeled by an infinite plane of dipole sources located at the ocean's surface. Each individual dipole source radiates energy as

$$I_d = I_0 \sin^2 \theta \tag{3.7}$$

where I_0 is the equivalent intensity of a monopole source and θ is the angle from the surface. The sound field at depth D, from an infinite plane of dipole sources is determined by integrating over the entire plane and is given by

$$I = \int_{\phi=0}^{2\pi} \int_{r=0}^{\infty} \frac{I_0}{R^2} \sin^2 \theta \, r \, dr \, d\theta \tag{3.8}$$

where R is the distance from the source, r is the radius at the surface, and ϕ is the angle through the plane at the surface. The geometry for the integral in Equation 3.8 is shown in Figure 3.4 with the assumption that there is no refraction. Equation 3.8
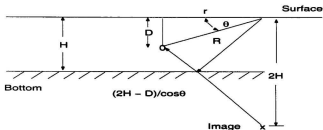
Figure 3.4: Geometry for a source at the surface, a distance of r m horizontally from the hydrophone at depth D m in H m of water.

represents the contributions to the sound field from the direct path from source to

49

receiver, and does not include attenuation due to chemical absorption. If attenuation is included, Equation 3.8 becomes

$$\hat{i} = \int_{\theta=0}^{2\pi} \int_{r=0}^{\infty} \frac{I_0}{R^2} \sin^2\theta \, e^{-\alpha R} \, r \, dr \, d\theta \tag{3.9}$$

where α is the frequency dependent absorption coefficient in nepers m^{-1}, and is calculated from equations A.1, A.3 and A.5 taken from Clay and Medwin (1977) (see Appendix A).

To solve Equation 3.8, the following substitutions are made:

$$R^2 = D^2 + r^2, \tag{3.10}$$

$$\sin^2\theta = \frac{D^2}{R^2}, \tag{3.11}$$

$$r = R\cos\theta, dr = R\sin\theta \, d\theta. \tag{3.12}$$

From these substitutions, it follows that the sound field intensity at depth D, becomes

$$I = 2\pi I_0 \int_0^{\pi/2} \sin^3\theta \cos\theta \, e^{-\alpha D/\sin\theta} \, d\theta . \tag{3.13}$$

An interesting result of this geometry is that the sound from an infinite plane of dipole sources at the surface suffers no losses in intensity due to spherical spreading below the surface. The sound field is dependent only on the depth of the hydrophone through the absorption along the ray paths.

3.3.2.1 Bottom Interactions

Reflections of sound off the ocean floor can add significant energy to the ambient sound levels generated by wind and precipitation for frequencies less than 35 kHz. This fact is true even for ocean depths of 4000 m at sufficiently low frequencies (e.g., less than 10 kHz), and for a broader range of frequencies (e.g., less than 35 kHz) for depths around 1000 m. In shallow water, multiple bounce paths (i.e., sound which

50

reflects off both the ocean floor and the surface) can also increase the ambient sound level.

In order to apply universal wind speed algorithms to either data set, as well as to make comparisons between the two sets, the depth attenuation of the signal and increased signal from bottom reflections must be accounted for. Farmer and Lemon (1984) maintain that in deep water, bottom interactions are not important, however it can be shown that the energy from reflections is significant at frequencies lower than 10 kHz (see Figure 3.7c). The geometry for bottom reflections as well as multiple reflections off the bottom and ocean surface maintain the same geometry as the direct path, and thus use the same trigonometric substitutions thereby eliminating spherical spreading losses.

Figure 3.4 shows the geometry for reflections of the sound off the bottom and surface. The total path length can be calculated by considering the distance to the image from the reflecting surface. The image of the source is located at an additional depth H below the ocean bottom, and is $2H - D$ from the receiver. The path length from the image to the hydrophone is $(2H - D)/\cos\theta$. For multiple reflections off the bottom and the surface, the hydrophone is located $2H + D$ from the image in the surface and the total path length is then $(2H + D)/\cos\theta$. Assuming a loss factor at the surface of γ, and a loss factor at the bottom of β, the equation for the sound field at the hydrophone is now

$$
I = 2\pi I_0 \int_0^{\pi/2} \sin^3\theta \cos\theta \\
(e^{-\alpha D/\sin\theta} + \beta e^{-\alpha(2H-D)/\sin\theta} + \beta\gamma e^{-\alpha(2H+D)/\sin\theta} + \dots) d\theta . \quad (3.14)
$$

This equation assumes that the reflections will maintain their dipole nature.

51

However, variations in the ocean floor and at the surface would scatter the incident sound. A factor of $\sin^2 \theta$, which models the directionality of the dipole, is removed from the terms representing the reflected energy in order to model the random scattering of energy. Moreover, the intensity constant I'_0 for upward traveling energy from the specular reflections must be not equal to the constant I_0 in Equation 3.14 representing the downward traveling energy because energy must be conserved. To derive the relation between these two intensities, consider the energy passing through an infinite plane just above the ocean floor; it must be equal to the reflected energy coming up off the ocean floor. Neglecting the attenuation term in Equation 3.14, the total energy passing down through a point on this plane is

$$2 \pi I_0 \int_0^{\pi/2} \sin^3 \theta \cos \theta \, d\theta = I_0 \frac{\pi}{2} \; . \tag{3.15}$$

The energy passing up through this point on the plane is

$$2 \pi I'_0 \int_0^{\pi/2} \sin \theta \cos \theta \, d\theta = I'_0 \pi \; . \tag{3.16}$$

Since the total energy must be conserved, Equation 3.15 must equal Equation 3.16, so

$$I_0 = 2 \, I'_0. \tag{3.17}$$

The sound field generated by an infinite plane of dipole sources at the surface of the ocean subject to specular reflections within the wave guide and chemical absorption along the ray path at depth D is given by

$$I = 2 \pi I_0 \int_0^{\pi/2} \left\{ \sin^3 \theta \cos \theta \, e^{-\alpha D / \sin \theta} + \right.$$
$$\left. \frac{\sin \theta \cos \theta}{2} \left(\beta \, e^{-\alpha (2 H - D) / \sin \theta} + \beta \, \gamma \, e^{-\alpha (2 H + D) / \sin \theta} + \dots \right) \right\} \, d\theta \; . \tag{3.18}$$

Writing Equation 3.18 using summation notation yields

$$I = 2\pi I_0 \int_0^{\pi/2} \left\{ \sin^3\theta \, \cos\theta \, e^{-\alpha D/\sin\theta} + \right.$$
$$\left. \frac{\sin\theta \, \cos\theta}{2} \left(e^{\alpha D/\sin\theta} \sum_{n=1}^{\infty} \beta^n \gamma^{n-1} e^{[-2\,n\,\alpha\,H]/\sin\theta} + e^{-\alpha D/\sin\theta} \sum_{n=1}^{\infty} \beta^n \gamma^n e^{[-2\,n\,\alpha\,H]/\sin\theta} \right) \right\} d\theta \,. \tag{3.19}$$

Equation 3.19 can be simplified by noting that

$$\sum_{n=1}^{\infty} \beta^n \gamma^n e^{-2\,n\,\alpha\,H/\sin\theta} = \frac{1}{1 - \beta\,\gamma\,e^{-2\,\alpha\,H/\sin\theta}} - 1 \,, \tag{3.20}$$

since $e^{-\alpha} \leq 1$. Rearranging Equation 3.20 using

$$\frac{1}{1 - s} - 1 = \frac{1}{\frac{1}{s} - 1} \tag{3.21}$$

Equation 3.19 becomes

$$I = 2\pi I_0 \int_0^{\pi/2} \left\{ \sin^3\theta \, \cos\theta \, e^{-\alpha D/\sin\theta} + \right.$$
$$\left. \frac{\sin\theta \, \cos\theta}{2} \, \frac{1}{\frac{e^{2\,\alpha\,H/\sin\theta}}{\beta\gamma} - 1} \left(e^{-\alpha D/\sin\theta} + \frac{e^{\alpha D/\sin\theta}}{\gamma} \right) \right\} d\theta. \tag{3.22}$$

Equation 3.22 is a simplified form of Equation 3.18 and solutions to Equation 3.22 can be determined numerically for all frequencies when the solution is called the 'response characteristic' for the deployment. The integrands of equations 3.22 (blue solid line) and Equation 3.13 (red dashed line) are shown in Figure 3.5 for the ambient sound at 1 kHz, a 2 dB bottom loss, no loss in intensity for reflections at the surface and a temperature of 10°C. Incorporating specular reflections off the bottom and multiple reflections from bottom and surface increases the amount of energy incident to the hydrophone. While absolute comparison is not possible using

53
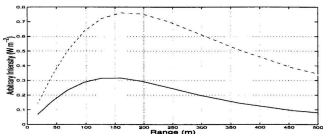
Figure 3.5: the acoustic intensity as a function of range, for no bottom reflections using Equation 3.13 (solid blue line) and including bottom reflections using Equation 3.22 (dashed red line). Both examples had the following parameters: ocean depth of 1600 m, hydrophone depth 250 m, temperature 10°C, $\beta = 0.16$, $\gamma = 1$ and frequency of 1 kHz.

the curves plotted in Figure 3.5, the acoustic intensity when considering reflections is more than double that when reflections are neglected at 1 kHz.

In Figure 3.5 the peak in acoustic intensity is within a circle of radius equal to the hydrophone depth, while in Figure 3.6 the integrand from Equation 3.22 for hydrophone depth 100 m (red dashed line), and hydrophone depth 250 m (blue solid line) are contrasted. This shows the change in location in peak intensities.

The response characteristic can vary with temperature through the absorption coefficient, ocean bottom depth, hydrophone depth, and reflection type (i.e. specular or non-specular). The influence of these components are demonstrated in Figure 3.7, using $\gamma = 1$, and $\beta = .4^2$ which represent 0 and 8 dB loss respectively. The difference in response between dipole reflection (Equation 3.13) at the ocean's bottom and monopole reflection (Equation 3.22) is shown in the Figure 3.7a. The overall

54
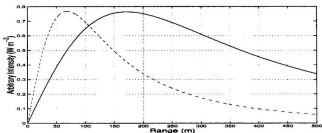
Figure 3.6: The acoustic intensity as a function of range, using Equation 3.22. Hydrophone depths were 250 m (solid blue line) 100 m (dashed red line). In both cases the ocean depth was 1600 m, the temperature was 10°C and the frequency tested was 1 kHz.

difference between specular and non-specular reflections is less than 0.12 dB, starting at 0.04 dB at 8 kHz and increasing to a peak of 0.115 dB at 8 kHz, and decreasing to 0 dB at 35 kHz. Shifting the hydrophone depth while keeping the ocean bottom depth constant has little effect as can be noted by comparing the dashed and solid lines in Figure 3.7a. In contrast, changing the ocean depth while keeping the hydrophone depth constant results in an increasing difference with increasing frequency as illustrated by the green dash-dot line in Figure 3.7a. The increased effect of the nature of the reflections at high frequency is a result of one simple fact: when the ocean depth is 250 m, the high frequencies (e.g., greater than 10 kHz) interact with the bottom before absorption along the path length attenuate the sound level. Minimal difference occurs when the hydrophone depth varies and the ocean depth is large compared to the hydrophone depth (compare the solid blue line to the dashed red line in Figure 3.7a). The reason for this minimal difference is that hydrophone placement largely

55
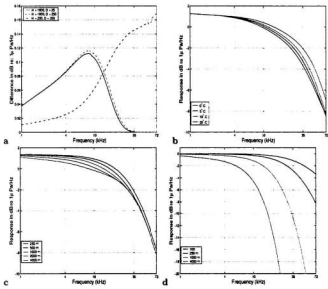
Figure 3.7: a) The difference between the response characteristic when specular and non specular reflections are modelled, for depths of 250 and 1600 m with instrument depth of 25 and 250 m. b) Response characteristics for depth 1600 m and instrument depth 250 m for temperatures of 0, 5, 10 and 20°C. c) Response characteristics for 10°C and instrument depth 250 m for ocean depths of 250, 500, 1000, 2000, and 4000 m. d) Response characteristics for 10°C and infinite ocean depth for instrument depths of 100, 250, 1000, and 4000 m.

affects the direct path to the hydrophone and does not affect the energy reflected off the bottom. The frequency dependence of the difference in additional sound signal from specular and non-specular reflection is a result of the convolution of the increasing effect of absorption and the constant loss in reflection. For each of the examples in Figure 3.7a the difference between reflection type is less than 0.2 dB.

Figures 3.7b to d show how the observed SSL changes as a function of frequency, subject to various parameter changes. Changing the assumed temperature from 0 to 20°C results in an approximate 2 dB change in response at frequencies above 10 kHz (Figure 3.7b).

Ocean depth has a profound effect on the response characteristic as a result of its wave guiding potential. For frequencies higher than 35 kHz and at depths greater than 300 m. the depth dependence vanishes while at lower frequencies the difference is approximately 0.2 dB per depth doubling as can be seen by comparing the 1000 m response to the 2000 m response in Figure 3.7c. The depth dependence vanishes for large enough depths and high frequencies because the absorption effect dominates. The reason for the depth dependence at low frequencies is the increased path length for the reflected rays.

The depth of the hydrophone has little effect on frequencies below 10 kHz, but has great effect on frequencies above 10 kHz, as shown in Figure 3.7d. Here temperature is fixed at 10°C and the ocean bottom is moved to infinity (bottom depth set to 1000 km). It is remarkable that the strength of the signal at depth 4000 m for frequencies less than 10 kHz, indicating that ambient sound measurements made at this depth would still reflect surface phenomenon.

The response characteristics expected for the hydrophone depths, water tem-

perature and ocean depth, for each deployment are shown in Figure 3.8. The red
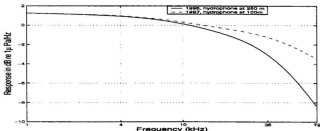
Figure 3.8: Response characteristics calculated for the 1996 deployment (blue solid line) and for the 1997 (red dashed line) deployment with ocean depth 1600 m, hydrophone depth 250 m and temperature 7° C.

dashed line shows the 1997 response, while the blue solid line shows the response for 1996. The difference in the response for the two deployments, which begins at 20 kHz, is 4.5 dB by 70 kHz. This difference is caused entirely by the change in hydrophone depth. Increasing the hydrophone depth increases the length of the direct ray path which increases the effects of chemical absorption. Higher frequencies see greater attenuation due to increasing chemical absorption with increasing frequency.

3.3.3 Sources of Uncertainty in SSL Estimates

The spectral processing necessary to account for the additional signal from bottom and surface reflections add uncertainty to the estimates of SSL. The temperature of the water column is not constant with depth or time, and temperature affects the magnitude of absorption of sound in water. In addition, the ocean floor is quite steep at OWS Mike, changing by 400 m in 10 km, as noted by the depth of 2000 m at the

CTD station, and the depth of 1600 m at the OASIS mooring. The uncertainty in SSL from these two sources of uncertainty will affect the estimates of spectral slope as well.

3.3.3.1 Uncertainty due to Temperature Variation

Recordings taken at OWS Mike show that water temperature covers a substantial range during the course of the deployments. These changes in temperature have the potential to alter the apparent sound spectrum though changes in the response characteristics (i.e., the solution to Equation 3.22). The temperature profile from a signel CTD taken during 1996 shows a range of temperatures for the upper layer of between -1 and 7°C (see Figure 3.9). The time series of temperature profiles from
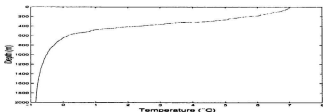
Figure 3.9: Temperature profile from single CTD cast taken at OWS Mike during 1996.

single CTD casts in Figure 3.10 show the surface warming from 6°to 9°C during the 1997 deployment. By calculating the difference between the response curve using a temperature of 12°C and that using 2°C the uncertainty due to temperature changes of $\pm 5°C$ was determined (green dashed line in Figure 3.11). This uncertainty in SSL due to temperature is less than 0.5 dB, and heavily dependent on frequency. A response characteristics using the temperature profile shown in Figure 3.9 was
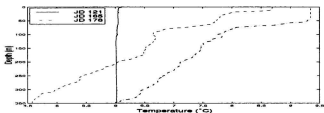
Figure 3.10: Temperature profile evolution for the upper 350 m of ocean during 1997, from single CTD casts taken on Julian Day (JD) 121 (blue solid line), 165 (red dashed line) and 178 (green dashed blue line).

calculated for each deployment. This approach was discarded in favour of using a single representative temperature. These two approaches differed by less than 10%. For 1996, the temperature of the upper layer varied from 0 to 7°C, while in 1997 the mean temperature for the surface is 8.4°C, with a maximum temperature of 9.73°C, and a minimum of 6.00°C. None of the temperature profiles indicate that there would be any significant channeling of sound, as there is no temperature minimum.

The complicated shape of the uncertainty in SSL from temperature is a convolution of the affects due to absorption on the direct and reflected signals.

3.3.3.2 Bottom Interactions

By calculating the effects of bottom interaction at two different depths, while keeping the effect due to absorption constant (i.e., by keeping the temperature the same between the two), the uncertainty in SSL due to any uncertainty in depth is calculated. To account for the slope in ocean bottom, but not to overestimate the uncertainty in SSL, an uncertainty in bottom depth of ± 300 m is assumed. With the temperature fixed at 10°C, the estimate of the uncertainty in SSL from the depth uncertainty is

60

obtained from half of the difference in response between a bottom depth of 1300 and 1900 m, and is shown as the red dashed line in Figure 3.11. The total uncertainty in SSL from uncertainties in depth and temperature is plotted as the solid blue line in Figure 3.11. Maximum differences are less than 0.5 dB and occur at approximately 5 and 35 kHz, as a result of a declining effect from reflections due to absorption of the energy at frequencies greater than 10 kHz; in fact, for frequencies above 35 kHz, it is as if the ocean is infinitely deep.
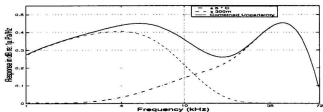
Figure 3.11: The uncertainty in SSL estimates after spectral processing due to uncertainty in temperature (green dashed dot line), and ocean depth (red dashed line) are shown with the combined temperature and depth uncertainty (blue solid line) as functions of frequency.

The confidence intervals from the FFT and the uncertainties calculated here are used later to determine the accuracy with which the spectral slope of the observed ambient sound can be measured. The calculation of this accuracy for the spectral slope is described in the next section, while the observed spectral slopes are described in Chapter 4. In addition, the uncertainty in wind speed estimates from the known sources of uncertainty are compared to the observed error in the wind speed estimates in Chapter 4.

3.4 Uncertainty in Spectral Slopes

While wind-only ambient sound has been characterized with a spectral slope of between -17 and -19 dB/decade (Knudsen et al. 1948; Wenz 1962; Shaw et al. 1978), it has been noted that at wind speeds over 10 $m\,s^{-1}$ the spectrum above 10 kHz loses this slope (Farmer and Lemon 1984). To explore the spectral behaviour over the bandwidth presented here, the spectrum is divided into three regions: 1 to 10 kHz, 10 to 35 kHz, and 35 to 72 kHz. These regions were chosen through visual inspection of the ambient sound spectra. The boundary between the first two Regions is 10 kHz, approximately coinciding with the frequency at which Farmer and Lemon (1984) noted a change in spectral behaviour for high speeds. The boundary between Regions two (II) and three (III) is 35 kHz, and was chosen because of a consistent shift in spectral slope in the observed spectra at this frequency. This frequency corresponds approximately to a bubble production peak between bubbles of diameter 0.1 and 0.05 mm (or from 32 to 64 kHz) caused by capillary waves riding on the crests of gravity waves (Kolaini et al. 1994). It is therefore reasonable to expect the wind-generated ambient sound spectra to extend up to these frequencies. The regions as well as the corresponding frequency range and bin numbers are listed in Table 3.1.

Region	Frequency Range	Bins
I	1-10 kHz	1-64
II	10-35 kHz	65-104
III	35-72 kHz	105-129

Table 3.1: Regions used to determine the spectral slope and the number of frequency bins in each region.

To examine the spectral behaviour of these regions, the spectral slopes of each region are plotted against the wind speed estimate from the SSL (see Chapter 4). The spectral slopes were determined using a linear regression algorithm, which returned the estimated uncertainty associated with each spectral slope. The total uncertainty in spectral slope is the sum (incoherent) of the uncertainty in the spectral slope as determined using linear regression and the uncertainty in the spectral slope from the solid line drawn in Figure 3.11. The uncertainties for each region are listed, the uncertainty in slope from temperature and depth uncertainties (Temp/Depth) and uncertainty from linear regression (Mean Lin Reg), in Table 3.2.

Source of σ(dB/m)	1997			1996-10			1996-60		
	σ_{s1}	σ_{s2}	σ_{s3}	σ_{s1}	σ_{s2}	σ_{s3}	σ_{s1}	σ_{s2}	σ_{s3}
Temp/Depth	0.13	0.12	1	0.13	0.12	1	0.13	0.12	1
Mean Lin Reg	0.92	1.14	1.50	0.54	0.72	1.05	0.24	0.37	0.64
Total	0.93	1.15	1.80	0.56	0.73	1.45	0.28	0.39	1.19

Table 3.2: The mean uncertainty in the spectral slope, in dB/decade, for the random uncertainties in SSL listed as Mean Linear Regression (Mean Lin Reg), and uncertainty in spectral slope, in dB/decade, from the temperature and depth uncertainties (Temp/Depth). The uncertainty σ_{sn} refers to the uncertainty in slope for the spectral Region n_i in Table 3.1).

Time averaging reduces the error from the linear regression by reducing the magnitude of noise in the spectra. The effect of time averaging on the spectrum is illustrated by comparing the sample spectrum for 1996-10 (solid blue line), 1996-60 (red dashed line) and 1997 (green dashed dot line) in Figure 3.12, where 1996-60 has been shifted upwards by 5 dB, and 1997 downwards by 5 dB.
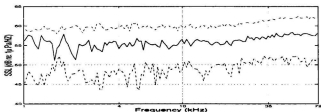
Figure 3.12: Sample spectrum for the 1996-10 (blue), 1996-60 (red dashed), and 1997 (green dashed dot) data sets. The spectrum from 1997 has been shifted down by 5 dB, and the spectrum for 1996-60 has been shifted up by 5 dB. The wind speeds for the three cases were: 1996-10, 7.5 $m\,s^{-1}$; 1996-60, 7.2 $m\,s^{-1}$; and 1997, 7 $m\,s^{-1}$.

3.5 Electrical Noise Floor

When recording ambient sound there are three factors which limit the minimum SSL which can be recorded. The first factor is, as discussed in Chapter 2, thermal noise that dominates at frequencies greater than 50 kHz. In addition, there exists a minimum wind speed below which there is no dominant wind signal. Finally, in any electronic system there is a noise floor, that is, a constant electrical signal from the power source which is erroneously recorded as sound by the hydrophone.

From the ambient sound spectra from 1996-10, for wind speeds less than 3 $m\,s^{-1}$ (red solid line), there is an apparent noise floor in the recorded ambient signal (Figure 3.13). Urick (1967) defines the sound made by the thermal agitation of the water molecules against the hydrophone as thermal noise (Equation 2.63). It has been thought that thermal noise dominates the ambient sound signals for frequencies above 50 kHz (Urick 1967; Burdic 1984).

64
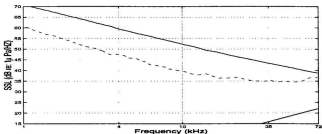
Figure 3.13: Average ambient sound spectra from the 1996-10 data set using wind speeds less than 3 $m\,s^{-1}$(red solid line) and for wind speeds with in 0.5 $m\,s^{-1}$of 8$m\,s^{-1}$(blue solid line). Included is the predicted thermal noise for frequencies from 35 to 72 kHz (solid black line).

Comparing the minimum ambient sound spectra to Equation 2.63 (black solid line) shows that the observed minimum is much louder than the predicted thermal noise at these frequencies. Wind-induced intensities should decrease by 19 dB/decade, however, the SSL for frequencies greater than 10 kHz do not decrease, but rather become approximately constant from 10 to 35 kHz, and increase from 35 to 72 kHz. In addition, the mean ambient sound spectra for the 1996-10 (blue solid line) shows no sign of a noise minimum in the spectra, where the mean wind speed is 8 m/s.

The effects of this noise floor which dominates the signal at low wind speeds are shown for the 1996-60 and 1997 data sets in Figure 3.14. The spectra plotted in Figure 3.14 are the mean spectra for wind speeds less than or equal to 3 $m\,s^{-1}$ for the ambient sound from 1996-10 (blue solid line), 1996-60 (red dashed line), and 1997 (green dash dot line).

The ambient sound spectra from 1996-10 are more sensitive to the noise floor

65
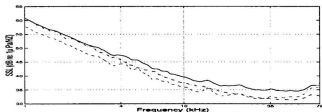
Figure 3.14: The average ambient sound spectrum for wind speeds less than or equal to 3 $m\,s^{-1}$ for the 1996-10 (blue solid line), 1996-60 (red dashed line), 1997 (green dashed dot) data sets.

as a result of the short time interval and limited time averaging (compared to 1996-60). One reason for this sensitivity might be that over short time intervals, when the wind speed oscillates from below the wind speed threshold to above it, the effect of the noise floor are averaged into measured wind-generated spectra, while those recorded over over longer intervals are more likely to record either the noise floor or wind-generated spectra.

Chapter 4

Spectral Relation of Ambient Sound and Wind Speed

4.1 Introduction

It is well known that the wind speed at the ocean's surface can be estimated from the intensity of the ambient sound in the ocean (Wenz 1962; Shaw et al. 1978; Evans and Watts 1982). There are two well known wind speed estimation equations developed by Evans and Watts (1982) and Vagle et al. (1990). Both these empirical relations were designed for use of Sound Source Levels (SSL) at one frequency. The equation from Evans and Watts (1982) is for use with the SSL at 4 kHz (SSL_4), while the equation from Vagle et al. (1990) is for use with SSL_8. Vagle et al. (1990) demonstrate that these equations can accommodate SSL at any frequency f, by adjusting the SSL_f to some reference frequency using the spectral slope of wind-only ambient sound, which is well documented to lie between -17 and -20 dB/decade. Zedel et al. (1998) show that for the present data set, the SSL_2 overestimate the wind speed, and SSL_8 underestimate the wind speed. As a result of this spectral variation in wind speed estimate, they propose using the average SSL from 1 to 10

kHz ($SSL_{\overline{1-72}}$) to estimate wind speed.

The accuracy of the two existing wind-speed-from-ambient-sound equations is determined for two sampling rates, and for three different time averagings. In addition, a new frequency dependent relation is developed. This new relation serves two functions: i) to determine if all frequencies from 1 to 72 kHz can be shifted to some reference frequency and give accurate wind speed estimates; ii) to improve the accuracy in the wind speed estimate obtained using the two existing equations. The wind speed estimates presented here are for time intervals of 10, 60 and 72 minutes. Previous studies have made estimates using 12 hour averages.

The performance of the wind estimating equations is measured by both the mean error in wind speed estimate ($\mu(U_e)$) and the standard deviation in the error of the wind speed estimate ($\sigma(U_e)$). Estimates of the expected $\mu(U_e)$ and $\sigma(U_e)$ are calculated using the uncertainties in the coefficients from the new frequency dependent wind-speed-from-ambient-sound equation, and the uncertainty in estimating the SSL from each data set. The calculation of the uncertainty associated with the coefficients is found in this chapter, while the uncertainty in the SSL measurements were calculated in Chapter 3.

In addition to correlating the ambient sound to the wind speed, the spectral behaviour of the ambient sound with wind speed is investigated for frequencies from 1 to 72 kHz. Farmer and Lemon (1984) noted that for wind speeds greater than 10 $m\ s^{-1}$ the SSL at 14.5 and 25 kHz are less than the SSL at 8 kHz would predict given a constant spectral slope. They proposed that the mechanism for this reduction in high frequency SSL is a bubble layer which builds up during periods of high wind speeds and absorbs energy at frequencies corresponding to the resident bubble size.

68

Vagle et al. (1990) expanded on this observation by noting that for frequencies up to 25 kHz, the wind speed at which the onset of absorption occurs decreases for increasing frequencies. Their observation is represented by Equation 2.64 in Chapter 2. The relation for this critical wind speed as a function of frequency is determined for frequencies from 1 to 72 kHz for the present data and is compared to Equation 2.64.

To investigate the spectral behaviour of ambient sound as a function of wind speed, the ambient sound spectrum has been broken down into three spectral regions. These divisions are based on visual inspection of the present ambient sound spectra in various wind conditions: specifically the frequency noted by Farmer and Lemon (1984) above which high winds attenuate the SSL. Quantitative measurements of the spectral relation to wind speed are presented by plotting the spectral slope of each spectral region as a function of wind speed. This spectral relation to wind speed is also tested for variations in deployment parameters: hydrophone depth; sampling rate; and ensemble averaging.

4.2 Wind Speed Estimate from Ambient Sound

For both deployments which make up the present data set, the wind speed was measured at OWS Mike by a ship-mounted anemometer. Estimates of the wind speed from the ambient sound recorded by the sub-surface hydrophone will be compared to the wind speed recorded at OWS Mike. The ship-mounted anemometer sampled continuously, and recorded the average wind speed every hour. This time averaging of the anemometer improves the correlation to the spatially averaged estimates of wind speed made by the hydrophone.

69

The 1996 ambient sound data was collected from samples taken every 70 seconds and recorded every 3.5 minutes, the 1997 ambient sound data was recorded from samples taken every 24 minutes and recorded every 72 minutes. Therefore, the wind estimates from the ambient sound from 1997 may not be expected to be as strongly correlated to the anemometer data, because the ambient sound was not sampled frequently enough to reflect short term variability in the wind speed.

In 1996 wind speeds were available in 10 minute intervals. Characteristics of ambient sound which change on short time scales are maintained by averaging ensembles into 10 minute intervals. This data is referred to as the 1996-10 data set. One hour ensembles were also formed and will be called the 1996-60 data set.

In 1997, only the hourly averaged anemometer measurements were available, while the ambient sound ensembles were recorded every 72 minutes. Consequently, estimates of wind speed from the ambient sound are compared to the wind speed measurement recorded closest to them in time. For the cases where the wind speed measurement fell in the middle of the time interval between two ambient data ensembles, the measurements of ambient sound and wind speed were discarded.

4.2.1 Determination of a Frequency Dependent Wind Speed Equation

The wind speed estimation equation derived by Evans and Watts (1982) is based on the relationship

$$U_{10} = 10^{A \cdot SSL + B}, \tag{4.1}$$

where A and B are empirical constants. The Equation developed by Vagle et al. (1990) uses the relation

$$U_{10} = \frac{10^{\frac{SSL}{20}} - b}{s},$$ (4.2)

where s and b are empirical constants. In both equations, U_{10} is the wind speed at 10 m height above the ocean surface.

For the remainder of this thesis, the wind speed equations will be referred to as Evans' equation (Equation 4.3), which is the equation from Evans and Watts (1982) shifted to 8 kHz, given by

$$U_{10} = 10^{0.0420 \cdot SSL_8 - 1.33}$$ (4.3)

and Vagle's Equation (or Equation 4.4), given by

$$U_{10} = \frac{10^{\frac{SSL_8}{20} - 80.94}}{52.87}.$$ (4.4)

To determine if shifting the SSL_f to a reference SSL frequency is appropriate, linear regression was used to determine the slope and intercept of the line relating the SSL at a given frequency to the logarithm (base 10) of the measured wind speed. This approach results in frequency dependent coefficients $A(f)$ and $B(f)$, for which the wind speed estimate Equation 4.1 must be modified to

$$U'_{10}(f) = 10^{A(f) \cdot SSL(f) + B(f)}$$ (4.5)

where f is the frequency. Equation 4.5 is different from the approach used for Evans' and Vagle's Equations, where only the constant spectral slope of wind-only ambient sound is used to adjust the SSL.

71

To calculate $A(f)$ and $B(f)$ (referred to as 'the Coefficients'), only those points which did not alter the spectral slope over 35 to 72 kHz from its wind-only behaviour, and those which did not elevate the SSL_{20} with respect to the SSL_8 were considered in the wind speed-ambient sound relation. These criteria eliminated those "contaminated" by precipitation, as will be discussed in Chapter 5. In addition, the SSL at all frequencies other than 8 kHz were adjusted by -19 dB/decade. This correction has the effect of flattening the spectrum by removing the constant spectral slope of wind-only ambient sound, and allows the Coefficients to be calculated as though at an 8 kHz reference frequency (centred about 8 kHz), consistent with Vagle et al. (1990).

Ambient sound is not correlated with wind speeds less than 3 $m\,s^{-1}$ (Vagle et al. 1990; Nystuen 1998); speculation sets the wind speed threshold for the onset of ambient sound to be lower than the wind speed threshold for white-capping, which is approximately 5 $m\,s^{-1}$. Dahl and Jessup (1995) detected a backscatter intensity threshold at 4 $m\,s^{-1}$, indicating the presence of bubbles at the surface at this wind speed. While there is no model describing this wind speed threshold for ambient sound, the present data set exhibits this minimum value between 3 and 5 $m\,s^{-1}$. Noting this characteristic, the Coefficients for Equation 4.5 are determined using wind speeds greater than 3 $m\,s^{-1}$. Wind speeds greater than 15 $m\,s^{-1}$ were included for the calculations of $A(f)$ and $B(f)$ to examine the effects of high wind speed on the SSL at different frequencies.

Figures 4.1a and b shows how Coefficients $A(f)$ and $B(f)$ from Equation 4.5 vary with frequency. There is systematic behaviour between the two Coefficients for each deployment case shown in Figure 4.1. For frequencies less than 10 kHz, there
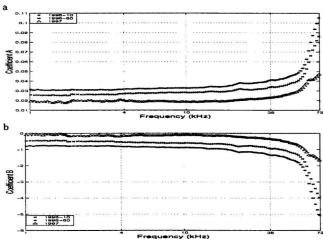
Figure 4.1: a) $A(f)$ and b) $B(f)$ from Equation 4.5. In both plots, the Coefficients were calculated using wind speeds greater than $3\,m\,s^{-1}$, wind-only events, and 'flattened' spectrum centred about 8 kHz. The 1996-10 (blue x), 1996-60 (red *), and 1997 (green Δ) are shown in both a) and b).

are approximately constant values for $A(f)$ and $B(f)$, while a frequency dependence exists for frequencies greater than 10 kHz.

The sensitivity of the estimated wind speed to small changes in the Coefficients is demonstrated in Figure 4.2.

Wind speeds were estimated using the Coefficient values for 8 kHz, and show that for SSL less than 55 dB (corresponding to wind speeds up to $10\,m\,s^{-1}$), the difference in wind speed estimates between any choice of Coefficients is on the order of $1\,m\,s^{-1}$. At these low wind speeds, the estimates using the Coefficients determined

73
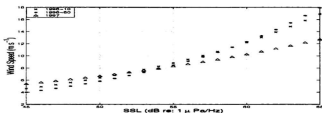
Figure 4.2: Wind speed estimates for SSL from 45 to 65 dB using $A(f)$, and $B(f)$ (from Equation 4.5) determined from the 1996-10 (blue x), 1996-60 (red *) and 1997 (green $\triangle$) data sets.

from the 1997 data are greater than those using either averaged data set from 1996. For SSL greater than 55 dB ($\approx 10~m~s^{-1}$), the difference in wind speed estimates from the ambient sound recorded in 1996 and 1997 increases with increasing SSL (or wind speed), reaching a maximum difference of 5 $m~s^{-1}$ between 1996-60 and 1997. The difference decreases to approximately 0 $m~s^{-1}$ between 1996-60 and 1996-10 for SSL greater than 55 dB. At these higher wind speeds, estimates from both data sets from 1996 exceed those from 1997. The marginal difference between the 1996-60 and 1996-10 data sets is expected, as they are both derived from the same data set.

In order to develop a universal wind estimation from ambient sound equation, the mean of the three Coefficient functions plotted in Figures 4.1a and b are used as the Coefficients in Equation 4.1. The frequency dependent Coefficients which are used in Equation 4.5 for comparison to estimates from Vagle's and Evan's equations

74

are

$$A'(f) = \frac{A_{1996-10} + A_{1996-60} + A_{1997}}{3} \tag{4.6}$$

$$B'(f) = \frac{B_{1996-10} + B_{1996-60} + B_{1997}}{3} \tag{4.7}$$

where the subscripts refers to the data set from which $A(f)$ and $B(f)$ were determined.
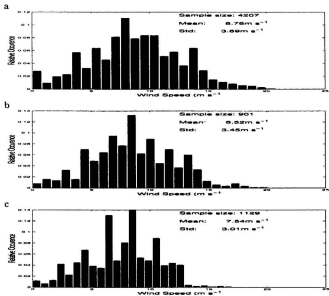
Figure 4.3: Wind speed distributions measured by the ship-mounted anemometer for the a) 1996-10, b) 1996-60, c) 1997 data sets.

In choosing universal values for the Coefficients, it is important to consider differences in wind speed distribution for the various data sets. From Figure 4.3, wind speeds less than or equal to 3 $m\,s^{-1}$ account for 7%, 5% and 6.5% of the distribution of wind speeds for the 1997, the 1996-60, and the 1997 data sets respectively. All deployments have approximately the same percentage of wind speeds below 3 $m\,s^{-1}$, so that any difference resulting from exclusion of wind speeds in this range is not caused by differences in the distribution of wind speeds. However, both the 1996-10 and 1996-60 data sets have more high wind speed events than does the 1997 data set. 10.1% of anemometer readings are greater than or equal to 15 $m\,s^{-1}$ in the 1996-60 data, while the 1996-10 data has 4.7% measured wind greater than 15 $m\,s^{-1}$. In 1997, less than 1% of the anemometer data is greater than or equal to 15 $m\,s^{-1}$.

4.2.2 Comparison of Frequency Dependent and Independent Wind Speed Estimation

The error in the wind speed estimate is given by

$$U_e = U_{OWS} - U_a \tag{4.8}$$

where U_a is the wind speed estimate, and U_{OWS} is the wind speed recorded by the ship-mounted anemometer. Two parameters can be used to measure the performance of each wind speed estimating equation; the mean error in the wind speed estimate ($\mu(U_e)$) and the standard deviation of the error in wind speed estimate ($\sigma(U_e)$). The $\mu(U_e)$ is the mean bias of the estimate and is characteristic of the empirical relation, but can be removed by adjusting parameters. The $\sigma(U_e)$ represents the mean variation of the estimate for all wind speeds and is a measure of the reliability of any estimated wind speed.

76
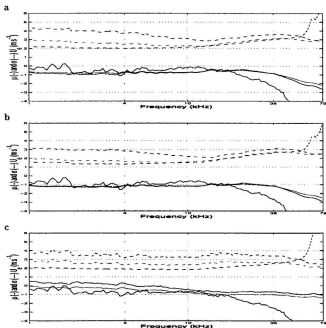
Figure 4.4: The $\mu(U_e)$ (solid) and $\sigma(U_e)$ (dashed) for: a) the 1996-10, b) 1996-60, c) 1997 deployment. In a to c, the results using Equation 4.5 are plotted in blue, Evans' Equation in red, and Vagle's Equation in green.

In Figure 4.4, the wind speed estimates from Equation 4.5 (blue) are compared to estimates made using Evans' (red), and Vagle's (green) Equations by plotting the $\mu(U_e)$ (solid lines) and $\sigma(U_e)$ (dashed lines).

For frequencies from 1 to 10 kHz, estimates from both Vagle's and Evans' equation do not show a frequency dependence in the $\mu(U_e)$. In 1997 there is an approximate 1 $m\,s^{-1}$/decade change in the $\mu(U_e)$. The $\mu(U_e)$ of Equation 4.5 shows no general trend, although there are variations in the mean estimate in this frequency range. For frequencies above 35 kHz all three equations show an increasing overestimation of the wind speed using the 1996-10 and 1996-60 data. Only Equation 4.5 increasingly overestimates as the frequency increases using the 1997 data. Both Evans' and Vagle's equations reach a maximum overestimation of 2.5 $m\,s^{-1}$ in 1996-10 and 1996-60 and 1 $m\,s^{-1}$ in 1997 at 72 kHz.

There are several interesting questions which arise from examining the mean error in the estimated wind speed for each data set. First, if the Coefficients are the mean values of the empirical relations for each data set then why do the mean errors not sum to zero for all deployments? In other words, why is

$$\mu_{1997}(f) + \mu_{1996_{60}} + \mu_{1996_{10}}(f) \neq 0\,, \forall f\,? \tag{4.9}$$

Second, why is there no frequency dependence in the $\mu(U_e)$ for Evan's and Vagle's Equation as Zedel et al. (1998) observed? Third, why do Evan's and Vagle's show no high frequency (greater than 35 kHz) dependent overestimation in 1997? These questions are considered individually.

The sum of the mean errors for all the data sets do not sum to zero because of the non-linear response function of the estimated wind speed (Figure 4.2) and the specific data being used to establish the Coefficients (Figure 4.3).

The frequency dependent mean observed by Zedel et al. (1998) was caused by an inappropriate choice of bottom loss parameters in their model (see Section 3.3.2). By choosing an inappropriate value for signal loss with reflection off the bottom adjusts the calibrated signal incorrectly and introduces a frequency dependence in the mean error. This fact introduces the possibility that the bottom parameters, such as the reflection coefficient, can be determined from the ambient sound at several frequencies from 1 to 10 kHz.

The increasing overestimate with frequencies greater than 35 kHz in 1996 is not present in 1997 because there are fewer high wind speed events in 1997. The high wind speeds of 1996 skew the error because there exists a maximum measurable wind speed for frequencies greater than 35 kHz. This is examined in detail in Section §4.4.1.

Wind estimates for frequencies above 10 kHz will not be considered for the remainder of the thesis. A more complete outline of the problems of using the SSL for frequencies greater than 10 kHz is provided in Section §4.4.1.

If all wind speeds are included, the mean values for $A(f)$ and $B(f)$ using results from each deployment and both time intervals from 1996 over the frequency range 1 to 10 kHz are: $A = 0.042$ and $B = -1.38$. These values are within 1.0% of A, and 3.9% of B from the adjusted version of the equation used by Evans et al. (1984) (Equation 4.3).

The $\sigma(U_x)$ of each equation show little variation for frequencies less than 10 kHz. All equations show an increasing $\sigma(U_x)$ with increasing frequency above 10 kHz for both 1996 data sets, while only Equation 4.5 shows an increase for frequencies above 35 kHz in 1997. The equations can be arranged in the order of decreasing

79

$\sigma(U_e)$: Vagle's Equation, Evans' Equation, Equation 4.5. A more detailed examination of the $\sigma(U_e)$ is included in Section 4.3.3.

4.2.3 Uncertainty in Wind Speed Estimation

The uncertainty in the wind speed estimate has three possible sources: poor correlation at the time/spatial scale over which the measurements were made; uncertainty in the SSL, which in turn has several sources; or a poor model of the ambient-sound-wind-speed relation.

Prior studies have shown that the ambient sound is correlated to wind speeds measured as far away as 55 km (Cato et al. 1995), so the time/spatial scale is unlikely to cause large effects. Unfortunately the effects of spatial averaging and sampling frequency cannot be distinctly separated from time averaging with the present data. The uncertainty in the wind speed estimate introduced by errors in determination of $A(f)$ and $B(f)$ and in the recorded SSL are determined in this section. The accuracy of the model for Equation 4.5 is explored in §4.3.3.

4.2.3.1 Uncertainty: SSL

Zedel et al. (1998) state that using Vagle's Equation accuracy in SSL of 1 dB is needed for a 10% accuracy in wind speed estimation. This estimate is found by differentiating the wind speed estimate from ambient sound equation with respect to SSL. For wind speed estimates using Equation 4.5 the uncertainty in the wind speed estimate is given by

$$dU = U_{10} \cdot A(f) \ln 10 \cdot dSSL. \qquad (4.10)$$

To get the uncertainty in SSL, the confidence intervals from the FFT and the uncertainty from temperature and depth errors must be included (see Chapter 3).

The total uncertainty in the SSL is the sum of the uncertainty in the SSL from the FFT, and the uncertainty from temperature and depth. The total uncertainty is given by

$$dSSL(f) = \sqrt{\sigma_{SSL}^2 + \sigma_{T,D}^2} \qquad (4.11)$$

where $\sigma_{T,D}$ is the combined uncertainty in the SSL due to the uncertainty in temperature and depth (see Figure 3.11), and σ_{SSL} is the uncertainty in the SSL measurement (see Figure 3.1). The $dSSL$, measured in dB, for the 1996-60 (blue solid line), 1996-60 (red dashed line), and 1997 (green dash dot line) data sets are shown in Figure 4.5.
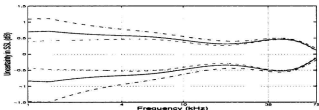
Figure 4.5: The sum of the mean σ_{SSL}, σ_T and σ_D for ambient sound from the the 1996-10 (solid blue line), 1996-60 (red dashed line), and 1997 (green dash dot line) data sets.

4.2.3.2 Uncertainty: $A(f), B(f)$

Zedel et al. (1998) chose to ignore the uncertainty in the estimation of $A(f)$ and $B(f)$, however, small changes in $A(f)$ and $B(f)$ do lead to large differences in wind speed estimates (Figure 4.2). While it is not clear that it is appropriate to consider the uncertainty in $A(f)$ and $B(f)$ as coherent (recall the systematic behaviour

81

shown in Figure 4.1), the uncertainty in SSL from uncertainty in $A(f)$ and $B(f)$ can be estimated by

$$\sigma(U_{10}) = \sigma_A + \sigma_B, \tag{4.12}$$

where

$$\sigma_A = \frac{\partial U}{\partial A} \delta A, \tag{4.13}$$

$$\sigma_B = \frac{\partial U}{\partial B} \delta B, \tag{4.14}$$

and

$$\frac{\partial U}{\partial A} = U_{10} \cdot \ln 10 \cdot SSL(f) \tag{4.15}$$

$$\frac{\partial U}{\partial B} = U_{10} \cdot \ln 10. \tag{4.16}$$

When calculating the Coefficients using regression, the uncertainty in the estimated Coefficients are also calculated. The mean uncertainty for each frequency was calculated from the uncertainty for each of the data sets. For all three data sets the percent uncertainty for $A(f)$ (solid blue line) and $B(f)$ (red dashed line) are shown in Figure 4.6, where the uncertainty in $A(f)$ has been multiplied by 10 to make the scales comparable. The percent uncertainty in $A(f)$ is less than 1% for all frequencies, while the percent uncertainty in $B(f)$ is 3% for frequencies between 1 and 20 kHz. The percent error begins to increase slowly with increasing frequency 20 kHz, reaching 5% at 50 kHz. At 50 kHz the percent error increases rapidly, reaching a maximum value of 12% at 72 kHz. The percent error in A increases rapidly for increasing frequency at 50 kHz, reaching a maximum of 0.2 %.

One source of the uncertainty in the coefficients relating wind speed to the ambient sound levels might be the limited correlation between wind speed and am-
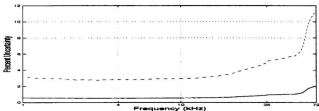
Figure 4.6: The percent uncertainty in $A(f)$ multiplied by ten (blue solid line), and $B(f)$ (red dashed line).

bient sound. Recall that at any given instant the sound recorded by a sub-surface hydrophone may be louder or quieter than the wind speed might indicate. At some time interval, the average SSL recorded by the hydrophone reflects the mean amount of wave breaking which is characteristic of the mean wind speed. Another potential cause for this uncertainty is the potential time lag between any increase in wind speed and the subsequent increase in ambient sound in the ocean.

4.2.3.3 Uncertainty: Wind Speed Estimate

By plotting the uncertainty in the wind speed estimate from both the uncertainty in SSL (blue line) and the uncertainty in $A(f)$ and $B(f)$ (red line) in the same plot, the magnitude of both sources of uncertainty are compared in Figure 4.7. The uncertainty arising from the uncertainty in the SSL has been multiplied by 10. The uncertainties in the Coefficients result in larger $\mu(U_s)$ (solid line) and $\sigma(U_s)$ (red dashed) than do uncertainties in SSL for both 1996-10 and 1996-60 where time averaging of several spectra (3 and 17) reduces the uncertainty in SSL.
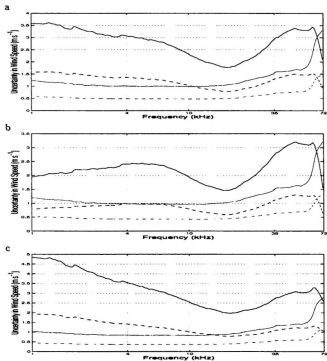
Figure 4.7: The expected mean error in wind speed estimate from both the uncertainty in SSL and the uncertainty in Coefficients $A(f)$ and $B(f)$. The $\mu(U_e)$(solid line), and $\sigma(U_e)$ (dashed line) are both included for the a) 1996-10, b) 1996-60, and c) 1997 data sets.

4.2.3.4 Uncertainty: The Model

The form of Equations 4.3 and 4.5 assumes that the relation between the logarithm of the wind speed and ambient sound is linear. Any systematic error caused by deviation from the assumed model of the ambient-sound-wind-speed relation would result in a wind speed dependent error. For the present data set, the μ and $\sigma(U_*)$ using Vagle's modified form show no improvement over estimates from the form of Equation 4.5. The wind speed from ambient sound equations can be arranged in the order of descending μ and $\sigma(U_*)$: Vagle's Equation; Evans' Equation; and Equation 4.5.

To examine the effects of the magnitude of the wind speed on the wind speed estimate, the error in the wind speed estimate (Equation 4.8) is plotted as a function of the estimated wind speed in Figure 4.8: the precipitation events identified by the algorithms presented in Chapter 5 are plotted in red. In Figure 4.8a, precipitation during high wind speeds leads to more accurate estimates of wind speeds in 1996-10. This phenomenon is not repeated in 1996-60 or 1997, indicating that this phenomenon occurs at a short time scale and is sensitive to both time averaging and infrequent sampling rates. Perhaps the results observed in 1996-10 are caused by additional low frequency (≤ 10 kHz) SSL added by the precipitation signal.

In 1996, the mean wind speed estimate using the SSL from 1 to 10 kHz in Equation 4.5 overestimate wind speed below $10\ m\ s^{-1}$ and underestimate wind speeds above $10\ m\ s^{-1}$, as shown in Figure 4.8a and b. Figure 4.8c shows a similar relation between wind speed and the error in wind speed estimates using the 1997 data. Improved wind estimates using this wind speed dependence in error are included in

85
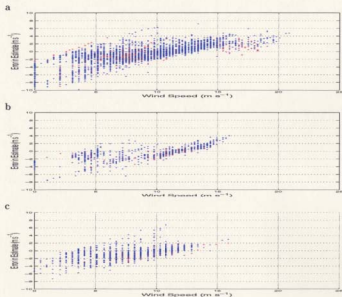
Figure 4.8: Error in mean wind speed estimate using frequencies from 1 to 10 kHz in Equation 4.5 compared to the estimated wind speed, for the a) 1996-10, b) 1996-60, and c) 1997 data sets. Red dots are spectrum contaminated with precipitation as identified by the algorithms in Chapter 5, blue dots are the estimates for wind-only spectrum.

4.3   Improvements in Wind Speed Estimates

If the error in the wind speed estimates were due only to the uncertainty in the SSL estimates, better wind speed estimates could be derived by either spectral averaging or time averaging. Improvements based on time averaging are explored by comparing the results from the three data sets. In addition, the wind speed estimates are calculated using spectral averages of SSL. Both forms of averaging reduce the variation in the wind speed estimate by reducing noise in the ambient sound measurements. Finally, the systematic mean error can be removed by introducing a wind speed dependent correction term.

4.3.1   Spectral Averaging

To reduce the variance in the SSL, the mean SSL is used in Equations 4.3 and 4.4. In general, a non-linear transformation (e.g., the SSL to wind speed equation) has the effect of magnifying variance. As a result, averaging the data before the non-linear operation is more effective at reducing the overall variance than averaging the data after the non-linear operation (i.e., calculating the mean SSL and then computing the wind speed is preferable to computing the mean wind speed from single frequency SSLs). This approach in not an option for Equation 4.5; using the mean SSL in Equation 4.5 would require new values for the constants A and B. Instead, the mean wind speed estimate using the SSL for frequencies from 1 to 10 kHz is used to reduce the variance in that estimate.

The upper bound of the frequency used in either the wind speed average or

the average SSL must be selected accounting for the possibility of signal absorption by bubble clouds at high winds. For the present data this bound has been set to 10 kHz. This frequency threshold for high wind speed corresponds to the frequency noted by Farmer and Lemon (1984). Assuming 'contamination' from shipping sound is not present, the lower bound is set to 1 kHz.

The mean $\mu(U_s)$ and $\sigma(U_s)$ for the estimates obtained using the average SSL or average wind speed estimates are listed in Table 4.1. To determine if the spectral

Deployment	1996-10		1996-60		1997	
Equation	$\sigma(U_s)$	$\mu(U_s)$	$\sigma(U_s)$	$\mu(U_s)$	$\sigma(U_s)$	$\mu(U_s)$
Evans	$2.13 \ m.s^{-1}$	$-0.65 \ m.s^{-1}$	$1.31 \ m.s^{-1}$	$-1.17 \ m.s^{-1}$	$1.82 \ m.s^{-1}$	$-0.19 \ m.s^{-1}$
Vagle	$3.16 \ m.s^{-1}$	$-0.70 \ m.s^{-1}$	$1.57 \ m.s^{-1}$	$-1.17 \ m.s^{-1}$	$2.44 \ m.s^{-1}$	$0.20 \ m.s^{-1}$
Equ. 4.5	$1.93 \ m.s^{-1}$	$-0.42 \ m.s^{-1}$	$1.29 \ m.s^{-1}$	$-0.86 \ m.s^{-1}$	$1.57 \ m.s^{-1}$	$-0.65 \ m.s^{-1}$

Table 4.1: The $\mu(U_s)$ and $\sigma(U_s)$ when the $SSL_{\overline{1-10}}$ is used in Equations 4.3 and 4.4, and the mean wind speed estimate using SSL_1 to SSL_{10} from Equation 4.5. Results for 1996-10, 1996-60 and 1997 are listed.

averaging improved the wind speed estimate at frequencies less than 10 kHz, the difference between $\sigma(U_s)$ obtained using the spectral average and the $\sigma(U_s)$ obtained using SSL_f is considered (Figure 4.9).

$$I_\sigma = \sigma_f - \sigma_a \tag{4.17}$$

where σ_a is the standard deviation determined when wind estimates are obtained using spectral averages, and σ_f is the standard deviation determined using the SSL_f. From this definition, positive I indicates a reduction in the $\sigma(U_s)$ when averaging is used.

88
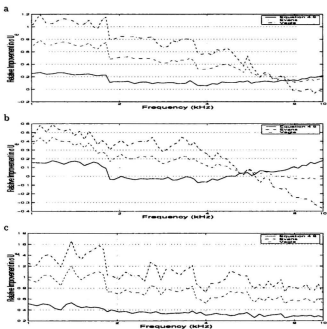
Figure 4.9: The relative improvement in $\sigma(U_s)$ when mean values of SSL and wind speed estimates are used to estimate wind speed compared to the SSL at individual frequencies, using Equation 4.5 (blue solid line), Evans' (red dashed line) and Vagle's (green dash dot line) Equations. Results from the a) 1996-10, b) 1996-60, and c) 1997 data sets are shown.

The reduction in $\sigma(U_e)$ obtained for Vagle's and Evans' equations follow similar trends for frequencies less than 10 kHz in each of the 1996-10, 1996-60 and 1997 data sets. For 1996-10 and 1996-60 there is a decreasing improvement for increasing frequency. Using the 1996-10 data, spectral averaging reduces the $\sigma(U_e)$ obtained using SSL_1 by 1, 0.7 and 0.2 $m\,s^{-1}$ for Vagle's equation, Evans' equation and Equation 4.5 respectively. By 10 kHz, the $\sigma(U_e)$ for both Evan's equation and Equation 4.5 improves by 0.2 $m\,s^{-1}$ while the $\sigma(U_e)$ for Vagle's equation is no better than the estimate obtained using SSL_{10}.

Using the 1996-60 data, spectral averaging reduces the $\sigma(U_e)$ by 0.5, 0.4 and 0.15 $m\,s^{-1}$ for Vagle's equation, Evans' equation and Equation 4.5 at 1 kHz respectively. For frequencies between 2 kHz and 4 kHz, there is no improvement in the wind speed estimate using Equation 4.5. For frequencies above 5 kHz, Evan's equation does not improve when spectral averaging is used, while the $\sigma(U_e)$ from Vagle's equation becomes larger for increasing frequency. The $\sigma(U_e)$ from Equation 4.5 declines with increasing frequency above 5 kHz.

Using the data from 1997, the $\sigma(U_e)$ of Equation 4.5 is reduced by 0.5 $m\,s^{-1}$ at 1 kHz and follows an approximately linear relation with frequency, reaching improvement of 0.3 $m\,s^{-1}$ at 10 kHz. A similar linear relation is obtained for Vagle's and Evans' equations, however they both show identical spectral structure. At 1 kHz the reduction in the $\sigma(U_e)$ is 1.2 and 1 $m\,s^{-1}$ for Vagle's equation and Evans' equation respectively, while at 10 kHz the reduction is 0.8 and 0.6 $m\,s^{-1}$. Examples of the spectral structure are the three peaks at frequencies less than 2 kHz.

Further comparison of the deployments is presented in the next section, however the data sets can be organized by the magnitude of the overall reduction in

90

$\sigma(U_e)$ in increasing order: the 1996-60 data set; the 1996-10 data set; the 1997 data set. Arranging the data set in this way indicates the increasing importance of averaging, as the 1997 data set was recorded with the hydrophone at shallower depth than 1996 (100 m compared to 250 m). In addition, there was no time averaging used in 1997. Unfortunately, the present data set does not allow for the contribution of these variables to be distinctly separated.

4.3.2 Time Averaging

The effects of time averaging on $\sigma(U_e)$ are evaluated by comparing the individual plots for 1996-10 and 1996-60 of $\sigma(U_e)$ in Figures 4.4a and b. To illustrate the reduction of the variation in the estimate, the plot of the standard deviation in the wind estimate using 1996-60 is subtracted from 1996-10 in Figure 4.10.

$$I_\sigma = \sigma_{1996-10} - \sigma_{1996-60} \qquad (4.18)$$
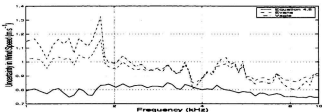
Figure 4.10: The improvement in $\sigma(U_e)$ when 17 ensembles are averaged instead of only 3. using Equation 4.5 (blue solid line), Evans' (red dashed line) and Vagle's (green dash dot line) Equations.

The $\sigma(U_e)$ for estimates using the 1996-60 ambient sound data is lower than

when the 1996-10 data is used for all three equations. Equation 4.5 has a $\sigma(U_e)$ approximately 0.8 $m\,s^{-1}$ smaller than 1996-60 than in 1996-10. Both Vagle and Evans show spectral variation in the improved $\sigma(U_e)$ when 1996-60 is compared to 1996-10. For all the equations, more improvement in $\sigma(U_e)$ is realised through ensemble (time) averaging than through spectral averaging.

From the previous section, the 1996-60 data set, where 17 ambient sound ensembles have been averaged, the reduction in the $\sigma(U_e)$ is the least. This result indicates that the benefits (reduction in variance of the error) of time and specular averaging do not add.

4.3.3 Systematic Wind Speed Correction

Figure 4.8 shows that there is a wind speed dependent error in the wind speed estimate. Vagle et. al. (1990) noted that when winds from 0 to 20 $m\,s^{-1}$ are included the ambient-sound-wind-speed relation is not linear. To eliminate this systematic error, a correction term is added to Equation 4.5 resulting in

$$U_{10} = 10^{A \cdot SSL + B} + \alpha \left(10^{A \cdot SSL + B}\right) + \beta \tag{4.19}$$

The coefficients α and β are determined by linear regression of the wind speed estimate from Equation 4.5 and the error in the estimated wind speed. While this correction term could be calculated for each equation and for each frequency, only the mean estimate using Equation 4.5 for frequencies between 1 and 10 kHz will be investigated. It has been shown that averaging the results using Equation 4.5 in this way has the smallest $\sigma(U_e)$.

The error in the wind speed estimate is plotted against the estimated wind speed (Figure 4.11). Only wind speed estimates greater than 3 $m\,s^{-1}$ are considered.

From the behaviour of the present data, the error can be divided into two separate wind speed regions. These regions are wind speeds less than 10 $m\ s^{-1}$ and those greater or equal to than 10 $m\ s^{-1}$. Frora Figure 4.11 the form of the correction for wind speeds less than 10 $m\ s^{-1}$ is constant at -1.22 $m\ s^{-1}$ in all three data sets. Both
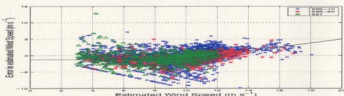
Figure 4.11: Mean wind speed correction term (black solid line) superimposed on the scatter plot of the mean error in the wind speed estimate for the 1996-10 (blue x), 1996-60 (red *) and 1997 (green Δ) data sets obtained using wind only spectrum. Only initial wind speed estimates greater than 3 $m\ s^{-1}$ are included.

α and β were calculated using linear regression for each of the three data sets at wind speeds greater than 10 $m\ s^{-1}$. The results from the individual data sets were then averaged to determine the common correction factor (see solid line in Figure 4.11). For wind speeds greater than 10 $m\ s^{-1}$ the correction factor is -1.22 $m\ s^{-1}$ and increases to 5 $m\ s^{-1}$ at wind speeds of 20 $m\ s^{-1}$.

Deployment:	1996-10		1996-60		1997	
Equation	$\sigma(U_e)$	$\mu(U_e)$	$\sigma(U_e)$	$\mu(U_e)$	$\sigma(U_e)$	$\mu(U_e)$
Eqn. 4.5	1.99 $m\ s^{-1}$	-0.99 $m\ s^{-1}$	1.37 $m\ s^{-1}$	-0.33 $m\ s^{-1}$	1.65 $m\ s^{-1}$	0.13 $m\ s^{-1}$

Table 4.2: The $\mu(U_e)$ and $\sigma(U_e)$ when the SSL_{1-10} is used in Equations 4.3 and 4.4, and the mean wind speed estimate using SSL_1 to SSL_{10} from Equation 4.5. Results for 1996-10, 1996-60 and 1997 are listed.

The μ and $\sigma(U_e)$ using Equation 4.19 for each data set are shown in Table 4.2. While the variance listed in Table 4.2 is greater for both the 1996-10 and 1997 data

93

sets than it is for the spectrally averaged results in Table 4.1, the differences are small. For the 1996-10 data set this difference is only 0.04 $m\,s^{-1}$ (2% of the spectral averaged result), while it is 0.6 $m\,s^{-1}$ (4% of the spectral averaged result) using the 1997 data. Most importantly, the $\mu(U_s)$ has dropped to 0.00, -0.33 and 0.12 $m\,s^{-1}$ from -0.42, -0.86 and -0.65 $m\,s^{-1}$ (see Table 4.1) for the 1996-10, 1996-60 and 1997 data sets.

4.4 Spectral Behaviour for Different Wind Speeds

It has been shown that the behaviour of the ambient sound spectra is not solely governed by Knudsen's - 19 dB/decade relation for frequencies higher than 10 kHz (Farmer and Lemon 1984; Vagle et al. 1990). The following four sub-sections outline the relation between the ambient sound spectrum and wind speed.

Ambient sound levels at all frequencies are more closely correlated to changes in SSL below 10 kHz than they are to the measured wind speed. Accordingly, the corrected wind speed estimate obtained using the mean result from frequencies between 1 and 10 kHz using Equation 4.19 is used to measure the change in spectral slope. For reference, the approximate SSL_8 are included in the plots.

4.4.1 Critical Wind Speed

The critical wind speed is the frequency dependent threshold for which sound levels decrease with increasing wind speed. This decrease in SSL for wind speeds greater than 10 $m\,s^{-1}$ is seen as an inflection point in the scatter plot of the SSL versus the SSL_8. The magnitude of SSL_8 at which the maximum wind-only SSL_f occurs represents the maximum wind speed which can be estimated by SSL_f. Figure 4.12

94

shows sample scatter plots for $f = 35$ kHz for the 1996-60 data set. The inflection point, corresponding to the maximum SSL_f, is indicated by the vertical solid line.
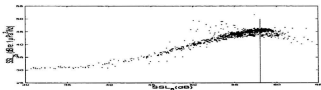
Figure 4.12: Scatter plots of SSL_{35} as a function of SSL_8 (wind speed) for the 1996-60 data set The SSL_8 which occurs at the peak SSL_f value is marked by the vertical line.

To determine the critical wind speed, only 'wind-only' spectra were used to eliminate spectral contamination from precipitation. The mean SSL_8 corresponding to SSL_f values within 1.5 dB of the maximum SSL_f were converted to wind speed using Equation 4.19. For reference, the mean wind speeds measured by the anemometer were also determined. Figure 4.13 shows plots of the critical wind speeds as a function of frequency, for each frequency above 8 kHz, for both 1996-60 (a), and 1997 (b). Plotted with these figures is Equation 2.64 (solid blue line). The wind speed estimates from the maximum SSL_8 are in blue x, while the measured wind speed are in red circles. These figures demonstrate that Equation 2.64 is inaccurate for frequencies above 10 kHz using the present ambient sound data. The critical wind speed approaches a constant value for frequencies greater than 20 kHz. For frequencies from 8 to 15 kHz Equation 2.64 is broadly consistent with the present data. while a second linear relation for frequencies from 10 to 20 kHz is demonstrated by the deviation of the present data from the solid line in Figure 4.13a. Vagle et al.

95

a

b
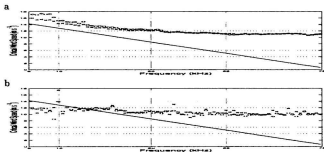
Figure 4.13: The critical wind speed as a function of frequency for the ensembles from the a) 1996-60 and b) 1997 data sets. Included in both plots is Equation 2.64 reprinted from Vagle et al. (1990) as the solid line.

(1990) could not explicitly note this behaviour, as their measurements of SSL extended to only 25 kHz. However, their value for the maximum wind speed at 25 kHz did not fall on the linear relation exhibited by the lower frequencies and would appear to be consistent with the present result.

4.4.2 Spectral Slope From 1 to 10 kHz (Region I)

For wind-only ambient sound, a -19 dB/decade slope is assumed to characterize the spectrum. To investigate if this constant spectral slope is maintained for all wind speeds, the spectral slope from 1 to 10 kHz is plotted against the corrected wind speed estimate using Equation 4.19 and the equivalent SSL_8 in Figure 4.14 for the 1996-10 (a), 1996-60 (b), and 1997 (c) data sets.

In all the data sets, the spectral slope varies from -17 to -20 dB/decade with wind speed. The scatter in the plots comes from the uncertainty in estimating the

96
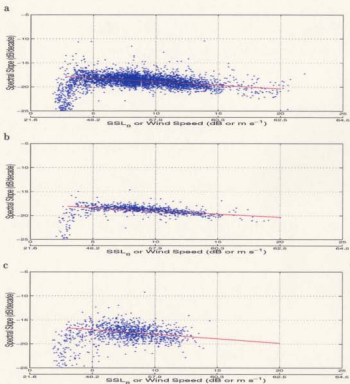
Figure 4.14: The relation of the spectral slope in Region I to the SSL_8 from the a) 1996-10, b) 1996-60, and c) 1997 data sets. The empirical linear fit for wind speeds greater than 3 $m\,s^{-1}$ for both 1996 data sets and for wind speeds greater than 6 $m\,s^{-1}$ for 1997 are included as the red solid line.

spectral slope. From Chapter 3, the uncertainty in the spectral slope in this region for the 1996-60 data set is ±0.28 dB/decade, for 1996-10 is ±0.56 dB/decade, and for 1997 is ±0.93 dB/decade. The decrease in the uncertainty in spectral slope between 1996-60 and 1996-10 is a result of time averaging, and is illustrated by comparing Figures 4.14a to b: there is a substantial reduction in scatter in b.

The mean spectral slope of the wind-only data points in Region I is -18.77 ± 0.56, -18.89 ± 0.28 and -18.10 ± 0.93 dB/decade for the 1996-10, 1996-60 and 1997 data sets. These values are equivalent within uncertainty. The spectral slope of Region I has a characteristic mean spectral slope of -18.6 ± 0.4. However, there is a wind speed dependent decrease in the spectral slope in each data set. This is quantified by a slope (m) and intercept (b) determined using linear regression for wind-only data points (see Figures 4.14a to c). For comparison, these three lines are plotted along with errors specified by the uncertainty in slope (m) and intercept (b) given by

$$\delta = R \cdot \delta_m + \delta_b \qquad (4.20)$$

where R is the range of wind speeds, δ_m and δ_b are the uncertainty in the slope and intercept determined by regression in Figure 4.15. The slope, intercept, δ_m and δ_b values are given in Table 4.3.

In 1997, the data shows more scatter for wind speeds less than 6 $m\,s^{-1}$ than does the data for either 1996 data set (compare Figures 4.14 a to c). Since a linear relation which matched the relation for the 1996-10 and 1996-60 data based on visual inspection of the data plotted in Figure 4.14c, wind speeds less than 6 $m\,s^{-1}$ were excluded for the 1997 data, while only wind speeds less than 3 $m\,s^{-1}$ were excluded for the two data sets from 1996.
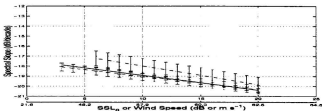
Figure 4.15: The relation of the spectral slope in Region I to the wind speed estimates from Equation 4.19. The approximate SSL_4 is included as a reference and was determined using an inverse method from Equation 4.19.

deployment	m	δ_m	b	δ_b
1996-10 [†]	-0.15	0.01	-17.43	0.06
1996-60 [†]	-0.13	0.02	-17.69	0.15
1997 [*]	-0.19	0.13	-16.10	0.29

Table 4.3: The slope (m) and intercept (b) relating the spectral slope of Region I to wind speed estimates from Equation 4.19 using wind-only data points. The uncertainty in the slope (δ_m) and intercept (δ_b) are included. [†] when estimated wind speeds greater than $3~m~s^{-1}$ are used. [*] when estimated wind speeds greater than 6 $m~s^{-1}$ are used.

4.4.3 Spectral Slope From 10 to 35 kHz (Region II)

The spectral slope from 10 to 35 kHz can be sorted into three distinct wind speed ranges when plotted as a function of the wind speed estimate. These three wind speed ranges are: i) less than 3 $m\,s^{-1}$; ii) between 3 and 10 $m\,s^{-1}$; iii) greater than 10 $m\,s^{-1}$. The spectral slope of Region II is plotted as a function of estimated wind speed in Figure 4.16. The clustered data points greater than 48 dB but less than 58 dB are data points where Nystuen's algorithm detects precipitation and which match the WMO (see Chapter 5). These points are excluded from the mean spectral slopes and the empirical fits of spectral slope to wind speed in order to exclude any contamination from the precipitation dominated spectra.
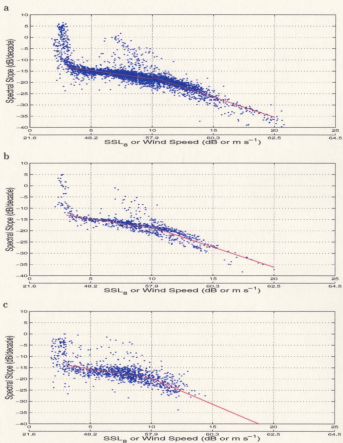
Figure 4.16: The relation of the spectral slope in Region II to the SSL_8 for the a) 1996-10, b) 1996-60 and c) 1997 ambient sound levels. The empirical fit is shown by the red solid line.

It has already been discussed that there is little correlation of ambient sound to wind speeds less than $3\ m\,s^{-1}$, so the first wind speed range will not be quantified. The relation for the remaining wind speed ranges are determined using linear regression as was Region I. As such, the uncertainty in the relations for this Region are also given by Equation 4.20.

The slopes (m) and intercepts (b) for the relation of the spectral slope of Region II with wind speeds between 3 and 10 $m\,s^{-1}$ are given in Table 4.4. By

deployment	m	δ_m	b	δ_b
1996-10	-0.76	0.02	-10.87	0.17
1996-60	-0.84	0.04	-10.52	0.32
1997	-0.83	0.08	-11.46	0.65

Table 4.4: The slope (m) and intercept (b) relating the spectral slope of Region II to the wind speed estimate using Equation 4.19 for wind speeds greater than 10 $m\,s^{-1}$. The uncertainty in slope and intercept (σ_m and σ_b) are included.

visual inspection of Figure 4.16 this relation looks similar to that for all wind speeds of Region I. From Chapter 3, the uncertainty in the spectral slope of this Region is 0.73, 0.39, 1.15 dB/decade for the 1996-10, 1996-60 and 1997 data sets respectively. The mean spectral slope for 1996-10, 1996-60 and 1997 are -16.86 ± 0.73, -17.05 ± 0.39 and -18.10 ± 1.15 respectively. While these mean values are equivalent within uncertainty for this region, only the mean slope of Region II for 1996-60 and 1997 are equivalent to the mean slopes of Region I within the estimated uncertainty. The spectral slope of Region II is characterised by a mean spectral slope of -17.3 ± 0.5 for wind speeds less than 10 $m\,s^{-1}$. This mean spectral slope is different from that of Region I for all wind speeds.

The slopes (m) and intercepts (b) for the relation of the spectral slope of Region

II to wind speeds greater than 10 $m\ s^{-1}$ are given in Table 4.5. By visual inspection of Figure 4.16 this relation is not similar to Region I. Consistent with Farmer and Lemon (1984), there is a decrease in spectral slope corresponding to a reduction in SSL for frequencies between 10 and 35 kHz for wind speeds greater than 10 $m\ s^{-1}$.

deployment	m	δ_m	b	δ_b
1996-10	-1.79	0.02	0.29	0.26
1996-60	-1.78	0.06	-0.60	0.69
1997	-2.30	0.27	3.22	2.92

Table 4.5: The slope (m) and intercept (b) relating the spectral slope of Region II to the wind speed estimate using Equation 4.19 for wind speeds greater than 10 $m\ s^{-1}$. The uncertainty in slope and intercept (σ_m and σ_b) are included.

The relations for both wind speed ranges in this Region are plotted in Figure 4.17 for the 1996-10 (blue solid line), 1996-60 (red dashed line) and 1997 (green dash dot line) data sets. The uncertainty given by Equation 4.20 is shown by the error bars. Based on visual inspection, the relations describing the spectral slope of
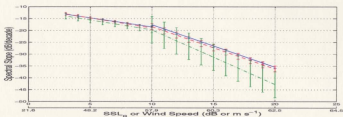
Figure 4.17: The relation of the spectral slope in Region II to the wind speed estimate from Equation 4.19.

Region II is equivalent when comparing the data from 1996 to the data from 1997.

4.4.4 Spectral Slope From 35 to 72 kHz (Region III)

Ambient sound at frequencies above 35 kHz is not well studied. Scrimger et al. (1987) did make mention of the rain signal extending to 50 kHz. Urick (1967), cited in Burdic (1984), postulates that the ambient sound signal at frequencies above 50 kHz is dominated by thermal noise. Figure 4.18 shows a scatter plot of the slope of Region III where a distinct wind speed dependent relation is demonstrated. The clustered data points with spectral slopes less than -20 dB/decade are data points where the Slope algorithm detects precipitation and which match the WMO (see Chapter 5). These points are excluded from the mean spectral slopes and the empirical fits of spectral slope to wind speed in order to exclude any contamination from the precipitation dominated spectra. The relation of spectral slope to wind speed in this Region is determined by fitting a first order polynomial to the data. A polynomial for each data set is shown by the red line in Figures 4.18a to c. These polynomials are described by the coefficients given in Table 4.6 and are compared in Figure 4.19.

Deployment	a	b	c	d
1996-10	-0.03 ± 0.0003	1.13 ± 0.01	-15.11 ± 0.10	42.26 ± 0.30
1996-60	-0.03 ± 0.0009	1.20 ± 0.03	-15.67 ± 0.24	47.43 ± 0.70
1997	-0.06 ± 0.0056	2.00 ± 0.12	-21.76 ± 0.78	56.41 ± 1.52

Table 4.6: The coefficients of the polynomial $ax^3 + bx^2 + cx + d$ relating the spectral slope of Region III to wind speed estimate from Equation 4.19.

Here, the error bars are determined by the uncertainty in the spectral slope of this Region. These values were determined in Chapter 3 to be: $\pm$ 1.45, 1.19 and 1.80 dB/decade for the 1996-10, 1996-60 and 1997 data sets. The wind estimates only extend to 15 $m\,s^{-1}$ for the 1997 data. This places an upper bound on the accuracy of
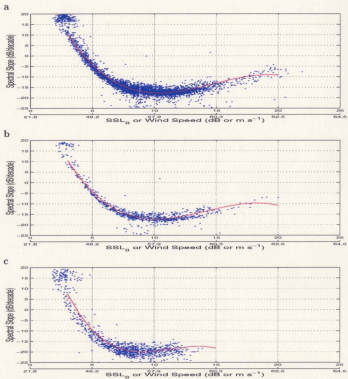
Figure 4.18: The relation of the spectral slope in Region III to the estimated wind speed using Equation 4.19 for the a) 1996-10, b) 1996-60 and c) 1997 ambient sound levels. The empirical fit is shown by the red solid line.

the polynomial describing the wind-speed-spectral-slope relation. For wind speeds
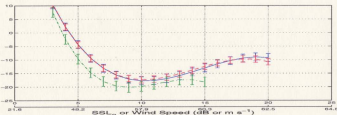
Figure 4.19: The relation of the spectral slope in Region III to the wind speed estimated from Equation 4.19 for the a) 1996-10, b) 1996-60 and c) 1997 ambient sound levels.

between 9 and 13 $m\,s^{-1}$ these polynomials are identical within uncertainty. There is no similarity with the spectral behaviour in this Region to either Region I or II. The difference in behaviour between Region II and Region III may be related to the increase in bubble production of capillary-gravity waves in wind speeds greater than 15 $m\,s^{-1}$ noted by Kolaini et al. (1994). At these frequencies, or for bubbles that are of small enough radius, there is not the same attenuation at high wind speeds as there is for bubbles corresponding to frequencies from 10 to 35 kHz. At bubble sizes corresponding to frequencies greater than 35 kHz there is either less sound being generated at the lower wind speeds (5 to 15 $m\,s^{-1}$), or there is attenuation from a resident bubble layer which forms at lower wind speeds than the resident bubble layer predicted by Farmer and Lemon (1984). There might also be a saturation point for the bubble layer at wind speeds of 10 $m\,s^{-1}$. For wind speeds greater than 10 $m\,s^{-1}$ perhaps the bubble sources are mixed below the resident acoustic absorbing bubble layer.

106

4.5   Conclusions

It has been shown that the SSL for frequencies from 1 to 10 kHz shifted to a reference frequency of 8 kHz provide accurate wind estimates using the wind-speed-from-ambient-sound equations of Evans and Watts (1982) and Vagle et al. (1990). Determining individual relations for each frequency (from 1 to 10 kHz) results in smaller variation in the error of the wind speed estimate when compared to Evans' and Vagle's equations. All three equations produce a mean error in the wind speed estimate in this frequency range of approximately 1 $m\,s^{-1}$. The variance in the wind speed estimate for this frequency range depends on the sampling rate, the spatial averaging of the ambient sound field and time averaging of the ambient sound ensembles.

The three wind-speed-from-ambient-sound equations can be arranged in order of decreasing $\sigma(U_e)$ (or increasing accuracy): Vagle's equation, Evans' equation, Equation 4.5. The mean $\sigma(U_e)$ for frequencies from 1 to 10 kHz and each data set are approximately 3, 2.3 and 1.8 $m\,s^{-1}$ for Vagle's equation, Evans' equation and Equation 4.5.

In general, Equation 4.5 shows half the $\sigma(U_e)$ that Vagle's equation does, while Evans' equation is approximately midway between the two. The three data sets can be arranged in order of decreasing mean $\sigma(U_e)$ (or increasing accuracy): 1996-10, 1997, 1996-60. The mean $\sigma(U_e)$ of Equation 4.5 for each data set for frequencies from 1 to 10 kHz is on order of 2.1, 2.0, 1.5 $m\,s^{-1}$ for the 1996-10, 1997, and 1996-60 data sets. These values represent the accuracy with which the wind speed can be determined for the sampling rates and spatial averaging of each data set.

Spectral averaging reduces the $\sigma(U_e)$ for the wind speed estimates from each

of the equations. The variance in the error is reduced the most for Vagle's equation, and shows a frequency dependence for this reduction. Spectral averaging does not improve the estimate from SSL_{10} as much as it does the SSL_1. This result is consistent with the amount of uncertainty in SSL recorded by the hydrophone (see Figure 4.5). The reduction in the estimate variance using Evans' equation is similar to Vagle's. Averaging of the wind speed estimates using Equation 4.5 results in approximately constant variance reduction. Only the 1997 data are improved by the spectral averaging, where the $\sigma(U_e)$ is reduced by approximately 0.4 $m\,s^{-1}$.

Time averaging is more effective than is spectral averaging in reducing the $\sigma(U_e)$. The $\sigma(U_e)$ is 0.8 $m\,s^{-1}$ less for estimates from Equation 4.5 using the data from 1996-60 than when the data from 1996-10 is used. Averaging 17 ensembles reduces the variance in the error more than when 64 frequency bins are averaged together.

The $\mu(U_e)$ is removed by adjusting Equation 4.5 by a correction factor, resulting in a wind speed-from-ambient-sound-equation of the form of Equation 4.19. Wind speed estimates using this equation result in μ and $\sigma(U_e)$ values listed in Table 4.7.

Deployment	1996-10		1996-40		1997	
Equation	$\sigma(U_e)$	$\mu(U_e)$	$\sigma(U_e)$	$\mu(U_e)$	$\sigma(U_e)$	$\mu(U_e)$
Eqn. 4.5	2.0 $m\,s^{-1}$	-0.0 $m\,s^{-1}$	1.3 $m\,s^{-1}$	-0.3 $m\,s^{-1}$	1.6 $m\,s^{-1}$	0.1 $m\,s^{-1}$

Table 4.7: The $\mu(U_e)$ and $\sigma(U_e)$ when the $SSL_{\overline{1-10}}$ is used in Equations 4.3 and 4.4, and the mean wind speed estimate using SSL_1 to SSL_{10} from Equation 4.5. Results for 1996-10, 1996-60 and 1997 are listed.

These results show that the wind speed can be estimated to an accuracy of: 2.0 $m\,s^{-1}$ when the data is collected every 70 seconds and averaged into 10 minute

108

ensembles, with the hydrophone at a depth of 250 m; 1.6 $m\ s^{-1}$ when the data is collected every 24 minutes and averaged into 72 minute ensembles, with the hydrophone at a depth of 100 m; 1.3 $m\ s^{-1}$ when the data is collected every 70 seconds and averaged into 60 minute ensembles, with the hydrophone at a depth of 250 m.

These results are not expected. The ambient sound was collected less frequently, had less spatial averaging and fewer ensemble averages in 1997 than in 1996-10, yet the variance in the error in the wind speed estimate was less in 1997 than in 1996-10. This may reflect a time scale limit of between 10 and 60 minutes for which the ambient sound levels adjust with the wind speed.

Estimates of wind speed using frequencies between 10 and 35 kHz still provide reasonable wind speed estimates (see Figure 4.4). It has been shown however, that at these frequencies there is a maximum wind speed which can be measured. As a result, quoting a μ and $\sigma(U_s)$ for results where the distribution of wind speeds includes values greater than 10 $m\ s^{-1}$ is not representative of the estimate accuracy at these frequencies.

The scatter plot of SSL versus SSL_s has an inflection point. This inflection point marks that wind speed at which there is a decline in SSL with increasing wind speed. This wind speed is 10 $m\ s^{-1}$ for frequencies greater than 20 kHz, and follows Equation 2.64 for frequencies from 8 to 15 kHz. This maximum wind speed means that the wind-speed-from-ambient-sound equation is bi-valued.

A consequence of the critical wind speed is that the spectral slope of the ambient sound spectrum is frequency dependent over the range of 1 to 72 kHz. The spectrum is divided into three Regions based on the relation of spectral slope and wind speed. Region I (1 to 10 kHz) has a constant spectral slope of approximately

109

-18 dB/decade. This slope varies by 4 dB/decade over a wind speed range of 0 to 20 $m\,s^{-1}$. Region II (10 to 35 kHz) has two wind speed ranges. For wind speeds less than 10 $m\,s^{-1}$ the spectral slope is approximately -17 dB/decade and varies by 4 dB/decade over 0 to 10 $m\,s^{-1}$. For wind speeds greater than 10 $m\,s^{-1}$ the spectral slope dramatically decreases changing by 15 dB/decade from 10 to 20 $m\,s^{-1}$. Region III (35 to 72 kHz) is unlike either Region I or II. The spectral slope decreases by 30 dB/decade over wind speeds from 0 to 8 $m\,s^{-1}$. Between 8 and 13 $m\,s^{-1}$ the spectral slope of this region is approximately constant at -20 dB/decade, and then increases as the wind speed increases.

The results presented here support the sound model used in Chapter 3 to set the SSL to a reference level independent of location and hydrophone depth. First, the fact that there is no frequency dependent mean error in the wind speed estimate for frequencies between 1 and 10 kHz. Second, the critical wind speed is identical when determined using the 1996-60 and 1997 data. Finally, the spectral behaviour with wind speed determined using each of the three data sets is identical.

110

Chapter 5

Rain Detection

5.1 Introduction

A characteristic sound is generated when drops of water strike the ocean surface. It is through this characteristic sound that precipitation can be identified and the rainfall rate estimated. Early studies determined that this sound was generated by the initial impact of the drop on the surface and the subsequent erratic entrainment of bubbles. It was also thought that sound levels were proportional to the raindrop diameter and the impact velocity of the drop (Franz 1959). Experiments have confirmed that the sound levels are proportional to drop size and impact velocity and are dependent on the entrainment of bubbles (Medwin et al. 1992; Oğuz and Prosperetti 1992; Pumphrey et al. 1989). While controlled experiments have expanded from the study of single falling drops to a spectrum of drops simulating rainfall, current field studies of ambient sound generated by rainfall over the ocean have been limited in duration, bandwidth of recorded sound, location, or have been laboratory controlled precipitation measurements (Scrimger et al. 1987; Nystuen and Selsor 1997). Of these previous works, Scrimger et al.'s (1987) study includes the largest frequency range, extending from 100 Hz to 50 kHz but is unfortunately limited to a wind speed

range of 1 to 5 $m\,s^{-1}$. Despite the existing description of the ambient sound spectra generated by falling drops and further work describing the effects of wind speed on the ambient spectra (Nystuen 1986), quantification of the sampling rate necessary to identify precipitation is still required. In addition, it is still unclear how accurate precipitation identification would be given continuous sampling for varying rainfall rates.

The present data set is unique in the duration, frequency range, and wind speeds of observations. For both the 1996 and 1997 deployment, meteorological activity was recorded visually at OWS Mike following World Meteorological Organization (WMO) protocol. In 1997, automated precipitation observations were available from an Optical Rain Gauge (ORG). The ORG determines the rainfall rate by observing the scintillations caused by drops passing through its LASER beam. This LASER beam is emitted at one end of the ORGs sampling area and observed by the ORG at the other. Rain drops passing through the beam block or alter the intensity of the LASER before it reaches the receiver, by a process similar to the light from stars passing through the atmosphere. These scintillations are characteristic of specific rainfall rates.

To begin this chapter, the WMO precipitation records from 1997 are compared to the ORG data. For this comparison to be valid, it must first be determined if the two reference records are dependent. This hypothesis is tested using a 2x2 contingency table and a χ^2 hypothesis test (see Appendix C).

The WMO data is also reclassified into eight sub-categories describing the type of precipitation which occurred in the observation hour. The new classification makes statistical comparisons of successful acoustic identification possible. Both the

112

WMO system and the new classification system (WMO sub-categories) are presented in Appendix D. Comparisons are then made between the hourly averaged ORG observations and the WMO sub-categories, as well as to the acoustic identifications.

Finally two precipitation-identification-from-ambient-sound algorithms (PIAs) are compared. One algorithm identifies the characteristic peak between 10 and 20 kHz (Lemon et al. 1984; Nystuen 1986), which shall be called the Nystuen Algorithm (NA). The other is developed in this chapter and makes use of the slope of the high frequency side of the peak reported by Scrimger et al. (1987) and is called the Slope Algorithm (SA).

The performance of both algorithms is compared to the WMO observations, because this data is available for both data sets. Where possible, quantification of rainfall rates and minutes of rainfall over the interval are presented using the ORG data. The effectiveness of both algorithms will be explored for various sampling intervals, precipitation types and wind conditions.

5.2 Effects of Sampling Rates

Data acquisition parameters were different between the 1996 and 1997 deployments. In 1996 the hydrophone was set to sample for 100 ms three times every 3.5 minutes, while in 1997 the hydrophone was set to sample for 100 ms three times every 72 minutes. This difference is significant considering the time scale for changes in precipitation. If there is no precipitation during one of the three 100 ms samples, then no precipitation can be detected. For a precipitation event that is not continuous over the ensemble length, there is a finite chance of not detecting the precipitation. The probability of detecting intermittent precipitation when the interval is sampled

only once is given by

$$p = \frac{i}{N}, \tag{5.1}$$

where i is the number of minutes of precipitation in N minutes. The probability changes when the interval is sampled more than once: for m samples the probability of detecting intermittent precipitation is given by

$$p(m) = 1 - \left(\frac{(N-m)!}{(N-m-i)!} \frac{(N-i)!}{N!} \right). \tag{5.2}$$

More specifically, Equation 5.2 is the probability of detecting at least one minute of rain out of N minutes of recorded ambient sound, and is determined by simplifying the appropriate hypergeometric distribution.

The sampling time also affects how the ambient sound data will be compared to the meteorological data. The WMO data is recorded every hour and reflective of the events in the past hour, while the ORG data is recorded every minute. For the 1996 ambient sound data, the 3.5 minute ensembles can be averaged into one hour ensembles and compared to the WMO data. The disadvantage of this approach is that it averages out isolated precipitation signals occurring in one of the averaged ensembles and may result in a missed identification of precipitation for that hour (referred to as a loss in Sensitivity, see §5.4.3). For future reference this processing will be referred to as the 1996-60 data set (as defined in Chapter 3).

Since 10 minute wind speed data exists for 1996, the 3.5 minute ambient sound data has been averaged into 10 minute intervals for comparison to the anemometer data. The ambient sound spectra from this shorter averaging interval will also be compared to the WMO precipitation observations to examine the effects that averaging has on the acoustic signal dominated by precipitation. This approach will be

114

referred to as the 1996-10 data set.

For the 1997 data set, ambient sound was sampled 3 times every 72 minutes and averaged to give the recorded ensemble. As a result, the 72 minute ensemble is composed of 2 spectra from one hour, and another from an adjacent hour. Ambient sound identifications are compared to WMO observations corresponding to the hour in which two of the three ambient sound spectra in the ensemble occur. For the times when the ambient sound recording is exactly in between two WMO readings, the data are ignored.

Comparisons to the ORG data are straightforward because the ORG recorded rainfall rates every minute. From these rainfall rates the mean rainfall rate for any longer interval can be calculated. An interval will be considered to have contained precipitation, as determined by the ORG, if any one minute in that interval contained a rainfall rate greater than or equal to 0.1 $mm\,hr^{-1}$(the minimum resolution of the ORG).

5.3 The Different Precipitation Records

Recorded every minute, the ORG rainfall data represent the most comprehensive reference for comparison with the ambient sound spectra. A comparison between the WMO and ORG data is presented to allow a consistent comparison between 1997 data (with both WMO and ORG observations) and the 1996 data where the ambient sound data was sampled more frequently, but for which no ORG data is available.

5.3.1 Statistical Comparison

Do these two standard methods of identifying periods of precipitation differ statistically? To answer this question, the precipitation data from the ORG data and WMO observations are summarized in a 2x2 contingency table (Table 5.1). The

	ORG	
	Precipitation	No Precipitation
WMO	Precipitation	632	388
	No Precipitation	130	1016

Table 5.1: Contingency table for ORG record of precipitation to the WMO record of precipitation.

Precipitation column under the *ORG* heading identifies the elements in the data for which the ORG indicated precipitation. The rows divide the *ORG Precipitation* data into elements when the WMO observations simultaneously indicated precipitation. and those when the WMO observations did not indicate precipitation. The *No Precipitation* column divides the elements of the data when the ORG data did not indicate precipitation, and when the WMO observation distinguishes elements as precipitation and no precipitation. The ORG data and the WMO data provide meteorological information for 2166 hours, during which ambient sound was recorded for 1129 hours. Over these 2166 hours, the two instruments simultaneously indicated there had been precipitation during 632 hours and no precipitation during 1016 hours. One instrument indicated precipitation while the other did not during 518 hours. To test whether these two methods of reporting precipitation are statistically dependent, the null hypothesis that the results from the ORG are independent of the results from the WMO is assumed. Using a χ^2 test (see Appendix C) for the

116

values in Table 5.1 results in $\chi^2 = 622.6$. This value is greater than the rejection criteria using a 95% confidence of $\chi^2 = 3.84$, so the null hypothesis is rejected. The two standards are statistically dependent.

In order to quantify this dependence, a comparison parameter is defined by

$$\frac{m_r}{r} \tag{5.3}$$

where m_r is the number of times both the WMO record and the ORG data simultaneously indicate precipitation, and r is the number of precipitation events the WMO observations or the ORG data indicate in total. For the WMO observations $\frac{m_r}{r}$ is 62%, and for the ORG data $\frac{m_r}{r}$ is 83%.

It is also useful to consider how often the two methods agree on the presence and absence of precipitation. Consider

$$\frac{m_r + m_{nr}}{N} \tag{5.4}$$

where m_{nr} is the number of times the two records simultaneously indicated there was no precipitation, and N is the total number of samples in the data set. Using this comparison, of the 2166 intervals examined, these two methods of reporting precipitation match 76% of the time.

The difference in comparison percentages is a consequence of the fact that there are more non-precipitation events in the observations than precipitation events. This weighting gives a larger number of matches when considering non precipitation events. A contributing factor that limits agreement to a 76% match is the sampling area difference between the two methods of reporting precipitation. And, the sampling area of the hydrophone is different than the sampling radius of both the WMO visual record and the ORG measurements. The hydrophone samples an area at the

117

surface approximated by a circle of radius equal to the depth of the hydrophone, whereas the WMO entries are limited by the distance to the visual horizon, and the ORG measures a 504 X 76 mm^2 area. Although the ORG measures rainfall at what is effectively one point in space, it averages data over a longer interval. Precipitation is expected to occur on length scales of approximately hundreds of meters so, like the anemometer, and long time intervals, the ORG represents precipitation measurements over a spatial scale larger than the listening radius of the hydrophone (see Appendix F). The WMO sampling area is also much larger than the hydrophone's listening area, so in reality the ambient sound data is correlated to something on a spatial scale smaller than either the WMO observations or the ORG observations. Given the less than 100% agreement between the ORG and the WMO observations the probability of detecting precipitation acoustically cannot be better than the agreement between the WMO and the ORG, that is 76%.

5.3.2 A Simplified WMO Precipitation Classification System

The WMO weather observation standard consists of 100 different entries corresponding to the current meteorological conditions, including conditions as common as fog and as exotic as sand storms. Many of the entries are similar in nature but are distinct depending on specific details. For example, whether the entry had occurred in the past hour or at the time of observation. Based on these similarities, the entries have been reclassified into eight sub-categories as follows: no precipitation of any type present (0); 'Intermittent Drizzle' (1); 'Continuous Drizzle' (2); 'Intermittent Rain' (3); 'Continuous Rain' (4); 'Showers' (5); 'Solid Precipitation' (hail, snow, freezing rain etc.)(6); and 'Unclassified' (9). The unclassified sub-category contains

elements which do not fall into the six main precipitation categories (1-6). The actual WMO descriptions and the sub-categories in which they are reorganized are included in Appendix D.

In order to give quantitative parameters to the qualitative WMO sub-categories, the mean rainfall rate and the duration of precipitation over the hour are given by the ORG data are shown for each WMO sub-category in Table 5.2.

Category	Size	Mean Rainfall Rate	Mean Minutes of Precipitation
Intermittent Drizzle	13 hours	$0.10 \ mm \ hr^{-1}$	15 minutes/hr
Continuous Drizzle	18 hours	$0.13 \ mm \ hr^{-1}$	17 minutes/hr
Intermittent Rain	37 hours	$0.36 \ mm \ hr^{-1}$	27 minutes/hr
Continuous Rain	147 hours	$0.55 \ mm \ hr^{-1}$	38 minutes/hr
Showers	94 hours	$1.47 \ mm \ hr^{-1}$	15 minutes/hr
Solid	186 hours	$1.66 \ mm \ hr^{-1}$	19 minutes/hr
Unclassified	137 hours	$0.37 \ mm \ hr^{-1}$	12 minutes/hr

Table 5.2: Rainfall rates and frequency of precipitation over hour intervals, corresponding to the WMO sub-categories for the 1997 data meteorological data.

The data from this table are also represented graphically by the histograms shown in Figure D.1 and Figure D.2. As an example of these histograms, the distribution of minutes of precipitation per hour for 'Intermittent' (a) and 'Continuous Rain' (b) are shown in Figure 5.1. Figure 5.1b shows that there is the highest probability of precipitation over the entire hour compared to any other duration for the 'Continuous Rain' sub-category, as noted by the approximately 1:9 ratio of any duration to the 60 minute duration. This ratio is between 1:5 and 3:5 for 'Intermittent Rain' and distinguishes the intermittent category from the continuous category (Figure 5.1a). From Table 5.2, there is a larger mean rainfall rate for the 'Rain' categories than for the 'Drizzle' categories and a larger mean number of minutes of precipitation observed during intervals identified as 'Continuous' rather than 'Intermittent'

119
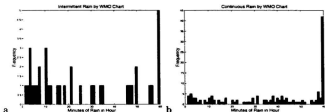
Figure 5.1: Histogram of minutes of rain for WMO sub-categories a) 'Intermittent Rain' and b) 'Continuous Rain.'

precipitation. The 'Shower' category describes precipitation events that have measurable rainfall during 15 minutes of every hour, and correspond to a rainfall rate of $1.47 \ mm \ hr^{-1}$.

The 'Unclassified' precipitation describes intermittent precipitation with a rainfall rate of $0.37 \ mm \ hr^{-1}$. This rainfall rate is identical to that for 'Intermittent Rain,' but the minutes of rain during an hour are less than those for 'Intermittent Drizzle.' For classifying the performance of the identification algorithms, this category will be treated as an intermittent category.

'Solid' precipitation generates a distinct acoustic signal from wind-only or liquid precipitation events (Scrimger et al. 1987). It is unclear if the rate of precipitation for this category has an effect on the chance of detection, and is only included for a cursory comparison.

5.3.3 Precipitation Distribution for 1996 and 1997

To illustrate the different precipitation patterns between the two deployments, Figure 5.2 shows the breakdown of precipitation events by WMO sub-category for the two deployments.
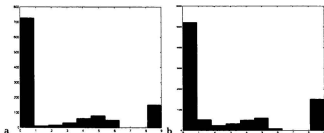
Figure 5.2: Histogram of the number of occurrences in each WMO sub-category, for the a) 1997 deployment and b) 1996 hourly deployment. The categories are: 0. 'No Precipitation'; 1. 'Intermittent Drizzle'; 2. 'Continuous Drizzle'; 3. 'Intermittent Rain'; 4. 'Continuous Rain'; 5. 'Showers'; 6. 'Solid Precipitation'; 9. 'Unclassified'.

The main distinction between deployments is the frequent occurrence of 'Intermittent Drizzle' (category 1) in 1996 (Figure 5.2b)compared to 1997(Figure 5.2a). These frequencies are quantified later in Table 5.9

Equation 5.2 gives the probability of detecting intermittent precipitation if the sound levels are sampled n times over a sample interval. From the ORG data, the number of minutes of rain in each of the 72 minute intervals is available. Using this distribution of precipitation, the probability of detecting precipitation can be determined for the specific temporal distribution of precipitation in 1997. The overall probability for detecting precipitation can be calculated from the sum of the

121

probabilities of detecting an interval with i minutes of precipitation, sampled for m minutes over that interval. By modifying Equation 5.2 to include the number of intervals with i minutes of precipitation the probability of detecting intermittent precipitation as a function of the number of samples taken is given by

$$p(m) = 1 - \left(\frac{(N-m)!}{(N-m-i)!} \frac{(N-i)!}{N!} \right) \frac{H(i)}{\sum H}. \tag{5.5}$$

where $H(i)$ is the number of observations with i minutes of rain and $N = 72$ is the length of the interval. The resulting probability as a function of samples per interval is plotted in Figure 5.3. Sampling the 1997 data set three times in a 72 minute
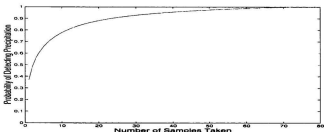
Figure 5.3: The probability of detecting precipitation as a function of number of samples over a 72 minute interval given the 1997 precipitation distribution.

interval yields a 56% chance of detecting precipitation, while sampling 17 times per 72 minute interval yields an 86% chance of detecting precipitation.

Although the distribution for the 1996 data set is unknown, a similar probability distribution can be obtained. Figure 5.2 shows that there is more 'Continuous' and 'Intermittent Drizzle' in the 1996 (b) WMO observations than in 1997 (a) WMO observations. The distribution of WMO sub-categories from Figure 5.2b and

122

the minutes of precipitation for each WMO sub-category from Table 5.2 define the distribution of minutes of precipitation for 1996 as

$$H(i) = WMO(j) \tag{5.6}$$

$$i = \{15, 17, 27, 38, 15, 19, 12\} \tag{5.7}$$

$$j = \{1, 2, 3, 4, 5, 6, 9\}. \tag{5.8}$$

j is the set of WMO sub-categories indicating precipitation, $WMO(j)$ is the number of observations in sub-category j and i is the number of minutes of rain for that sub-category from Table 5.2. $H(i)$ is then used in Equation 5.5 with $N = 60$. For the ambient sound spectra from 1996-60, the probability of detecting precipitation over the 60 minute interval is 99% when that interval is sampled 17 times.

The probabilities for detecting precipitation must be adjusted to the fact that the ORG and WMO observations agreed 76% of the time. The total probability of detecting precipitation is then a combination of the probability from Equation 5.5 and the percent agreement between the ORG data and the WMO observations (i.e., 76%). This is given by

$$P(m) = 0.76 \cdot p(m) \tag{5.9}$$

where $p(m)$ is given by Equation 5.5. For 1996-60 the modified chance of detecting precipitation is 75% and for 1997 is 43%.

5.4 Precipitation Identification Algorithms (PIAs)

A sample precipitation spectrum is shown in Figure 5.4. In this figure the constant wind-only slope of -19 dB/decade has been removed to reduce the dynamic range

123

of the spectrum. Noise in the spectrum is seen as various 2 dB peaks in the red dashed line. The blue solid line shows the spectrum after a moving average filter of
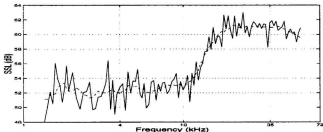
Figure 5.4: Individual spectrum from 1997 data set. The red dashed line is the raw spectra and the blue solid line is the smoothed spectrum. The wind speed corresponding to the ensemble was 5.1 $m\,s^{-1}$.

length 9 frequency bins has been applied; this processing will be discussed later. The spectrum (raw or smoothed) shows two distinct features of ambient sound generated by precipitation: i) the broad peak in SSL between 10 and 25 kHz; ii) the spectral slope in Region III (from 35 to 72 kHz) which is less than -19 dB/decade.

The following section describes two algorithms, each of which use one of these two features to identify precipitation from the ambient sound spectra of the present data.

5.4.1 The Algorithms

5.4.1.1 The Modified Nystuen Algorithm

The Nystuen Algorithm (NA) identifies precipitation by the increased sound level at 20 kHz relative to the sound level at 8 kHz. Smoothed spectra are used for the

NA because false identifications occur when noise in the spectra cause an anomalous increase in the SSL at 20 kHz or a decrease in SSL at 8 kHz. To increase the separation of SSL_{20} and SSL_8 for precipitation events, the sharp noise peaks in the spectra are removed by means of a smoothing algorithm. For points away from the end of the spectra, an average value was computed using a moving average of variable length. The distance in frequency bins from 8 to 20 kHz is 30 bins. The moving average should be designed to filter variations in the signal that are shorter than half this size. Experience suggests an optimal moving average length for smoothing is 9 bins for the present data. A sample spectrum which has been smoothed by this moving average is shown as the red solid line in Figure 5.4

The NA works by fitting two test lines to a scatter plot of the SSL_{20} versus the SSL_8 from the smoothed spectra. For wind-only spectra these points should fit a straight line, with a slope of 1 and an intercept governed by the -19 dB/decade slope of wind-only ambient sound. At high wind speeds (i.e., above 15 $m\,s^{-1}$) there is an inflection point in the scatter plot (Farmer and Lemon 1984), so that an increase in the wind speed, or increase in the SSL_8, causes a decrease in SSL_{20}. Test lines are used to separate wind-only events from precipitation events by applying the known spectral characteristics of ambient sound, specifically the linear relation of SSL to wind speed and the inflection point in the scatter plots of SSL at high wind speeds. Scatter plots of the smoothed spectra for the 1997, 1996-60 and 1996-10 data sets are shown in Figures 5.5a, b, and c with test lines indicated in green (the drizzle line), and red (the rain line).

Attempts were made to automate the process of selecting the rain and drizzle line using the estimated uncertainty in SSL_{20} and SSL_8. However optimal perfor-

125

mance (see §5.4.3) was obtained identifying the end points of the test lines by visual inspection.

For this algorithm, the distinction between rain and drizzle comes from the difference in rain-drop size. Rain (or large drops) adds a significant amount of energy to the lower frequency SSL and therefore raises the 8 kHz SSL relative to 20 kHz, thereby flattening the spectrum. Drizzle significantly raises the SSL at 20 kHz without affecting the signal at 8 kHz. Examples of drizzle and rain dominated ambient sound spectra are shown in Figure 2.6 from Chapter 2.

A third test line, called the 'apex line', can be included if necessary to separate the region that forms in the apex of the triangle subtended by the 'Drizzle' and 'Rain line' from wind-only SSL in the scatter plot. Physically, the apex line is the maximum SSL_{20} intensity for wind-only events and is shown as the horizontal red dashed line in the three scatter plots of SSL_{20} versus SSL_8. The apex line becomes necessary as scatter in the plot lengthens the radius of curvature at the inflection point creating a larger area in the triangle formed by the maximum SSL_{20}, the 'Rain Line' and the 'Drizzle Line.' The apex line is only needed in the 1996-10 data set.

Parameter	1997	1996-10	1996-60
D X1,Y1	58,52.5	59.5,53.5	59.5,52
D X2,Y2	40,36	40,35.5	40,35.5
R X1,Y1	58,52	59.5,53	59.5,52
R X2,Y2	65,46	65,49	65,46.5
High Seas	58	59.5	59.5
Max 20 kHz	52	51.5	51.5

Table 5.3: The SSL in dB for the end points of the test lines used by the NA for the 1997, 1996-60 and 1996-10 data sets.

Test line parameters for 1996-10, 1996-60 and 1997 are shown in Table 5.3. For

126
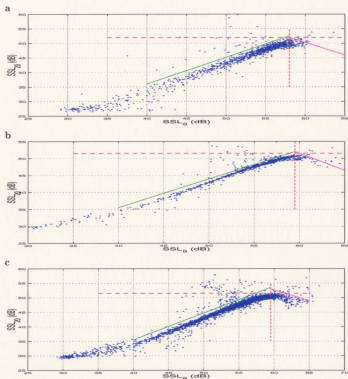
Figure 5.5: Scatter plot of the SSL_{20} versus SSL_8 for a) 1997, b) 1996-60, and c) 1996-10 data sets. The precipitation identification lines are shown: high seas inflection point (vertical red dashed line); maximum SSL_{20} or 'apex line' (horizontal dashed line); 'drizzle line' (green solid line to the left of high seas); and 'rain line' (red solid line to the right of high seas).

each data set, the test line end points as well as the maximum wind-only SSL_{20} and the SSL_8 at the inflection point are similar in value. All x-coordinates (DX1, DX2, RX1, RX2 and High Seas) have an uncertainty equal to the uncertainty in SSL_8. The y-coordinates (DY1, DY2, RY1, RY2 and Max 20 kHz) have an uncertainty equal to the uncertainty in SSL_{20}. The uncertainty in the SSL_8 for the 1996-10, 1996-60, and 1997 data sets are $\pm$ 0.49, 0.43, 0.62 dB respectively. Comparing the 1996-60 test line points to the 1997 test line points, within the experimental uncertainty only $DX2$ and $RX1$ values are identical. The uncertainty in the SSL_{20} for the 1996-10, 1996-60, and 1997 data sets are $\pm$ 0.32, 0.28 and 0.40 dB. Within the experimental uncertainty, only the DY2 and Max 20 kHz points are identical. That these test lines cannot be set by shifting them by a common value proportional to the expected uncertainty means that a simple automated scheme which maximizes precipitation identification is not possible with this approach. It is, however, encouraging that all the values are identical within twice the uncertainty in both coordinates (95% confidence).

While the argument can be made that identifying the test lines by slope and intercept would make comparison between deployment examples more clear, identifying the test lines by physically significant sound levels serves two purposes: i), choosing physically significant intensities of sound at specific frequencies allows for easy identification of the meteorological events which cause the characteristic intensity features; ii), choosing the end points is easier to do from the scatter plots.

Averaged spectra of correct (solid blue line) and incorrect (red dot dashed line) precipitation identifications made by the NA are shown in Figure 5.6. These two spectra are not visibly different; there is a pronounced peak between 10 and

128

20 kHz in both spectra. The mean sound spectra for precipitation not identified by the NA (green dashed line) has a constant spectral slope and therefore reflects wind-only conditions. The similarity of the missed identifications to the wind-only spectra indicates that this algorithm cannot identify all precipitation, although the exact cause is not clear from this data. The similarity of correct and incorrect identifications indicates one of three possibilities: 1) there is a time dependent decay of the precipitation generated sound so that the NA identifies precipitation when the WMO does not; 2) this technique is sensitive to spray and splashing which might lead to false identification; 3) precipitation sound is entering the listening radius from outside the sampling area of the WMO.

The ambient sound spectra for correct identifications made by the NA but classified as drizzle (solid blue line) and rain (red dashed dot line) do differ (Figure 5.7). In this comparison, the wind-only ambient sound spectra (dashed black line) includes only wind speeds greater than $12\ m\ s^{-1}$ in order to illustrate the difference of the rain sound spectra. This difference is that both have similar SSLs at 8 kHz, but the rain spectra has elevated SSL at 20 kHz compared to the wind-only sound spectra. For rain generated ambient sound there is no attenuation in the SSL during wind speeds greater than $12\ m\ s^{-1}$ for frequencies from 10 to 35 kHz as noted by Farmer and Lemon (1984). The high wind speed threshold was chosen as $12\ m\ s^{-1}$ and not $10\ m\ s^{-1}$ because this choice more clearly demonstrates the distinction between the rain and wind-only sound spectra.
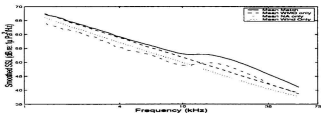
Figure 5.6: The mean smoothed ambient sound spectra for successful precipitation identifications by the NA (solid blue line), unidentified precipitation by the NA (dashed green line), incorrect identifications made by the NA (red dot dashed line) and wind-only spectra (dotted black line) from the 1997 data set.

Figure 5.7: The mean smoothed ambient sound spectra for drizzle identifications made by the NA (solid blue line), rain identifications made by the NA (red dot dashed line) and wind-only spectra for wind speeds greater than $12\ m\,s^{-1}$ (dotted black line) from the 1997 data set.

5.4.1.2 The Slope Algorithm (the SA)

The SA uses the distinct spectral slope from 35 to 72 kHz (Region III) to distinguish wind-only conditions from those with precipitation. Although the spectral slope over this frequency changes with wind speed (see §4.4.4), it is still possible to distinguish the slope from spectra generated by the wind-only mechanism from those that were recorded during precipitation. Figures 5.8a b, and c show the scatter plots of the $SSL_{\overline{1-10}}$ versus the spectral slope from 35 to 72 kHz for the 1997 and 1996 data.

Three lines are used to distinguish wind-only ambient sound from that dominated by precipitation. The first line is the 'Apex Line', which is the horizontal line corresponding to the minimum value for wind-only slopes in Region III. The other two lines are entered by choosing feet end points, and are distinguished in the same manner as the 'Rain' and 'Drizzle' lines are for the NA: by the inflection point in the spectrum identified by Farmer and Lemon (1984). To distinguish the 'Rain' and 'Drizzle' lines between algorithms, the algorithm name for which the line is used shall accompany the line name (i.e., 'Nystuen's Rain line,' or the 'Slope Rain line'). The end point method for the test lines is used for reasons identified when describing the NA.

The parameters used to choose these test lines for the 1997 and 1996 ambient sound data are given in Table 5.4 and do not show continuity between data sets. The uncertainty in the y-coordinates is given by the uncertainties in the spectral slope from 35 to 72 kHz for the 1996-10, 1996-60 and 1997 ambient sound spectra which are $\pm$ 1.45, 1.19 and 1.80 dB/decade, respectively. The uncertainty in the x-coordinate is given by the uncertainty in the SSL_6 for the 1996-10, 1996-60, and 1997 data sets which are $\pm$ 0.49, 0.43, 0.62 dB respectively. The values of $DY1$, $DX2$, $RY1$ and

131
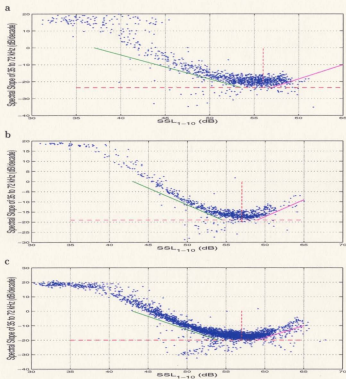
Figure 5.8: Scatter plot of the slope of Region III kHz versus SSL_{1-10} for the a) 1997, b) 1996-60, and c) 1996-10 data sets. The precipitation identification lines are shown: high seas roll over (vertical red dashed line); minimum spectral slope or 'apex line' (horizontal dashed line); 'drizzle line' (green solid line to the left of high seas); and 'rain line' (red solid line to the right of high seas).

Parameter	1997	1996-10	1996-60
D X1,Y1	53.5,-23.5	54,-20	54.5,-19
D X2,Y2	37,0	43,0	43,0
R X1,Y1	57,-23.5	59,-20	59,-19
R X2,Y2	65,-10	65,-10	65,-9
High Seas in dB	56	57	57
Min S, in dB/dec	-23.5	-20	-19

Table 5.4: The SSL in dB for the end points of the test lines used by the SA for the 1997, 1996-60 and 1996-10 data sets.

$R Y2$ are not within the expected uncertainty in SSL when the test line end points for 1996-60 and 1997 are compared. However, there is consistency for the $D Y1$ and $R Y1$: they are always equal to the 'Minimum Slope' coordinate. The high seas inflection point is identical within uncertainty for all deployment examples. In this algorithm there is no simple scheme to select the test lines in order to maximize the precipitation identification using the expected uncertainty for the scatter plot.

Averaged ambient sound spectra for correct (solid blue line) and incorrect (red dashed dot line) precipitation identifications made by the SA are shown in Figure 5.9. These two spectra are visibly different: the spectral slope of correct identifications is steeper than those for incorrect identifications. The mean sound spectra for precipitation not identified by the NA (green dashed line) resembles the mean wind-only ambient sound spectra (black dashed line). The similarity of the wind-only spectra and the missed precipitation identifications indicates that all precipitation cannot be identified by this algorithm, although the cause of the limitation is not identifiable from this data. The similarity of the correct and incorrect identifications indicates one of three possibilities: 1) there is a time dependent decay of the precipitation generated sound so that the NA identifies precipitation when the WMO does

133

not; 2) this technique is sensitive to spray and splashing which might lead to false identification; 3) precipitation sound is entering the listening radius from outside the sampling area of the WMO.

The ambient sound spectra for correct identifications made by the SA but classified as drizzle (solid blue line) and rain (green dashed line) do differ (Figure 5.10) but not in spectral slope from 35 to 72 kHz. The sound spectra of rain and sound spectra classified as 'apex' events (red dashed dot) are similar. In this comparison, the wind-only ambient sound spectra (dashed black line) includes only wind speeds greater than 12 $m\,s^{-1}$ in order to illustrate the difference of the drizzle, rain and 'apex' sound spectra from the wind-only sound spectra. For all types of precipitation (i.e., rain, drizzle and 'apex') generated ambient sound there is a distinct spectral slope from 35 to 72 kHz. The high wind speed threshold was chosen as 12 $m\,s^{-1}$ and not 10 $m\,s^{-1}$ because this choice more clearly demonstrates the distinction between the rain and apex sound spectra and the wind-only sound spectra.
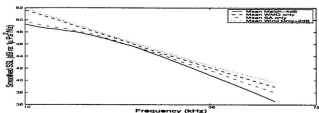
Figure 5.9: The mean smoothed ambient sound spectra for successful precipitation identifications by the SA (solid blue line), unidentified precipitation by the SA (dashed green line), incorrect identifications made by the SA (red dot dashed line) and wind-only spectra (dotted black line) from the 1997 data set.
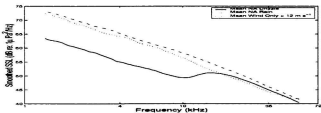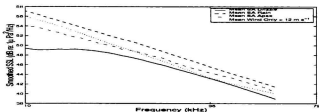

Figure 5.10: The mean smoothed ambient sound spectra for drizzle identifications made by the SA (solid blue line), rain identifications made by the SA (green dashed line), the 'apex' identifications made by the SA (red dot dashed line) and wind-only spectra for wind speeds greater than $12\ m\ s^{-1}$ (dotted black line) from the 1997 data set.

5.4.2 PIAs Based on other Spectral Slopes

The location and nature of peak in the rain sound spectrum suggests that the spectral slope from 10 to 20 kHz could be used to identify periods of precipitation. However, calculating the slope over this region does not provide a better indicator of precipitation compared to the NA. The NA already intrinsically compares this property. Explicit calculation of the slope in this range is complicated by the drop size dependent SSL peak in this frequency range, and the limited number of bins in this frequency range. In contrast, there is no single frequency above 35 kHz which can be compared to the SSL at 8 kHz in order to identify precipitation. Further, the limited frequency bins in the 35 to 72 kHz region is countered with more degrees of freedom per bin and consequently less uncertainty. In addition, there is no inflection point in the sound spectrum except when low signal levels are obscured by the electrical noise minimum at low wind speed conditions.

The spectral slope from 1 to 10 kHz is insensitive to acoustic precipitation signals.

5.4.3 Comparison Parameters for PIAs

The two precipitation identification algorithms will be rated for efficiency by defining two parameters: the Sensitivity (S) and the Confidence (C). The Confidence represents how often the indication of precipitation from the algorithms coincides with an observation of precipitation from the reference. Either the WMO observations or the ORG data could be used but for continuity, only the WMO data will be used since it is available for all data sets. The Sensitivity is a measure of how many precipitation events, as identified by the WMO observations, are correctly identified

by the algorithm. These parameters are defined as:

$$C = \frac{m_r}{n_a} \tag{5.10}$$

and

$$S = \frac{m_r}{s_r} \tag{5.11}$$

where s_r is the number of WMO observations which indicate precipitation, n_a is the number of ambient sound spectra the algorithm flags as precipitation, and m_r is the number of flagged ambient sound spectra which correspond to WMO observations of precipitation.

The Confidence and Sensitivity quantify two aspects of precipitation identification. An understanding of these indicators can be gained by considering a binomial distribution of precipitation and a randomly selected sample flagged as precipitation. For a probability of precipitation, p, given by

$$p = \frac{r}{N}, \tag{5.12}$$

where r is the number of precipitation events as indicated by the reference and N is the total number of time intervals being considered. The mean number of random samples correctly flagged as precipitation is given by

$$\mu_r = n_a p \tag{5.13}$$

and has a standard deviation of

$$\sigma = \sqrt{n_a p q}. \tag{5.14}$$

q is the probability of no precipitation, and is given by

$$q = 1 - p. \tag{5.15}$$

137

A randomly chosen sample would contain no more than

$$\mu_r + 1.96 \cdot \sigma \tag{5.16}$$

precipitation events (with a 95% confidence).

From these considerations, two new parameters can be defined to quantify how much better the algorithms perform compared to randomly selected samples. The first parameter is the *standard normalized random variable*, z, which is given by

$$z = \frac{m_r - \mu}{\sigma}. \tag{5.17}$$

z represents the difference, as a ratio of standard deviation, of the statistical mean μ and the algorithm identifications m_r. The second parameter to quantify performance is the *standard random variable*, t, which is the ratio of the number of events correctly identified by the algorithm to the randomly selected mean and is given by

$$t = \frac{m_r}{\mu_r}. \tag{5.18}$$

If t were equal to one then the algorithm would have correctly selected the same number of precipitation events as would a randomly selected sample. From elementary statistics, for a normally distributed function 95% of the distribution lies within $1.96 \cdot \sigma$ of the mean. If $t \geq 1$ but $z < 1.96$, then it would be unclear if the PIA performed any better than the random sample with a 95% confidence. In order to accommodate this 95% confidence interval in a performance parameter, define

$$t_{95} = \frac{m_r}{\mu_r + 1.96 \cdot \sigma} \tag{5.19}$$

which is the ratio of events correctly identified by the algorithm to the maximum limit of the random sample with 95% confidence. This new definition of t provides

138

an unambiguous indication if the algorithms are selecting more precipitation events than a random sample from the time series of ambient sound spectra.

The uncertainty in both the Confidence and the Sensitivity are determined by integrating

$$P_i = \frac{n!}{i!(n-i)!} p^i \cdot q^{(n-i)} \tag{5.20}$$

and determining the point at which the integral is equal to 0.95, for 95% confidence. n is the number of identifications made by the algorithm for the Confidence, and is the number of WMO observations for the Sensitivity, i is the number of observations correctly identified by the algorithm. p is the ratio of correct identifications made to the total identifications for the Confidence, and is the ratio of correct identifications made to the total WMO observations for the Sensitivity. In all cases, $q = 1 - p$.

5.5 Observations

5.5.1 'Drizzle', and 'Rain' Distinction

Using the parameters described in Tables 5.3 and 5.4, the distinction between 'Drizzle' and 'Rain' for the two algorithms is quantified using the ORG data from 1997. For the SA, the mean rainfall rate for time intervals corresponding to ambient sound spectra identified as 'Rain' was 1.65 $mm\,hr^{-1}$, while those identified as 'Drizzle' had a mean rainfall rate of 0.29 $mm\,hr^{-1}$. These results are comparable with those obtained using the NA, where the mean rainfall rate of 'Rain' events is 1.64 $mm\,hr^{-1}$, and for 'Drizzle' events is 0.30 $mm\,hr^{-1}$.

Using the SA, the 'Apex' events do not clearly fall into either 'Drizzle' or 'Rain' categories. The events identified as 'Apex' using the SA have a mean rainfall rate

of 0.42 $mm\,hr^{-1}$ which is greater than the 'Drizzle' events but less than the 'Rain' events. There are no points within the 'Apex' when the NA is used for the 1997 data.

5.5.2 Overall PIA Performance

The performance of either algorithm can be measured by its gross identification of precipitation (Sensitivity), its accurate identification of precipitation (Confidence), and its performance relative to a random sample within 95% confidence (t_{95}). Table 5.5 summarizes the performance parameters of both algorithms for the three deployment cases. In all cases the identifications from the algorithms are compared to the meteorological records from the WMO observations only.

Data Set	Algorithm	Confidence	Sensitivity	t_{95}
1996-10	SA	$64.0\% \pm 11.1\%$	$17.4\% \pm 2.1\%$	1.41
1996-10	NA	$69.6\% \pm 11.9\%$	$10.1\% \pm 1.6\%$	1.43
1996-60	SA	$83.3\% \pm 11.7\%$	$13.2\% \pm 1.6\%$	1.83
1996-60	NA	$78.3\% \pm 11.6\%$	$14.2\% \pm 1.8\%$	2.1
1997	SA	$76.8\% \pm 9.5\%$	$18.2\% \pm 2.0\%$	2.21
1997	NA	$86.3\% \pm 11.8\%$	$10.9\% \pm 1.3\%$	1.19

Table 5.5: Measure of success for the two PIAs for the 1996-10, 1996-60 and 1997 data sets. The uncertainty in each column was determined using Equation 5.20 with 95% confidence.

In all data sets, the algorithms perform better than a randomly selected sample, demonstrated by the t_{95} values in Table 5.5. A t_{95} value of 1 indicates that the algorithm identified as many precipitation events as would a randomly selected sample with 95% confidence. In all data sets both algorithms have $t_{95} > 1$, indicating that they both correctly identify more precipitation than would a randomly selected

140

sample of equal size.

The Sensitivity of either algorithm in all deployments is less than the predicted Sensitivity. Theoretically, the Sensitivity should approach the values given in §5.3.1 of 41% for 1997 and 74% for 1996-60. The values presented under *Sensitivity* in Table 5.5 show that, in the present data, the NA detects 30% less precipitation than predicted for 1997, while the SA detects 20% less. Both algorithms detect 60% less precipitation than predicted during 1996. This result indicates that certain meteorological conditions, such as rainfall rate or wind speed, may affect the probability of acoustically identifying precipitation.

5.5.2.1 Time Averaging

The effects of time averaging are explored by comparing the 1996-60 data set to the 1996-10 data. The Sensitivity of the SA improves from 13% to 17% while the Sensitivity of the NA drops from 14% to 10% when 3 ensembles are averaged, as in the 1996-10 data set, than when 17 ensembles are averaged, as in the 1996-60 data set. This result shows that removing the effects of averaging the ambient sound spectra does not make the Sensitivity approach the expected level from §5.3.1 of 74%. In addition, the Confidence of both algorithms drops: the NA sees a reduction in Confidence of 10% while the Confidence for the SA decreases by nearly 20%.

The limited improvement in Sensitivity and the drop in Confidence for the 1996-10 data set is expected. There is no precipitation record sampled at 10 minute intervals available for reliable comparison. As such, the 1996-10 data set will not be examined further.

5.5.2.2 Similarities in PIAs

To illustrate the results of the algorithms for the 1996-60 and 1997 data sets, Venn

diagrams show the intersection of the WMO observations and the identifications from the both algorithms in Figures 5.11a and b.
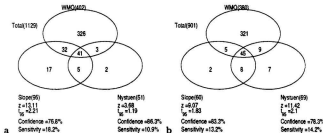
Figure 5.11: Venn diagram for the intersection of the sets (SA, NA, and WMO) for a) the 1997 data set and b) the 1996-60 data set. z, t_{98}, Confidence and Sensitivity are defined in §5.4.3.

The number located in the intersection of the three circles is the number of acoustic observations for which both algorithms detected precipitation when the WMO observation simultaneously indicated precipitation. Similarly, the number in the area of intersection of any two circles is the number of observations that fell into the two sets represented by the circles which intersect. For example, the number of observations for which both the SA and the NA identified precipitation, but the WMO observations did not, is 5 during 1997 (see Figure 5.11a).

Five of the incorrect identifications made by one algorithm overlap with the other in 1997, while eight incorrect identifications overlap in 1996. This overlap might indicate correlation to an event which affects both the algorithms. Further support to the correlation between the decrease in spectral slope and the increase in SSL_{20} relative to SSL_4 is the 41 element overlap in correct identifications made during 1997

142

and the 45 element overlap observed in 1996. In 1997 there are 32 additional correct SA identifications compared to 3 additional correct NA identifications, whereas in 1996 there are 9 more identifications made by the NA and 6 more by the SA. In 1997, the 95% confidence bound was determined to be ±8 and ±5 events for the SA and NA respectively (see Equation 5.20 and Table 5.5). This result means that the difference between the SA and the NA are statistically significant. For 1996-60, the 95% confidence bound was determined to be ±6 and ±7 events for the SA and NA respectively. The difference between the NA and the SA in 1996-60 is not statistically significant. however, the difference between the SA in 1997 and 1996-60 is statistically significant. One possible explanation for the increased SA identifications in 1997 is that the effect of precipitation on the spectral slope may be longer lasting than the increase in SSL_{20}, so that at the short sampling rate used in 1997, the majority of the observed precipitation spectra have the spectral slope characteristic and not the elevated sound level. A second possible explanation is that the SA is more sensitive to time averaging: the number of identifications made by the SA is reduced in 1996 compared to the identifications made using the NA.

In general, there is no improvement in either the Sensitivity or the Confidence of either algorithm in 1996 compared to 1997, lending support to the theory that the majority of missed identifications are a consequence of drop size distribution and not the sampling mismatch. This theory is investigated by examining the Sensitivity of each algorithm in detail.

143

5.5.3 Sensitivity of the PIAs

There are two known factors which affect the precipitation generated ambient sound signal. The first is the drop size, which affects the probability of bubble entrainment. If there is no bubble then there is no significant sound generated by the drop impact (Medwin et al. 1992). The second is wind speed which increases the probability of bubble production for large drops (Medwin et al. 1992) but decreases the probability of bubble entrainment for small drops (Nystuen 1986). To examine the importance of the current meteorological conditions, the results from both data sets have been combined and sorted into detections based on both wind speed and the type of precipitation as defined by the WMO sub-categories in Table 5.6.

Wind Speed in m·s⁻¹	0-3 371 40*			5-10 1180 123*			10-15 578 241 23*			15-20 241 23*		
Category	WSO2	SA	NA	WSO2	SA	NA	WSO2	SA	NA	WSO2	SA	NA
Int. D 61**	5	0	0	31	3	2	33	0	0	4	1	1
Cont. D 42**	5	0	0	36	0	1	15	0	0		0	0
Int. R 65**	9	2	2	48	11	11	12	1	4	1	1	1
Cont. R 111**	9	3	3	50	30	26	34	10	10	11	7	7
Showers 120**	14	0	0	8	2	2						
Solid P 70**	15	3	0	26	2	0	17	6	2			
Undefined 101**	55	5	1	196	17	11	99	9	4			
Totals 582**	92	13	9	429	69	64	244	30	15	25	11	10
PIA Tot		19	11		94	40		23	19		11	10

Table 5.6: Summary of correct identifications for the 1997 and the 1996-00 data sets. sorted by wind speed and precipitation category. † the number of ambient sound recordings in a given wind speed range. * the number of WMO observations with precipitation. ** the number of observations within the WMO sub-category.

5.5.3.1 By Precipitation Category

To investigate the influence that the type of precipitation has on the ambient sound spectrum, the detections for both deployments have been combined for each algorithm based on WMO sub-category in Table 5.7. In the *Totals* row, the 3.8% difference between the total identifications of the NA and the SA is statistically significant. using 95% confidence bounds (see Equation 5.20).

144

Category	SA Sensitivity	NA Sensitivity	Occurrence
Intermittent Drizzle	$6.3\% \pm 6.25\%$	$6.9\% \pm 6.25\%$	64
Continuous Drizzle	$0.0\% \pm 2.4\%$	$2.3\% \pm 2.4\%$	42
Intermittent Rain	$28.4\% \pm 12.3\%$	$22.4\% \pm 12.3\%$	65
Continuous Rain	$51.3\% \pm 9.9\%$	$51.4\% \pm 9.9\%$	111
Showers	$4.0\% \pm 4.3\%$	$2.0\% \pm 2.2\%$	139
Solid Precipitation	$14.1\% \pm 10.2\%$	$3.3\% \pm 3.3\%$	59
Undefined	$8.1\% \pm 3.3\%$	$5.5\% \pm 2.9\%$	308
Total	$15.7\% \pm 1.4\%$	$12.5\% \pm 1.4\%$	831

Table 5.7: Percentage of total precipitation correctly identified by the SA and the NA (the Sensitivity, Equation 5.11), sorted by WMO sub-category for the 1997 and 1996-60 data sets combined. Included is the total number of precipitation intervals in each sub-category under the *Occurrence* column. The uncertainty in each column was determined using Equation 5.20 and 95% confidence.

In general. neither algorithm is effective at identifying 'Drizzle,' as defined by the WMO sub-categories. Both algorithms identify nearly 7% of the 'Intermittent Drizzle,' corresponding to a 0.10 $mm\,hr^{-1}$ rainfall rate (see Table 5.2). Due to the small sample size in this category, the uncertainty is 6.25%. There is no significant precipitation identified by either algorithm (within 95% confidence) for this WMO sub-category. Neither algorithm identifies significant amounts of 'Continuous Drizzle,' which corresponds to 0.13 $mm\,hr^{-1}$. 'Showers,' which are defined as intermittent shown by the number of minutes of rain but have rainfall rates of 1.47 $mm\,hr^{-1}$, are also unidentified by acoustic means. The 'Undefined' precipitation is inconsistently identified through the ambient sound spectra, with the NA detecting 5% and the SA 8% of the precipitation. In each of these four categories it is not clear whether the low Sensitivity is a result of: i) the intermittent nature of the rainfall; ii) the drop size distribution associated with the rainfall rate.

'Solid' precipitation shows the largest difference between the two algorithms:

the SA detects 10.8% more 'Solid' precipitation than does the NA, but this difference is not significant. If a 60% confidence is assumed, where the uncertainty is approximately half the value listed in Table 5.7, the difference is between the identifications made by the NA and SA is significant. Regardless, neither algorithm identifies a significant portion of this form of precipitation. This category is also intermittent having on average 20 minutes of precipitation per hour.

The two 'Rain' categories show more frequent ambient sound signals corresponding to precipitation. Both algorithms identify approximately 25% of the 'Intermittent Rain.' The success rate of both algorithms is equal within the confidence bounds, and distinct from 0, resulting in a minimum detection of 28.4% and 22.4% for the SA and the NA respectively. Both algorithms detect slightly more than 50% of the 'Continuous Rain' events.

These results indicate that there is a strong relation between the acoustic signal of precipitation and the WMO sub-category.

5.5.3.2 By Wind Speed

To determine if the wind speed affects the precipitation generated ambient sound, signal identifications for both data sets are presented for each algorithm in Table 5.8. These results show that there is only statistically meaningful differences (using 95% confidence intervals) between wind speeds greater than $15 m\,s^{-1}$ and those less than $15\ m\,s^{-1}$ for both the NA and the SA. This result is remarkable in that at high wind speeds (15 to 20 $m\,s^{-1}$) the Sensitivity of both algorithms is at a maximum, correctly identifying more than 40% of the precipitation. This results may be due to the drop size present during the storms which generate such high wind speeds, however, there are only 23 precipitation events in this wind speed range resulting in

146

Wind Speed	SA Sensitivity	NA Sensitivity	Occurrence
0-5 $m\,s^{-1}$	14.1% ± 7.6%	9.8% ± 7.6%	92
5-10 $m\,s^{-1}$	16.3% ± 3.8%	15.1% ± 3.8%	423
10-15 $m\,s^{-1}$	12.3% ± 4.5%	6.1% ± 3.3%	244
15-20 $m\,s^{-1}$	47.8% ± 26.0%	43.5% ± 26.0%	23
Total	15.7% ± 1.4%	12.5% ± 1.4%	782

Table 5.8: Percentage of total precipitation correctly identified by the SA and the NA (the Sensitivity, Equation 5.11), by wind speed for 1997 and 1996-60 combined. Included are the total number of precipitation intervals in each wind speed range (Occurrences). The uncertainty in each column was determined using Equation 5.20 and 95% confidence.

a large uncertainty of approximately 26%.

95% confidence bounds are perhaps too strict. If 60% confidence bounds were used instead the SA identifies more precipitation in the wind speed range 10 to 15 $m\,s^{-1}$ than does the NA. Also, the NA shows a wind speed dependence, identifying more precipitation in the 5 to 10 $m\,s^{-1}$ range than in either the 0 to 5 or 15 to 20 $m\,s^{-1}$ range. The sensitivity of the NA ranges from as low as 6.1% (wind speeds between 10 and 15 $m\,s^{-1}$) and as high as 15.1% (wind speeds of 5 to 10 $m\,s^{-1}$). The sensitivity of the SA ranges from a low of 12.3% (for wind speeds from 10 to 15 $m\,s^{-1}$) and a high of 16.3% (wind speeds between 5 and 10 $m\,s^{-1}$).

5.5.3.3 Effect of Sampling Rate

The ambient sound sampling rate affects the probability of detecting precipitation (see §5.3.1). The importance of the sampling rate is explored by comparing the identifications made from the hourly averaged ambient sound spectra from the 1996-60 data and those from the 1997 data. Tables D.3 and D.4 in Appendix D.1 show a complete break down for each deployment by wind speed and category. The sensitivity data from these two tables are summarized by WMO sub-category in Table 5.9.

Data Set	1996-60			1997		
Category	SA	NA	Occurrence	SA	NA	Occurrence
Intermittent Drizzle	3.9% ± 3.9%	1.9% ± 1.9%	52	16.7% ± 16.7%	8.3% ± 8.3%	12
Continuous Drizzle	0.0%	0.0%	25	0.0%	5.5% ± 5.5%	17
Intermittent Rain	31.5% ± 14.3%	30.3% ± 16.2%	33	33.0% ± 18.4%	15.6% ± 11.4%	32
Continuous Rain	45.0% ± 16.2%	56.0% ± 16.2%	50	37.4% ± 9.4%	42.3% ± 9.5%	61
Showers	3.3% ± 3.3%	3.3% ± 3.3%	60	5.3% ± 3.7%	1.3% ± 1.3%	79
Solid Precipitation	0.0%	0.0%	9	26.9% ± 11.0%	6.0% ± 6.0%	50
Unclassified	9.2% ± 3.2%	7.2% ± 4.4%	131	7.2% ± 4.0%	5.6% ± 4.0%	151

Table 5.9: Summary of algorithm Sensitivity sorted by WMO sub-category for both the 1996-60 and 1997 data sets. The values are the total number of scattering intervals in each WMO sub-category (Occurrences). The uncertainty in each column was determined using Equation 5.20 and 95% confidence.

Within 95% confidence bounds, there is no Sensitivity difference between the 1996-60 and 1997 data. This means that using the present data, the increased sampling rate of the 1996-60 data (sampled 51 times per hour) does no better than the sampling rate of 1997 (sampled 3 times per 72 minutes). However, there is substantial ensemble averaging (17 ensembles) for the 1996-60 data, and no ensemble averaging in 1997. Ensemble averaging has the effect of smoothing out the spectral characteristics of precipitation.

The values of Sensitivity based on wind speed range are more likely to vary with the precipitation type within each wind speed category for each deployment than with wind speed. Realistically, there is no relation between sampling rate and wind speed, while there is a relation between the sampling rate and precipitation category.

5.5.4 PIA Confidence and Wind Speed

The Confidence (Equation 5.10) of a PIA is a measure of the correct identification rate and is shown for overall performance in Table 5.5. With a 95% confidence bound there is no difference in the Confidence of the two algorithms.

The detection method of the two PIAs depends on the spectral structure that changes with wind speed. We might then expect PIA confidence to depend on wind speed.

Table 5.10 shows the Confidence of each algorithm for both data sets combined for four wind speed ranges. The SA makes fewer false identifications in the 10-15 $m\ s^{-1}$ wind speed range when compared to the identifications in the 5-10 $m\ s^{-1}$ range. The NA does not reflect this trend. The 100% identification represents the

Wind Speed	SA	Occurrence	NA	Occurrence
0 - 5 $m\ s^{-1}$	$72.2 \pm 27.7\%$	18	$81.8 \pm 18.2\%$	11
5 - 10 $m\ s^{-1}$	$73.4 \pm 9.6\%$	94	$80.0 \pm 10.5\%$	76
10 - 15 $m\ s^{-1}$	$93.8 \pm 6.3\%$	32	$78.9 \pm 21.1\%$	19
15 - 20 ^{1} $m\ s^{-1}$	100%	11	100%	10
Total	$79.4 \pm 7.1\%$	155	$81.7 \pm 7.8\%$	116

Table 5.10: Percentage of correct identifications of precipitation made by the SA and the NA (the Confidence, Equation 5.10), sorted by wind speed for 1996-60 and 1997 data sets combined. The uncertainty in each column was determined using Equation 5.20 and 95% confidence. ^{1} the 95% confidence bound for 6 selections.

95% confidence bound for 60% ± 40% identifications, given the limited number of identifications made in this wind speed range, which were only 11 and 10 identifications by the SA and the NA respectively. Within 95% confidence there is no difference between the the algorithms at any wind speed range.

5.6 Conclusions

There is significant correlation between two characteristics of ambient sound. These characteristics are the spectral slope of Region III (from 35 to 72 kHz) and the elevated SSL at 20 kHz (SSL_{20}) generated by precipitation. Two distinct algorithms

can be used to identify precipitation using either of these characteristics. In addition to the classical detection algorithm using the SSL_{26}, the slope of Region III provides an alternative means of detecting precipitation. In this §5.5, the present data shows that limitations in detecting precipitation are placed on both algorithms by meteorological conditions.

There is meaningful signal in the ambient sound at frequencies from 35 to 72 kHz. This signal is generated during precipitation, and occurs in conjunction with the precipitation signal used by the NA. In contrast, Urick (1967) stated that the ambient sound at frequencies greater than 50 kHz is dominated by thermal noise. The results presented here support the findings from Chapter 4 which state that the intersection of thermal noise and ambient sound is at frequencies greater than 72 kHz when the wind speed is greater than 3 $m\ s^{-1}$ or precipitation is present.

Using 95% confidence bound, neither algorithm is effective at detecting all forms precipitation. The overall Sensitivity (Equation 5.11) is affected by the distribution of precipitation rates. In general, only the rain WMO categories are detectable via ambient sound. Both algorithms successfully identify $25\% \pm 12.5\%$ of 'Intermittent Rain' events, and $50\% \pm 10\%$ of 'Continuous Rain' events. However, the cause of this limited Sensitivity cannot be determined conclusively from the present data because the intermittent nature of the rainfall cannot be determined from the instantaneous rainfall rate (or drop size). The limited Sensitivity is likely due to a combination of three factors: i) the sampling rate of the ambient sound is too short to detect intermittent precipitation signals; ii) time averaging reduces the precipitation signal by averaging intermittent precipitation signals with wind-only dominated spectra; or iii) the rainfall rate for a given WMO sub-category varies during isolated

precipitation events. Comparison of the 1996 data averaged to 10 minute intervals and 60 minute intervals indicates that time averaging is not the dominant cause of low Sensitivity. Comparison of the hourly averaged data sampled 51 times per hour (1996-60) to the 1997 data set, sampled once every 24 minutes, indicates that the sampling rate is not the dominant cause of the observed low Sensitivity. A more frequently sampled precipitation record and a measurement of the drop size distribution is required for further study of the sampling rate effect. The present data is consistent with an evolving raindrop distribution: the rainfall rate determines the acoustic signal; this rainfall rate will vary for a given condition changing the probability of detection. More frequent WMO recorded observations, or preferably disdrometer and ORG measurements, are necessary to compare to unaveraged short time interval ambient sound data in order to rigorously test the effect of sampling rate and time averaging.

Complementing the description of the high frequency spectral precipitation signal is the fact that the high frequency side of the signal behaves differently than the 20 kHz peak under different meteorological conditions. The SA is more effective at identifying 'Solid Precipitation' than is the NA, although the SA only identifies $14\% \pm 10.2$ of the 'Solid' events compared to the $3\% \pm 3$ identified by the NA. One final difference between the algorithms: the SA makes fewer false identifications, and identifies more precipitation than does the NA in wind speeds of 10 to 15 $m\,s^{-1}$. Overall, the SA identifies 3% more precipitation than does the NA.

There are occurrences when the SA correctly identifies more precipitation than the NA, particularly using the 1997 data (see Figure 5.11). This result might indicate that the precipitation signal at frequencies from 35 to 72 kHz is less robust to time

151

averaging than is the elevated SSL_{20}. In the 1996-60 data set, 17 ensembles are averaged together, whereas in 1997 there is no ensemble averaging. In both cases each ensemble is an average of three individual ambient sound samples.

Chapter 6

Conclusion

There are many sources of ambient sound in the ocean (see Table 2.1). For frequencies from 1 to 72 kHz the dominant source is wind through bubble entrainment caused by breaking waves. Precipitation at the surface also elevates sound levels between 10 and 25 kHz. It has been shown in this thesis that there is a distinct spectral slope for frequencies from 35 to 72 kHz during precipitation. The sound source here is air bubbles entrained by raindrop impacts at the surface (Pumphrey et al. 1989; Medwin et al. 1992). When created, pressure and tension forces drive air bubbles at their breathing mode, generating sound at frequencies related to their radius. Smaller bubbles generate higher frequency sound (see Figure 2.2).

Acoustically active bubbles entrained by both breaking waves and drop impact remain close to the surface. The surface is a near perfect acoustic reflector, and as such, the bubbles generate sound as dipole sources as a consequence of the bubble's image through the surface. The resulting sound field can be modelled by an infinite plane of dipole sources at the surface, although this assumption might not be valid for intermittent rain showers. Due to this geometry, the sound field does not die off according to spherical spreading (Medwin and Beaky 1989), but is only affected by

chemical absorption along the path length. Sound reflected off the ocean bottom retains this characteristic. As a result, significant energy is added to the sound field when the bottom is not sufficiently far such that chemical absorption completely attenuates the sound. To identify characteristics of wind-generated and precipitation-generated ambient sound, measured Sound Source Levels (SSL) must then account for reflections of sound off the bottom of the ocean.

As a result of the different effects of hydrophone depth, and the ocean bottom depth. SSL must be adjusted to deployment independent levels. This adjustment is done using a model developed here (Equation 3.22) which calculates the energy added to the system through reflections and lost from the system by chemical absorption. Several factors are incorporated in this model: the bottom loss reflection coefficient. the chemical absorption (via the hydrophone and ocean bottom depth). the temperature (via the chemical absorption), and the nature of the reflections at the bottom (either specular or non-specular). At the surface, the model assumes an infinite plane of dipoles, non-specular reflection, and no refraction. By integrating over the infinite plane, and modelling multiple reflections, the deployment 'Response' is calculated additionally allowing for the factory determined hydrophone response.

Results of this model show that significant energy is added to the spectrum for frequencies below 10 kHz (see Figure 3.7c). Using a bottom reflection loss coefficient of -8 dB, there is significant energy added to the sound field for frequencies less than 10 kHz even for ocean depths greater than 4000 m. A maximum of 1.5 dB is added for all depths at 1 kHz. The frequency range to which this energy is added increases with decreasing water depth. Further, there is little difference whether the reflections are specular or non-specular, accounting for a difference in Response of

less than 0.2 dB (see Figure 3.7a). The temperature of the water does not change the Response for frequencies less than 4 kHz. For frequencies between 4 and 10 kHz a temperature change of 20 °C alters the Response by half a dB. This difference increases to a maximum of 2 dB by 35 kHz for a temperature change of 20 °C (see Figure 3.7b). The depth of the hydrophone affects the attenuation of the ambient sound signal by increasing the path length to the surface. At mooring depths of 4000 m. there is a loss greater than 18 dB for frequencies greater than 35 kHz. At this depth, however, there is a loss of only 2 dB for frequencies between 1 and 10 kHz, indicating that accurate measurements of the ambient sound generated at the surface can be recorded at such a large depth (see Figure 3.7d). This result assumes no refraction of the sound which is incident near normal to the horizontal.

Uncertainty in the model arises from the uncertainty in the temperature. depth and the measured SSL. These sources of uncertainty are calculated in Chapter 3 and estimates of frequency dependent uncertainty in SSL are shown in Figure 3.11 (in dB). The uncertainty in depth and temperature affect the accuracy of spectral slope estimates. Three spectral regions have been considered and are Regions I (1 to 10 kHz), II (10 to 35 kHz), and III (35 to 72 kHz) with uncertainties of 0.13, 0.12, and 1 dB/decade respectively.

Any subsurface hydrophone records sound generated at the surface in a circle of radius approximately equal to the hydrophone depth due to the dipole nature of the sources. As a result, the mean sound generated by breaking wind waves in that circle can be translated to a wind speed estimate (Knudsen et al. 1948; Wenz 1962: Shaw et al. 1978). The mean sound level is characteristic of a given wind speed. Due to the transient nature of breaking waves, at any instant in time this SSL could

155

be louder or quieter than the characteristic sound proportional to the instantaneous wind speed. However, given sufficient averaging an accurate wind speed estimate can be determined.

If the SSL are not set to reference levels which are deployment independent, a frequency dependent mean error in wind speed estimate results. Even if the calibration is performed correctly to the best of our ability, the wind-speed-from-ambient-sound equations tested here (Equations 4.3, 4.4 and 4.5) result in a mean wind speed error using the SSL from 1 to 10 kHz. The mean error can be removed by adding a wind speed dependent correction term to the wind-speed-from-ambient-sound equations.

Time averaging and spectral averaging both work to reduce the variance in the wind speed estimate. The effects of this averaging are not additive: even when frequency effects have been removed (Equation 4.5) there is no reduction in the variance of the estimate when both time averages and spectral averages are used. In contrast, when only spectral averaging has been performed, variance for this equation is reduced by 0.4 $m\ s^{-1}$.

The equations determined by Vagle et al. (1990) (Equation 4.4) and Evans and Watts (1982) (Equation 4.3) can be used for any frequency from 1 to 10 kHz, by adjusting the SSL to a reference frequency. The accuracy of the wind speed estimates are determined in part by the accuracy of the SSL measurement, so that spectral averaging improves the wind speed estimate from the SSL at 1 kHz (SSL_1) but does not reduce the variance for the SSL for frequencies between 8 and 10 kHz in the 1996 data set.

The accuracy of the mean wind speed estimate when the wind speed dependent

156

error has been removed (Equation 4.19) for frequencies from 1 to 10 kHz are 1.99, 1.27 and 1.63 $m\,s^{-1}$ for the 1996-10, 1996-60 and 1997 data sets respectively. These differences reflect the different deployment characteristics and sampling parameters of each data set. The 1996 data was collected with the hydrophone at 250 m, while the 1997 data was collected with the hydrophone moored at 100 m. In 1996, the ambient sound field was sampled every 70 seconds while in 1997 it was sampled every 24 minutes. Two time intervals were considered in 1996: 10 minute averages (1996-10) and hourly averages (1996-60). The more frequent sampling, larger listening radius, and ensemble averaging of the 1996-10 data set unexpectedly produces greater variance than the data of 1997. It was expected that time averaging and spectral averaging would reduce the variance, and that more frequent ambient sound samples would provide more accurate resolution of the wind field. This result indicates that there may be a time scale between 10 and 60 minutes over which the ambient sound does not respond to changes in the wind speed. In other words, more frequent sound sampling may not provide a more accurate estimate of wind speed, below some threshold sampling rate.

It was observed that the spectral slope depends on both the wind speed and the frequency. The spectral slope for frequencies from 1 to 10 kHz (Region I) was observed to vary by 4 dB/decade over wind speeds from 0 to 20 $m\,s^{-1}$. The mean spectral slope of this region is -18.6 ± 0.4 dB/decade. For frequencies from 10 to 35 kHz (Region II), the spectral slope for winds from 0 to 10 $m\,s^{-1}$ has a mean of -17.3 ± 0.5 and varies by 4 dB/decade. For wind speeds from 10 to 20 $m\,s^{-1}$ the spectral slope varies by 15 dB/decade. The spectral slope for frequencies from 35 to 72 kHz (Region III) has been modelled using a polynomial of order three.

157

For wind speeds from 0 to 9 $m\,s^{-1}$ the spectral slope steepens from greater than 0 dB/decade to approximately -18 dB/decade. For wind speeds from 9 to 13 $m\,s^{-1}$ the spectral slope of this Region remains constant, then increases to -10 dB/decade at wind speeds of 20 $m\,s^{-1}$.

Precipitation generates sound by entraining bubbles through craters resulting from drop impacts at the ocean surface. Not all drop sizes create craters capable of entraining bubbles. The wind speed also affects the probability of bubble entrainment. These two factors combine to create a complicated relationship, where rain creates a different acoustic signature than does drizzle. As well, some significant forms of precipitation do not generate any significant ambient sound. Two algorithms capable of identifying precipitation via the ambient sound were presented in Chapter 5. They are the Nystuen Algorithm (NA), which identifies the increase in SSL at 20 kHz (SSL_{20}) relative to SSL_4, and the Slope Algorithm (SA) developed here, which identifies the distinct spectral slope of Region III during precipitation.

Precipitation events classified as 'Rain' by the World Meteorological Organization (WMO) can be identified via the ambient sound. The NA is as effective as the SA. Neither algorithm detects more than 50% ± 10% of the 'Continuous Rain' events, and 25% ± 12.5% of the 'Intermittent Rain' events. Using the minutes of precipitation observed by an Optical Drop Rain Gauge (ORG) available from the 1997 data for WMO sub-categories, a larger percentage of precipitation should be identified for the more frequently sampled data from 1996 (see Equation 5.2). This result indicates that rain detection is drop size dependent. The data show some variation between the two algorithms in detection of 'Solid Precipitation.' The SA detects 14% ± 5% and the NA detects 3% ± 3% of this WMO sub-category (within 95%

confidence bounds).

The data from 1996 averaged into 10 minute intervals do not provide more significant identification of precipitation via either algorithm, indicating that the sampling rate is not a factor in the limited detection of precipitation. However, the averaging of the WMO observations skew these results. Further, when comparing the data from 1996 sampled every minute but averaged into hourly intervals to the unaveraged 72 minute ensembles from 1997, a larger percentage of identifications of precipitation via the ambient sound are not observed. Time averaging of frequent observations provides no enhancement over less frequently sampled observations.

Bibliography

Banner, M. and Cato, D. H. (1988). Physical mechanisms of noise generation by breaking waves. *Sea Surface Sound: Natural mechanisms of surface generated noise in the ocean*, 1:429–436.

Bom, N. (1969). Effect of rain on underwater noise level. *J. Acoust. Soc. of Am.*, 45:150–156.

Brekhovskikh, L. M. and Lysanov, Y. P. (1991). *Fundamentals of Ocean Acoustics*. Springer Verlagg.

Burdic. W. S. (1984). *Underwater Acoustic System Analysis*. Prentice-Hall.

Cato. D. H., Tavener, S., and Jones, I. (1995). Ambient noise dependence on local and regional wind speeds. *Sea Surface Sound '94*, 1:95–111.

Clay. C. S. and Medwin, H. (1977). *Acoustical Oceanography*. Wiley-Interscience.

Crawford. G. B. and Farmer, D. M. (1987). On the spatial distribution of ocean bubbles. *J. Geophys. Res.*, 92:8231–8243.

Dahl. P. H. and Jessup, A. T. (1995). On bubble clouds produced by breaking waves. *J. Geophys. Res.*, 100:5007–5020.

Evans, D. L. and Watts, D. R. (1982). Wind speed and stress at the sea surface from ambient noise measurements. *Proceedings International Symposium on Acoustic Remote Sensing Atmos. and Oceans.*, pages 69–78.

Evans, D. L., Watts, D. R., Halpern, D., and Bourassa. S. (1984). Oceanic winds measured from the sea floor. *J. Geophys. Res.*, 89:3457–3461.

Everitt. B. S. (1992). *The Analysis of Contigency Tables*. Chapman and Hall.

Farmer. D. and Lemon, D. (1984). The influence of bubbles on ambient noise in the ocean at high wind speeds. *J. Phys. Oceanogr.*, 14:1762–1778.

Farmer. D. M., Vagle, S., and Booth. A. D. (1998). A free flooding acoustical resonator for measurement of bubble size distribution. *J. Atmos. and Oceanic Tec.*, 15:1132–1146.

Franz. X. (1959). Splashes as sources of sounds in liquids. *J. Acoust. Soc. of Am.*, 31:1080–1096.

Gammelsroed, Osterhus, S., and Godoy, O. (1992). Decadal variations of ocean climate in the norwegian sea observed at ocean station "mike". *ICES Marine Symposium*, 195:68–75.

Heindsman, T., Smith, R. H., and Arneson, A. D. (1955). Effect of rain upon underwater noise levels. *J. Acoust. Soc. of Am.*, 27:378–379.

Johnson, B. D. and Cooke, R. C. (1979). Bubble populations and spectra in coastal waters. *J. Geophys. Res.*, 84:3761–3766.

Kerman, B. R. (1984). Underwater sound generation by breaking wind waves. *J. Acoust. Soc. of Am.*, 75:149–165.

Knudsen, V., Alford, R., and Emling, J. (1948). Underwater ambient noise. *J. Marine Research*, 7:410–429.

Kolaini, A. R. (1998). Sound radiation by various types of laboratory breaking waves in fresh and salt water. *J. Acoust. Soc. of Am.*, 103:300–308.

Kolaini, A. R., Crum, L., and Roy, R. (1994). Bubble production by capillary-gravity waves. *J. Acoust. Soc. of Am.*, 95:1913–1921.

Kolovayev, P. A. (1976). Investigation of the concentration and statistical size distribution of wind-produced bubbles in the near surface ocean layer. *Oceanology*, 15:659–661.

Leighton, T. G. (1994). *The Acoustic Bubble*. Academic Press.

Lemon, D. D., Farmer, D. M., and Watts, D. R. (1984). Acoustic measurements of wind speed and precipitation over a continental shelf. *J. Geophys. Res.*, 89:3462–3472.

Lokken, J. and Bom, N. (1972). Changes in raindrop size inferred from underwater noise. *J. Appl. Meteor.*, 11:553–554.

Medwin, H. (1977). Acoustical determination of bubble size spectra. *J. Acoust. Soc. of Am.*, 62:1041–1044.

Medwin, H. and Beaky, M. M. (1989). Bubble sources of the knudsen sea noise spectra. *J. Acoust. Soc. of Am.*, 86:1124–1130.

Medwin, H., Nystuen, J., Jacobus, P. W., Ostwald, L. H., and Snyder, D. E. (1992). The anatomy of underwater rain noise. *J. Acoust. Soc. of Am.*, 92:1613–1623.

Mellen. R. H. (1952). The thermal-noise limit in the detection of undewater acoustic signals. *J. Acoust. Soc. of Am.*, 24:478–480.

Melville, W. K. and Rapp, R. J. (1989). Experiments on breaking waves. *Sea Surface Sound: Natural mechanisms of surface generated noise in the ocean.* 1:39–49.

Melville, W. K., Terrill, E., and Ding, L. (1995). Field measurements of air entrainment by breaking waves. *Third International Symposium on Air-Water Gas Transfer*, 95.

Nystuen. J. A. (1986). Rainfall measurements using underwater ambient noise. *J. Acoust. Soc. of Am.*, 79:972–982.

Nystuen. J. A. (1987). Influence of wind on the underwater sound generated by light wind. *J. Acoust. Soc. of Am.*, 82:270–274.

Nystuen. J. A. (1996). Acoustical rainfall analysis: Rainfall drop size distribution using the underwater sound field. *J. Atmos. and Oceanic Tec.*, 13:74–84.

Nystuen. J. A. (1998). Rainfall at the air-sea interface. *Conference Proceedings, American Meteorological Society, 9th Conference on Interatction of the Sea and Atmosphere,* January:146–148.

Nystuen. J. A. and Selsor, H. D. (1997). Weather classification using passive acoustics drifters. *J. Atmos. and Oceanic Tec.*, 14:656–666.

Oğuz, H. N. and Prosperetti, A. (1992). Drop impact and the underwater rain noise. *Natural Physical Sources of Underwater Sound: Sea Surface Sound (2)*, 2:669–682.

Papanicolaou, P. and Raichlen, F. (1988). *Sea Surface Sound: Natural mechanisms of surface generated noise in the ocean*, 86:97–110.

Pickard. G. L. and Emery, W. J. (1996). *Descriptive Physical Oceanography, 5th Ed.* Butterworth Heinemann.

Potter. J. R. (1993). Acoustic imaging using ambient noise:some theory and simulation results. *J. Acoust. Soc. of Am.*, 95:21–33.

Pumphrey. H., Crum, L., and Bjørnø, L. (1989). Underwater sound produced by individual drop impacts and rain fall. *J. Acoust. Soc. of Am.*, 92:1613–1623.

Scrimger, J., Evans, D., McBean, G., and Farmer, D. (1987). Underwater noise due to rain. hail, and snow. *J. Acoust. Soc. of Am.*, 92:1613–1623.

Shaw, P., Watts. D. R., and Rossby, H. (1978). On the estimation of oceanic wind speed and stress from ambient noise measurements. *Deep Sea Res.*, 25:1225–1233.

Updegraff and Anderson (1991). *J. Acoust. Soc. of Am.*, 89:2264–2279.

Urick, R. J. (1967). *Principles of Underwater Sound for Engineers*. McGraw-Hill.

Vagle, S., Large, W., and Farmer, D. (1990). An evaluation of the wotan technique of inferring oceanic winds from underwater ambient sound. *J. Atmos. and Oceanic Tec.*, 7:576–595.

Wenz, G. (1962). Acoustic ambient noise in the ocean:spectra and sources. *J. Acoust. Soc. of Am.*, 34:1936–1956.

Wilson, J. H. (1980). Low frequency wind-generated noise produced by the impact of spray with the ocean's surface. *J. Acoust. Soc. of Am.*, 68:952–956.

Wu, J. (1981). Bubble populations and specctra in near-surface ocean: summary and review of field measurements. *J. Geophys. Res.*, 86:457–463.

Zedel, L., Gordon, L., and Crawford, G. (1996). Wind direction from and upward looking adcp. *J. Geophys. Res.*, 101:12163–12176.

Zedel, L., Gordon, L., and Osterhus, S. (1998). Ocean ambient sound instrumentation system: Acoustic estimation of wind speed and direction from a sub-surface package. *J. Atmos. and Oceanic Tec.*

Appendix A

Absorption Coefficient

In Chapter 2. the equation describing the propagation of sound through water were developed. In the process, the absorption coefficient due to three chemical components of salt water were identified. Equations describing the absorption coefficients from these three components are included in this appendix.

The finite time response of water to a changing pressure field. causes dispersion of sound waves in water. The phenomenon is modelled by adding a time dependent term to Hooke's law model of sound travelling in water. This time response is modelled by an absorption coefficient.

If the relaxation time is longer than the period of the pressure variations. then some of the energy at this frequency is lost as heat. It is this mechanical relaxation process which is responsible for increasing absorption with increasing frequency. In salt water the mechanical relaxation is governed by three processes, each of which are characterized by individual absorption coefficients. Clay and Medwin (1977) give a complete description of all the components of the absorption coefficient in salt water. The three processes are: freshwater absorption (Equation A.1); absorption by magnesium sulphate ($MgSO_4$) (Equation A.3); and absorption by boric acid

166

(Equation A.5).

$$\alpha_f = 1.71 \cdot 10^8 \frac{\frac{1}{3} \frac{1.2 \cdot 10^{-3} + 3.3 \cdot 10^{-3}}{1000(1.46 \cdot 10^3)^3}}{f^2} f^2 \tag{A.1}$$

$$f_{rm} = 21.9 \cdot 10^{\frac{6 - 1520}{(T + 273)}} \, 1000 \tag{A.2}$$

$$\alpha_m = 35.0 \frac{2.03 \cdot 10^{-5}}{} \frac{f_{rm} f^2}{f^2 + f_{rm}^2} \left(1 - 1.23 \cdot 10^{-3}\right) \tag{A.3}$$

$$f_{rb} = 0.9 \cdot 1.5^{\frac{T}{14}} \, 1000 \tag{A.4}$$

$$\alpha_b = \frac{1.2 \cdot 10^{-4}}{1000} \frac{f^2 f_{rb}}{(f_{rb}^2 + f^2)} \tag{A.5}$$

where α_f, α_m and α_b are the components of the absorption coefficients and f_{rm}, f_{rb} are the resonant frequencies of magnesium sulphate and boric acid relaxation process in kHz.

The temperature of the water has a strong influence on the fresh water component of the relaxation process. For the frequencies studied here, the dominant components of absorption are the magnesium sulfate and boric acid components (see Figures 3.3.1 a and b in Clay and Medwin (1977, pp. 100-101), or a reproduction based on the equations above in Figure A.1 assuming 10°C).
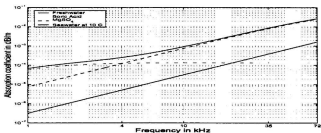
Figure A.1: The relative importance of the different absorption factors in determining the overall absorption coefficient (remake of figure from Clay and Medwin (1977), with the axes limited to the frequency range relevant to this study).

Appendix B

Analysis Using Unaveraged Spectra from 1996

In Chapters 4 and 5, the unaveraged ambient sound levels from the 1996 deployment are not used in the data analysis. They are not used because there are no wind speed or precipitation observations to compared to. However, in Chapter 4, it was determined that the spectral slope of the ambient sound spectrum changes with changes in the ambient sound levels. The time scale over which these properties change is examined using the ambient sound ensembles recorded every 3.5 minutes during 1996.

Ambient sound levels cannot be absolutely correlated to wind speeds: the correlation is a result of time and spatial averaging of breaking wave caused by the wind. However, two physical properties, the spectral slope of Region II and the spectral slope of Region III, are directly correlated to the instaneous sound levels below 10 kHz. The response time of these properties to changes in the sound level are measured for time intervals as short as 3.5 minutes using the unaveraged ambient sound data from 1996.

These recorded ensembles are averages of three measurements recorded at

evenly spaced time intervals over the 3.5 minute total ensemble length. As such, the ambient sound spectra are susceptible to changes in the ambient sound field at time intervals of 70 seconds. Vagle et al. (1990) stated that to get accurate wind estimates, the time intervals must be averaged over three hours. Chapter 4 demonstrates that accurate wind speed estimates can be obtained for 10 minute intervals when 3 ensembles (for a total of 9 ambient sound measurements) are averaged over the entire 10 minute period and the spatial average occuring for the ambient sound measurements over a circle of radius of 250 m. In addition, accurate wind speed estimates can be made from sampling as infrequently as 3 times over a 72 minute period, for spatial averages over a circle of radius of 100 m.

From the reduction in the standard deviation of the error in the wind speed estimate ($\sigma(U_e)$) that spectral averaging has on the wind estimate it was determined that there was the least spectral variation between 2 and 4 kHz (Figure 4.9). The spectral slopes will be compared to the mean SSL using frequencies from 2 to 4 kHz ($SSL_{\overline{2-4}}$) because of this minima, and to ensure that the SSL is not affected by mechanism behind the changing slope of Region II.

Figure B.1 shows the auto-correlation of the $SSL_{\overline{2-4}}$ (blue solid line), and the spectral slopes of Region I (red dashed line), Region II (green dash-dot line), and Region III (cyan dashed line). This figure shows that the $SSL_{\overline{2-4}}$ has autocorrelation coefficients greater than 0.5 for time lags of 10 hours or less Both Region II and Region III have an auto-correlation coefficient $R = 0.6$ at time lags of 5 hours. The spectral slope of Region I is has an autocorrelation of less then $R = 0.5$ for time lag greater than 3.5 minutes. The result for the spectral slope of Region I is a consequence of noise: the spectral slope in this region does not vary with wind speed

170

Figure B.1: Auto-Correlation of the $SSL\overline{2-4}$ (blue solid line), spectral slope of Region I (red dashed line), Region II (green dash-dot line), and Region III (cyan dashed line) as a function of the lag in hours.

so time series is the sum of a constant and a white noise time series. Consequently, the auto correlation is a measure of the correlation of the noise.

Figure B.2 shows the cross-correlation of the $SSL\overline{2-4}$ to the spectral slopes of Region I (red dashed line), Region II (green dash-dot line), and Region III (cyan dashed line). This figure reflects the stationary nature of the spectral slope of Region I (red dashed line). There is no correlation between the spectral slope of Region I and the SSL. In contrast, this figure shows the negative correlation of the slope of Region II and Region III to the $SSL\overline{2-4}$. At zero time lag both regions have a cross-correlation coefficient with the SSL of $R = 0.8$. At a lag of 5 hours the cross-correlation coefficient for both regions is $R = 0.6$.

While the correlation plots show symmetry which indicates that the spectral slopes may lead the SSL, it is presumed that the SSL corresponds to the generation of bubbles, and the variation in spectral slope is an effect of the resident bubble cloud. It is therefore nonsensical to consider the possibility that the spectral slope leads the SSL.
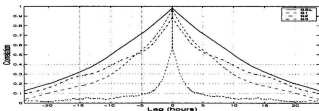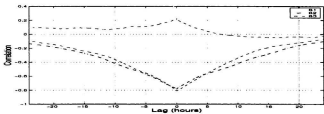
Figure B.2: Cross-Correlation of the spectral slope of Region I (red dashed line), Region II (green dash-dot line), and Region III (cyan dashed line) as a function of the lag in hours.

Appendix C

χ^2 Hypothesis Testing for Contingency Tables

In Chapter 5, the World Meteorological Organization (WMO) observations and observations from the Optical Rain Gauge (ORG) are compared. A standard statistical test is used to determine if the two sets of observations are dependent. This method, χ^2 hypothesis testing, is outlined here.

Given two binary data sets, each with outcomes of Heads (H) and Tails (T), it can be determined whether the two sets are independent by using a χ^2 analysis. To do so, the data can be presented in a contingency table, which compares how often the outcomes of the two sets match (see Table C.1). In Table C.1, a represents the number of times both data sets indicate result H simultaneously, b represents how often data set 2 indicates result H when data set 1 indicated result T. Similarly, c is the number of trials where data set 1 indicated result R while data set 2 indicated NR. Finally, d is the number of times both data sets 1 and 2 indicated result NR simultaneously.

The null hypothesis that two sets are independent is proposed. In other words, the outcome of the first set is in no way affected by the state of the other set. A

| | Data Set 1 | |
	H	T
Data Set 2	H	a	b
	T	c	d

Table C.1: Sample 2 by 2 Contingency Table

χ^2 test is used to reject or accept this hypothesis. This test uses the sum of the difference between the expected values and the actual values of the entries in the contingency table. For this table, the ratio of $\frac{a}{N}$ to $\frac{b}{N}$ should be the same if the two sets were independent, where N is the total number of trials. Everitt (1992) gives the χ^2 for such a table as

$$\chi^2 = \frac{N * (a * d - c * b)^2}{(a + b) * (c + d) * (a + c) * (b + d)} \tag{C.1}$$

Using a look up table, the χ^2 value for 1 degree of freedom, and a 95% confidence interval is 3.84. If the χ^2 value is greater 3.84 we reject our null hypothesis and the sets are not independent. Conversely, if the χ^2 is less than 3.84 the hypothesis is supported, and the data sets are independent.

Appendix D

Additional Rain Detection Information

In Chapter 5, the meteorological observations from the World Meteorological Organization (WMO) standard are subdivided for simplicity. The entries from the WMO standard are presented here for each sub-category. In addition, histograms of the rainfall rate and minutes of rain per hour for each sub-category are presented. Finally, the tabular data for precipitation identification for the algorithms presented in Chapter 5 sorted by wind speed and WMO sub-category are given.

D.1   New WMO Categories: Definition, and Comparison to ORG data

A standard method of recording meteorological activity is given by the International Meteorological Code for Ships according to the World Meteorological Organization (WMO). The data used from this Code for Ships was *Present Weather* Code. The 100 categories of this code have been divided in to eight sub-categories to make comparison to the precipitation identifications from ambient sound. These sub-categories are: no precipitation (0); Intermittent Drizzle (1); Continuous Drizzle (2);

175

Intermittent Rain (3); Continuous Rain (4); Showers (5); Solid Precipitation (6); Unclassified (9). The corresponding entries in the WMO chart for the 'No Precipitation' category are given in Table D.1. The other entries are listed in Table D.2. The entries categorized as some form of precipitation are listed in Table D.2.

WMO	Condition	Category
00-03	Change of Sky During past hour	No Rain (0)
04-09	Haze, Dust, Sand or Smoke	No Rain (0)
10-12	Mist and Shallow Fog	No Rain (0)
13-14	Phenomenon within Sight,but not at ship	No Rain (0)
17-19	Thunder, Squalls, Funnel Clouds	No Rain (0)
28	Fog in past hour	No Rain (0)
30-39	Dust storm, Sand storm or Snowstorm	No Rain (0)
40-49	Fog at time of Observation	No Rain (0)
98	Thunderstorm with dust or sand storm	No Rain (0)

Table D.1: The ww entries from the WMO chart for No Precipitation

WMO	Condition	Classification
15	Precipitation beyond 3 m miles (reaching surface)	Unclassified(9)
16	Precipitation within 3 m miles (reaching surface)	Unclassified(9)
20	Drizzle in past hour	Unclassified(9)
21	Rain (not Freezing)	Unclassified(9)
22	Snow	Solid(6)
23	Rain and snow mixed	Solid(6)
24	Freezing Drizzle or freezing rain	Solid(6)
25	Shower(s) of rain	Showers(5)
26	Showers of snow or rain and snow	Solid(6)
27	Showers of hail, or rain and hail	Solid(6)
29	Thunderstorm, with or without precipitation	Unclassified(9)
50	Intermittent Slight Drizzle	Intermediate Drizzle (1)
51	Continuous Slight Drizzle	Continuous Drizzle(2)
52	Moderate Intermittent Slight Drizzle	Intermediate Drizzle (1)
53	Moderate Continuous Drizzle	Continuous Drizzle(2)
54	Heavy Intermittent Drizzle	Intermediate Drizzle (1)
55	Heavy Continuous Drizzle	Continuous Drizzle(2)
56	Slight Freezing drizzle	Solid(6)
57	Moderate or Heavy Freezing drizzle	Solid(6)
58	Slight Rain and Drizzle Mixed	Unclassified(9)
59	Moderate or Heavy Rain and Drizzle Mixed	Unclassified(9)
60	Intermittent Slight Rain	Intermediate Rain(3)
61	Continuous Slight Rain	Continuous Rain(4)
62	Intermittent Moderate Rain	Intermediate Rain(3)
63	Continuous Moderate Rain	Continuous Rain(4)
64	Intermittent Heavy Rain	Intermediate Rain(3)
65	Continuous Heavy Rain	Continuous Rain(4)
66	Slight Freezing Rain	Solid(6)
67	Moderate of Heavy Freezing Rain	Solid(6)
68	Slight Rain or Drizzle with snow	Solid(6)
69	Moderate or Heavy Rain or Drizzle with snow	Solid(6)
70-79	Solid Precipitation no falling as Showers	Solid(6)
80-84	Slight Rain Shower	Showers(5)
85-90	Solid Precipitation in Showers	Solid(6)
91	Slight Rain (w/ Thunderstorms)	Unclassified(9)
92	Moderate or Heavy Rain(w/ Thunderstorms)	Unclassified(9)
93-97	Thunderstorms and Solid	Solid(6)
99	Heavy Thunderstorms with Hail	Solid(6)

Table D.2: The *ww* entries from the WMO chart and their corresponding Category

D.2 ORG Comparison to each WMO sub-Category

Histograms of the **rain fall rates** in $mm\,hr^{-1}$ and frequency of rain fall over the hour for each category can be made for the 1997 deployment using the ORG data. These histograms are shown for categories 1 (Intermittent Drizzle), 2 (Continuous Drizzle), 5 (Showers), 6 (Solid Precipitation), and 9 (Unclassified) in Figures D.1a to e (the rate) and Figure D.2a to e (the frequency). The histograms for sub-category 3 (Intermittent Rain) and 4 (Continuous Rain) are shown in Chapter 5.

The rainfall rate determines the acoustic signal from the precipitation via the raindrop size distribution. The minutes of rain per hour corresponding to the WMO sub-categories determines the probability of detecting precipitation based on how many times each hour is sampled.

Figure D.1: Histogram of rain fall rates, as determined from by ORG, for WMO sub-category a)'Intermittent Drizzle' (1), b)'Continuous Drizzle' (2), c)'Showers' (5), d)'Solid Precipitation' (6), e)'Unclassified Precipitation' (6).
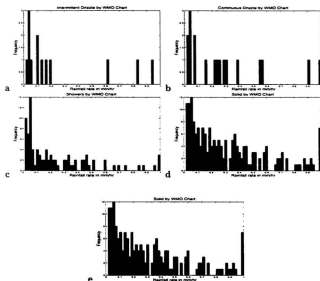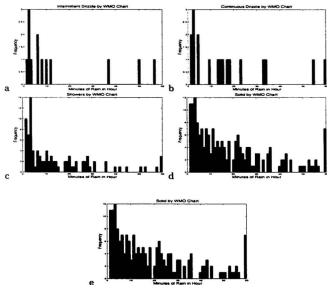
Figure D.2: Histogram of minutes of rain, as determined from by ORG, for WMO sub-category a)'Intermittent Drizzle' (1), b)'Continuous Drizzle' (2), c)'Showers' (3), d)'Solid Precipitation' (6), e)'Unclassified Precipitation' (6).

180

D.3 PIA Identifications for each Deployment Case

The number of correct identifications of precipitation for both algorithms for each deployment have been tabulated by wind speed and precipitation category in tables D.3 and D.4. The two numbers in brackets by the wind speed range are the total number of data points in that wind speed range, followed by the number of intervals which had precipitation in that wind speed range. The number in brackets next to the category is the total number of data points within that category of precipitation. By definition this means these points are precipitation only points. The 'Totals' row is the total of each column in the table, and the 'PIA Totals' are the total number of selections made by either algorithm.

Wind speed	0-5 m/s 225[†]			5-10 m/s 644[†] 258[*]			10-15 m/s 247[†] 168[*]			15-20 m/s 3[†] 4[*]		
Category	WMO	SA	NA	WMO	SA	NA	WMO	SA	NA	WMO	SA	NA
1.12**	0	0	0	10	2	1	2	0	0	0	0	0
2.17**	1	0	0	7	0	0	8	0	0	0	0	0
3.32**	0	1	1	23	0	4	2	0	0	0	0	0
4.61**	6	3	1	38	16	14	26	15	9	1	1	1
5.79**	10	1	0	41	1	5	16	2	0	0	0	0
6.98**	11	3	1	51	5	3	16	6	2	2	2	1
Totals 1**	0	0	0	2	0	0	2	0	0	0	0	0
Totals 491**	56	13	6	99	26	30	29	15	3	3	2	2
PSA Tot		13	6		99	26		29	15		3	2

Table D.3: Summary of correct identifications for the 1997 data set, sorted by wind speed and precipitation category. [†] the number of ambient sound recordings in a given wind speed range. [*] the number of WMO observations with precipitation. ** the number of observations within the WMO sub-category.

Wind speed	0-5 m/s 128[†] 36[*]			5-10 m/s 360[†] 185[*]			10-15 m/s 293[†] 128[*]			15-20 m/s 20[†] 25[*]		
Category	WMO	SA	NA	WMO	SA	NA	WMO	SA	NA	WMO	SA	NA
1.32**	5	0	0	15	1	1	31	0	0	0	0	1
2.25**	4	0	0	12	0	0	6	0	0	0	0	0
3.30**	0	0	0	17	7	18	10	2	0	0	0	0
4.50**	2	0	0	20	2	2	26	1	2	10	3	6
5.62**	4	0	0	4	0	0	1	0	0	0	0	0
6.98**	0	0	0	7	12	9	57	1	1	0	0	0
Totals 360**	2	3	2	185	26	45	129	4	3	20	4	6
PSA Total		7	2		44	34		4	5		4	6

Table D.4: Summary of correct identifications for the 1996-60 data set, sorted by wind speed and precipitation category. [†] the number of ambient sound recordings in a given wind speed range. [*] the number of WMO observations with precipitation. ** the number of observations within the WMO sub-category.

Appendix E

PIA identifications compared to the ORG

In Chapter 5, it was determined that the observations made using an Optical Rain Gauge were statistically dependent on observations made following to the World Meteorological Organization (WMO) protocol. For consistency of results, the WMO observations were used in comparison to observations made using the ambient sound. However, the ORG sampled the precipitation every minute and as such might present a better standard to compare the acoustic identifications of precipitation in 1997. Results using the ORG as the reference are presented here.

There is a sampling mismatch between the ambient sound recordings in 1997 and the WMO log entries from OWS Mike. The ORG data provides a convenient means of creating a record which matches the sampling rate of the hydrophone: by choosing the ORG entries which correspond to the three minutes at which the hydrophone sampled. However, using the ORG as the control for precipitation in the 1997 data set does not yield statistically different results than those obtained using the WMO chart entries. The total number of precipitation events identified by the ORG for the period when the hydrophone was recording was 339. This

number can be compared to the indications of precipitation from the WMO entries of 451. The ratio of precipitation events flagged by the ORG to those flagged by the crew member recording the WMO log entry is 75%, which is approximately the ratio determined earlier for the recent deployment of the ORG and OWS Mike. The WMO log entries and ORG data agreed during 261 intervals. Of the 339 ORG flagged precipitation events, the SA correctly identified 27 'Drizzle' events, 29 'Rain' events, and 7 'Apex' events, compared to 31, 27, and 5 intervals when using the WMO record only. The WMO observations and ORG data agreed during 24, 26, 5 intervals. The NA correctly identified 27 'Drizzle' intervals, and 12 'Rain' intervals when the ORG data is used as the reference versus the 30 and 15 intervals identified when the WMO observations are used as the reference. The WMO observations and ORG data agreed during 24, and 12 of the intervals. These results are summarized in Table E.1, and indicate that the while the Sensitivity of the PIAs are highest when precipitation is limited to when both the ORG data and the WMO observations simultaneously indicate precipitation, the Confidence is at its lowest for both algorithms.

Control	Intervals	SA (86)	NA(55)
ORG	293	63	41
WMO	402	73	44
Exculsive Combination	222	59	30
Inclusive Combination	544	77	45

Table E.1: The correct identifications of precipitation from either algorithm, when the ORG data or WMO observations are used as a reference. The numbers in brackets in the column headings are the total identifications made by the algorithms (correct and incorrect).

The results given in Table E.1 show that there is not better correlation with the precipitation record given by the ORG data. The *Exclusive Combination* category

are identifications made by the algorithms which correspond to both the WMO and the ORG observations. Using identifications in this cateogory, the Sensitivity of the SA improves to 27% (50/222)from 18.2% while the NA improves to 13.4% (30/222) from 10.9%. The increase in Sensitivity is offset by a decrease in Confidence. The Confidence of the SA drops to 68% from 76% while the Confidence of the NA drops to 54% from 86%. The *Inclusive Combination* category are identifications made by the algorithms which correspond to either the WMO or ORG observations. For identifications in this category, the Sensitivity of the SA of both the NA and the SA drop compared to using either the ORG or WMO observations. The Confidence of the SA improves to 89% from 76% while the Confidence of the NA drops to 82% from 86%. The results given in Table E.1 show that there is not better correlation with the precipitation record given by the ORG data.

Appendix F

Spatial Scale of Precipitation

Throughout this entire thesis, observations of ambient sound recorded by the OASIS device at one location are compared to data not necessarily recorded at the exact location of the mooring. To justify these comparisons, the length scale overwhich these meteorological phenomenon occur is necessary.

In an ocean context, micrometeorology is not well studied at spatial scales less than a kilometre. As such, it is hard to specify on what length scales precipitation occurs. A few simple calculations are used to specify this spatial scale. The ORG data provides a time series of rainfall rate recorded every minute. By calculating the autocorrelation as a function of the lag in minutes, the time scale for which meteorological conditions remain constant is estimated. If the ORG rainfall rate time series is converted to a binary series using the threshold rainfall rate for the instrument ($0.1\ mm\,hr^{-1}$), a more representative approximation of this property is realized. The correlation plot is shown in Figure F.1. This figure shows that there is significant correlation at a lag of 10 minutes.

Consider a precipitation event lasting one minute. Assuing that this disturbance propagates at speeds between 5 and 10 $m\,s^{-1}$, which are typical values, the
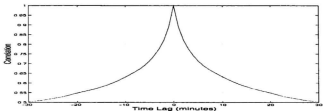
Figure F.1: Auto-Correlation of the ORG rainfall rate as a function the lag in minutes. The ORG rainfall rate was converted to a binary time series using the threshold for precipitation detection of 0.1 $mm\,hr^{-1}$.

disturbance will travel between 300 and 600 m. From the correlation-lag plot it is reasonable to assume that precipitation events, albeit intermittent ones, will travel nearly 5 km (10 minutes · 450 m). From this simple calculation, it is realistic to assume that precipitation occurs over spatial scales on the order of kilometres for this data set.